Title

Synthesis, Characterization, and Reactivity Studies of Iron Complexes Supported by the Redox-Active [ONO] Ligand

Author

Wong, Janice Lin

Publication Date

2014

UNIVERSITY OF CALIFORNIA,
IRVINE

Synthesis, Characterization, and Reactivity Studies of Iron Complexes Supported by the Redox-Active [ONO] Ligand

DISSERTATION

submitted in partial satisfaction of the requirements
for the degree of

DOCTOR OF PHILOSOPHY

in Chemistry

by

Janice Lin Wong

Dissertation Committee:
Professor Alan F. Heyduk, Chair
Professor William J. Evans
Professor Andrew S. Borovik

2014

TABLE OF CONTENTS

Page

LIST OF FIGURES iii

LIST OF TABLES vi

LIST OF SCHEMES vii

LIST OF CHARTS ix

ACKNOWLEDGEMENTS x

CURRICULUM VITAE xi

ABSTRACT OF THE DISSERTATION xiv

CHAPTER 1: Introduction 1

CHAPTER 2: Synthesis and Characterization of Iron Complexes Coordinated to the Redox-Active [ONO] Ligand 17

CHAPTER 3: Reactivity of Iron Complexes Coordinated to the Redox-active [ONO] Ligand 52

CHAPTER 4: Synthesis and Characterization of Homo- and Heterobimetallic Complexes of the Formula 77

CHAPTER 5: Synthesis and Characterization of Homoleptic Chromium(III) Complexes Coordinated to Redox-Active ~-Diimine Ligands 102

APPENDIX: Synthesis of *N*,*N*'-bis-(3-adamantylamino-propyl)-4,5-dimethoxy-benzene-1,2-diamine ($[^{Ad}N_2N_2]H_2$) 121

LIST OF FIGURES

Page

Figure 1.1 (*a*) Structural motifs for tridentate, pincer-type redox-active ligands. (*b*) Three accessible oxidation states of the [ONO] ligand. 8

Figure 1.2 (*a*) Fe[SQ]$_3$ complexes. (*b*) Fe[ONO]$_2$ complex. 12

Figure 2.1 ORTEP diagram of the crystal structure of **1**. Thermal ellipsoids are drawn at 50% probability. Hydrogens have been removed for clarity. 21

Figure 2.2 ORTEP diagram of the crystal structure of **2**. Thermal ellipsoids are drawn at 50% probability. With the exception of H(1), all hydrogens have been removed for simplicity. 23

Figure 2.3 Mössbauer spectrum of [ONHO]Fe(BDI-mes) (**2**) collected at 80 K. 24

Figure 2.4 Crystal structure of **3a**. The hydrogens and *tert*-butyl groups are removed for simplicity. Thermal ellipsoids drawn at 50% probability. 27

Figure 2.5 Mössbauer spectrum of [ONO^{q}]FeCl$_2$ (**3a**) collected at 80 K. The iron(III) species major component (94%) is shown in blue while the iron(II) species minor component (6%) is shown in green. The overall data fit is shown in red. 29

Figure 2.6 X-band EPR spectra of [ONO^{q}]FeCl$_2$ (**3a**; *left*) and [ONO^{q}]FeBr$_2$ (**3b**; *right*). Experimental conditions: $B_1 \perp B_0$; solvent, toluene; temperature, 77 K. 29

Figure 2.7 Crystal structure of **4**. The hydrogens and silicon-bound methyl groups are removed for simplicity. Thermal ellipsoids are drawn at 50% probability. 31

Figure 2.8 X-band EPR spectrum of [ONO^{q}]Fe[N(SiMe$_3$)$_2$]$_2$ (**4**). Experimental conditions: $B_1 \perp B_0$; solvent, toluene; temperature, 77 K. 31

Figure 2.9 Crystal structure of **5**. The hydrogens, imido *tert*-butyl groups, solvent molecules and a crystallographically unique but structurally analogous molecule of 5 are omitted for clarity. Thermal ellipsoids are drawn at 50% probability. 33

Figure 2.10 Mössbauer spectrum of {[ONO^{q}]Fe(«-N^{t}Bu)}$_2$ (**5**). Data collected at 95 K. 34

Figure 2.11 Crystal structure of **6**. The hydrogens and two crystallographically unique but identical crystal structures of 6 are removed for simplicity. Thermal ellipsoids are drawn at 50% probability. 36

Figure 2.12 X-band EPR spectrum of $[ONO^{cat}]Fe(dppe)$ (**6**). Experimental conditions: $B_1 \perp B_0$; solvent, toluene; temperature, 77 K. 37

Figure 2.13 Crystal structure of $[ONO^{cat}]Fe(py)_3$ (**7**). Hydrogen atoms, solvent molecules, and a crystallographically unique but structurally analogous molecule of **7** have been omitted for clarity. Thermal ellipsoids are drawn at 50% probability. 38

Figure 2.14 (*Left*) Mössbauer spectrum of $[ONO^{cat}]Fe(py)_3$ (**7**). Data collected at 90 K. (*Right*) X-band EPR spectrum of **7**. Experimental conditions: $B_1 \perp B_0$; solvent, pyridine; temperature, 77 K. 40

Figure 3.1 Crystal structure of **8** (*a*) and **9** (*b*). Thermal ellipsoids shown at 50% probability. Hydrogen atoms and solvent molecules have been omitted for clarity. 56

Figure 3.2 X-band EPR spectrum of $[ONO^{q}]Fe(cat\text{-}Cl_4)(py)$ (**9**; black) and simulation (red). Experimental conditions: $B_1 \perp B_0$; solvent, toluene; temperature, 4 K. 58

Figure 3.3 ORTEP diagram of complex **10**. Hydrogen atoms and *tert*-butyl groups have been omitted for clarity. Thermal ellipsoids are shown at 50% probability. 62

Figure 3.4 ESI/MS chromatograms of $[ONO^{q}]FeCl_2$ (**3a**; left), $[ONO^{q}]FeBr_2$ (**3b**; center), $[ONO^{q}]FeI_2$ (right). 65

Figure 4.1 The XDK ligand used by Lippard and coworkers to prepare new bimetallic complexes. 79

Figure 4.2 ORTEP diagram of **11**. Thermal ellipsoids are displayed at 50% probability. The hydrogen atoms and solvent molecules have been removed for simplicity. 82

Figure 4.3 X-band EPR spectrum of $[ONO^{sq}]Zn(py)_2$ (**11**). Experimental conditions: $B_1 \perp B_0$; solvent, toluene or pyridine; temperature, 77 K. 83

Figure 4.4 ORTEP diagram of **12** (*a*) and **13** (*b*). Thermal ellipsoids are displayed at 50% probability. The *tert*-butyl groups, hydrogen atoms, and solvent molecules have been removed for simplicity. 86

Figure 4.5 Mössbauer spectrum of $Fe_2[ONO]_3$ (**12**). Data collected at 80 K. 87

Figure 4.6 Cyclic (*left*) and differential pulse (*right*) voltammograms of $[ONO^{q}]FeCl_2$ (**3a**; magenta), $Fe_2[ONO]_3$ (**12**; red), **(13**; blue), $[ONO^{sq}]Zn(py)_2$ (**11**; green), and $Fe[ONO]_2$ (purple). Bulk of the 91 material indicated by *. Voltammograms were recorded at 1mM analyte concentration in 0.10 M [^{n}Bu$_4$N][PF$_6$] in THF using a glassy carbon working electrode, Pt wire counter electrode, Ag$^{0/+}$ wire reference, and scan rate of 200 mV/s at 298 K.

Figure 4.7 UV-vis-NIR spectra of $Fe_2[ONO]_3$ (**12**; red), $FeZn[ONO]_3$ (**13**; blue), and $Fe[ONO]_2$ (purple). 91

Figure 5.1 Crystal structure of **14**. Solvent molecules and hydrogen atoms are removed for clarity. Thermal ellipsoids are drawn at 50% probability. 107

Figure 5.2 Crystal structure of **15**. Solvent molecules and hydrogen atoms are removed for clarity. Thermal ellipsoids are drawn at 50% probability. 109

Figure 5.3 Absorption spectra of Cr(dmp-ADI^{sq})$_3$ (**14**; black) and Cr(dmp-PDI^{sq})$_3$ (**15**; red) collected in THF. 110

Figure 5.4 X-band EPR spectra of Cr(dmp-ADI^{sq})$_3$ (**14**; black) and simulation (red). Experimental conditions: $B_1 \perp B_0$; solvent, THF; temperature, 298 K. 111

Figure 5.5 X-band EPR spectra of Cr(dmp-PDI^{sq})$_3$ (**15**). Experimental conditions: $B_1 \perp B_0$; solvent, THF; temperature, 77 K. 111

Figure 5.6 Cyclic voltammograms (*left*) of Cr(dmp-ADI^{sq})$_3$ (**14**; black) and Cr(dmp-PDI^{sq})$_3$ (**15**; red) and differential pulse voltammogram (*right*) of **15**. Bulk of the material denoted by *. Voltammograms were recorded at 1mM analyte concentration in 0.10 M [^{n}Bu$_4$N][PF$_6$] in THF using a glassy carbon working electrode, Pt wire counter electrode, Ag$^{0/+}$ wire reference, and scan rate of 200 mV/s at 298 K. 113

LIST OF TABLES

Page

Table 2.1 Selected bond lengths (Å) and angles (°) of **1**. 21

Table 2.2 Selected bond lengths (Å) and angles (°) of **2**. 23

Table 2.3 Selected bond lengths (Å) and angles (°) of **3a** and **3b**. 27

Table 2.4 Selected bond lengths (Å) and angles (°) of **4**. 31

Table 2.5 Selected bond lengths (Å) and angles (°) of **5**. 33

Table 2.6 Selected bond lengths (Å) and angles (°) for **6**. 36

Table 2.7 Selected bond lengths (Å) and angles (°) of **7**. 39

Table 2.8 X-ray diffraction data-collection and refinement parameters for complexes **1**, **2**, **3a**, **3b**. 45

Table 2.9 X-ray diffraction data-collection and refinement parameters for complexes **4**, **5**, **6**, **7**. 46

Table 3.1 Selected bond lengths (Å) and bond angles (°) of **8** and **9**. 56

Table 3.2 Selected bond lengths (Å) and bond angles (°) of **10**. 62

Table 3.3 X-ray diffraction data-collection and refinement parameters for complexes **8**, **9**, **10**. 69

Table 4.1 Selected bond lengths (Å) and angles (°) of **11**. 82

Table 4.2 Selected bond lengths (Å) and angles (°) of **12** and **13**. 86

Table 4.3 X-ray diffraction data-collection and refinement parameters for complexes **11**, **12**, **13**. 96

Table 5.1 Selected bond lengths (Å) and angles (°) of **14**. 107

Table 5.2 Selected bond lengths (Å) and angles (°) of **15**. 109

Table 5.3 Redox potentials vs. $[Cp_2Fe]^{0/+}$ for Cr(dmp-ADI^{sq})$_3$ (**14**) and Cr(dmp-PDI^{sq})$_3$ (**15**). 113

Table 5.4 X-ray diffraction data-collection and refinement parameters for complexes **14** and **15**. 117

LIST OF SCHEMES

Page

Scheme 1.1 (*a*) Resonance structure of square-planar nickel complexes containing two dithiobenzil ligand moieties prepared by Schrauzer and Mayweg. (*b*) Ligand non-innocence in nickel dithiolene complexes. 3

Scheme 1.2 Three accessible oxidation states of the catechol-type and *ortho*-phenylenediimine ligands. 4

Scheme 1.3 Ligand-enabled oxidative addition and reductive elimination reactivity at d^0 metal center. 6

Scheme 1.4 (*a*) Oxidation states of the tetradentate [N_2N_2] ligand platform. (*b*) Ligand substitution reactions of [$N_2N_2^{cat}$]$TiCl_2$. 7

Scheme 1.5 Proposed mechanism extradiol dioxygenases. 9

Scheme 1.6 Proposed catalytic cycle by Kochi *et al*. for iron-catalyzed cross-coupling reactions. 10

Scheme 1.7 Proposed catalytic cycle by Fürstner *et al.* for iron-catalyzed cross-coupling reactions. 10

Scheme 1.8 Electronic arrangements of [PDI]$Fe(N_2)_2$ and the catalytic cycloaddition of dienes mediated by [PDI]$Fe(N_2)_2$. 11

Scheme 2.1 Reduction of [PDI]$FeBr_2$ to form resulting iron bis(dinitrogen) complex. Resonance is shown here to highlight the redox non-innocent nature of the compound. 18

Scheme 2.2 Synthetic routes towards accessing the various oxidation states of the [ONO] ligand. 19

Scheme 2.3 Synthesis of **2** from metathesis of **1** and K_2[ONHO]. 21

Scheme 2.4 Deprotonation and oxidation of complex **2** using various bases and oxidants. All reactions were carried out at ambient temperature using either THF, pentane, or diethyl ether solvents. 25

Scheme 2.5 Synthesis of [ONO^q]FeX_2 complexes. 26

Scheme 2.6 Synthesis of [ONO^{cat}]FeL_n complexes. 35

Scheme 2.7 Deprotonation and oxidation of **2** leading to putative iron product containing two possible isomers. 41

Scheme 3.1 Catalytic nitrene transfer reactivity mediated by Zr(IV) coordinated to a redox-active ligand. 53

Scheme 3.2 Synthesis of **8** and **9** from protonolysis of **4**. 55

Scheme 3.3 Reductions of **3a** and **4** in the presence of excess pyridine to produce **7**. 59

Scheme 3.4 Reductions of **3a** and **4** in the absence of pyridine to produce the diiron complex $Fe_2[ONO]_3$. 60

Scheme 3.5 Equilibrium between **7** and **10** in non-pyridine solvents. 63

Scheme 3.6 Ligand substitution and oxidative-addition reactivity of **7**. 64

Scheme 3.7 Proposed mechanism to form **5** through treatment of **7** with *tert*-butyl azide. 66

Scheme 4.1 Stepwise synthesis of bimetallic complexes based on dinucleating diphenoxide-based ligand scaffold. 79

Scheme 4.2 Synthesis of complex **11**. 81

Scheme 4.3 Reductions of $[ONO^q]FeCl_2$ in presence or absence of pyridine. 84

Scheme 4.4 Synthesis of complex **12**. 84

Scheme 4.5 Synthesis of complex **13**. 89

Scheme 4.6 Alternative synthetic pathways for preparing **13**. 89

Scheme 5.1 (a) The three accessible oxidation states of dioxolene ligands. (b) Homoleptic tris-semiquinonate complexes of chromium(III). 103

Scheme 5.2 Three accessible oxidation states of the (dmp-ADI) and (dmp-PDI) ligand scaffolds (dmp = 3,5-dimethylphenyl). 104

Scheme 5.3 Synthesis of complex **14**. 105

Scheme 5.4 Synthesis of complex **15**. 108

Scheme 5.5 Redox series of tris-iminosemiquinonate complexes of chromium(III). 115

LIST OF CHARTS

Page

Chart 1.1 Examples of dioxolene ligands in their neutral forms. 5

Chart 1.2 Examples of ~-diimine ligands in their neutral forms. 5

Chart 5.1 Chromium polymer catalysts containing (ar-ADI^{sq})$^{1-}$ and (ar-PDI^{sq})$^{1-}$ coordinated to single metal centers. 104

ACKNOWLEDGEMENTS

Words cannot convey my deepest gratitude for everyone that has played a positive role in my graduate studies experience. First and foremost, I must thank my family. The virtues of hard work and perseverance imparted by my grandparents and my parents are the reason why I always strive to overcome any hardships. In addition, despite all the tough times my brother and I have given each other as siblings, it is the bond we've developed over our lifetime that has helped us learn to appreciate the good things in life, and for that I must also thank my brother for his support. Thanks to my uncles, aunts, and cousins who constantly shower me with love and encouragements. A shout out to all the wonderful friends who continue to be my true friends - whether we've only known each other for a year, five years, fifteen years, or more. Thanks for making my journey through graduate school and the road leading up to it so much easier.

I am extremely grateful to Professor Alan Heyduk for his mentorship, support, and firm belief in my capacity to succeed in graduate school. Whenever I hit a rough patch, your honest words of wisdom always steered me back to the right path. Under your tutelage throughout the years, you have imparted me with your incredible sense of creativity when it comes to tackling complicated scientific problems. I would never have become the scientist I am today without you.

Professors Andy Borovik and Bill Evans have also played important roles during my time at UCI and beyond. In addition to serving on my advancement and dissertation committees, you have provided me with invaluable scientific and career advice. Thank you for all your support.

The data I have presented in this dissertation would not have been possible without the dedication of the facilities managers at UCI and several research groups. Thank you to Professor Andy Borovik and the Borovik group for the use of and assistance with their EPR spectrometer. In particular, Dr. David Lacy has been instrumental in helping me become proficient with using the instrument and grasping the concepts behind EPR spectroscopy. I am also indebted to Dr. Joseph Ziller for his persistence when it comes to finding that perfect crystal to mount on the diffractometer. Thank you Dr. John Greaves and Dr. Beniam Berhane for helping me with any questions I have regarding collecting mass spectrometry data. In addition to having a myriad of resources at my disposal at UCI, I have been fortunate to have the opportunity to collaborate with the Betley group at Harvard University and have access to their Mössbauer spectrometer. In particular, Raúl Hernández Sánchez has been a wonderful colleague for collecting and analyzing all of my data as well as helping me understand the concepts underlying Mössbauer spectroscopy.

My growth and success in graduate school would also not have been possible without the mentorship, friendship, and support of past and current members of the Heyduk group. As a first year graduate student, I was privileged to have benefitted from the generous guidance of my patient mentor, Dr. Géza Szigethy, who always encouraged me to persevere when things got tough in the lab. In the ensuing years, I've had the pleasure of experiencing the evolution of the Heyduk group as it develops into my awesome second family where we can always rely on one another. I would like to acknowledge David Cao who synthesized and characterized the bimetallic complex $FeZn[ONO]_3$ (**13**) and for proofreading this acknowledgement. Finally, I am very appreciative of my friends and colleagues who have edited my thesis: Dr. Rui Munhá, Dr. David Shaffer, Aaron Hollas, Mikey Wojnar, Lindsay Cameron, Kyle Rosenkoetter, and Mike Klosterman.

Lastly, I want to express my appreciation to the Taihi Hong Memorial Graduate Student Education Award for travel assistance to the 245th ACS National Meeting as well as UCI Regent's Dissertation Fellowship for funding during my last quarter at UCI.

CURRICULUM VITAE

Janice L. Wong, Ph.D.

Education:

University of California, Irvine, CA 2009 – 2014

Ph.D. candidate, Chemistry

Ph.D. dissertation: Synthesis and Reactivity of Iron Complexes Supported by Redox-Active Pincer-Type Ligands

San Jose State University, San Jose, CA 2004 – 2008

B.S., General Chemistry; Minor, Environmental Studies.

Research Experience:

University of California, Irvine, Department of Chemistry 2009 – 2014

Graduate Research Advisor: Prof. Alan F. Heyduk

- Prepared air- and moisture-sensitive early-transition metal and iron complexes using Schlenk line and glovebox techniques.
- Elucidated the complicated structures of the electronically non-innocent iron complexes using various analytical methods, including X-ray crystallography, UV-Vis-NIR, Mössbauer and electron paramagnetic resonance (EPR) spectroscopies, and cyclic and differential pulse voltammetry.
- Performed mechanistic studies to explore the multi-electron reactivity of the redox-active iron(III) complexes using GC and GC/MS techniques.
- Mentored and advised undergraduate and junior graduate members on designing experiments, using lab techniques, and analyzing data.
- Maintained laboratory equipment including gloveboxes and vacuum pumps.
- Managed chemical and supply inventory in the laboratory.
- Interacted with sales representatives to negotiate best prices for chemicals, equipments, and supplies.

San Jose State University, Department of Chemistry 2007 – 2009

Undergraduate Research Advisor: Prof. David. J. R. Brook

- Applied ^{1}H NMR technique to monitor coordination of Zn^{II} metal to a series of novel hydrazone ligands containing pyrazine cores with the goal of generating new molecular geometries to investigate the metal–ligand interactions.

San Jose State University, Department of Physics 2007 – 2009

NSF-REU in Physics Jun. 2008 – Dec. 2008

Undergraduate Research Advisor: Prof. Carolus Boekema

- Applied Maximum Entropy (MaxEnt) technique on the high-T$_c$ superconductor gadolinium barium copper oxide ($GdBa_2Cu_3O_7$) to study its magnetic properties through muon spin resonance data analysis.

Publications:

1. **Wong, J. L.**; Cao, D. X.; Szigethy, G.; Sánchez, R. H.; Zarkesh, R. A.; Ziller, J. W.; Heyduk, A. F. "Synthesis and Characterization of Homobimetallic and Heterobimetallic Complexes Supported By Redox-Active Ligands." *Manuscript in Preparation*.

2. **Wong, J. L.**; Sánchez, R. H.; Logan, J. G.; Zarkesh, R. A.; Ziller, J. W.; Heyduk, A. F. "Disulfide Reductive Elimination From an Iron(III) Complex." *Chem. Sci.* **2013**, *4*, 1906−1910.
3. Brook, D. J. R.; Yee, G. T.; Hundley, M.; Rogow, D.; **Wong, J.**; Tu, K. V. "Geometric Control Of Ground State Multiplicity In a Copper(I) Bis(Verdazyl) Complex." *Inorg. Chem.* **2010**, *18*, 8573–8577.
4. Songatikamas, T.; Boekema, C.; **Wong, J.**; Ngo, H.; Browne, M. C. "Predicted Magnetic Fields of Loop Currents For Cuprate Superconductivity: A MaxEnt-μSR GdBCO Study." *J. Supercond. Nov. Magn.* **2010**, *23*, 793–797.

Contributed Presentations:

1. **Wong, J. L.**; Heyduk, A. F. "Ligand-Based Multi-Electron Reactivity Of Redox-Active Iron Complexes." 245th American Chemical Society National Meeting, New Orleans, LA, April 11, 2013. (*Oral Presentation*)
2. **Wong, J. L.**; Heyduk, A. F. "Iron Complexes Containing the Redox-Active [ONO] Ligand." 243rd American Chemical Society National Meeting, San Diego, CA, March 25, 2012. (*Oral Presentation*)
3. **Wong, J. L.**; Heyduk, A. F. "Backbone Effects On Ligand Redox Activity In Homoleptic Chromium(III) Complexes." 241st American Chemical Society National Meeting, Anaheim, CA, March 28, 2011. (*Poster Presentation*)
4. **Wong, J. L.**; Brook, D. J. R. "NMR Studies of Ditopic Hydrazone Ligands With a Pyrazine Core." 237th American Chemical Society National Meeting, Salt Lake City, UT, March 23, 2009. (*Poster Presentation*)
5. **Wong, J.**; Songatikamas, T.; Norris, R.; Boekema, C. "MaxEnt-μSR Study Of GdBCO: Potential Precursor Effects." March 2008 American Physical Society National Meeting, New Orleans, LA, March 11, 2008. (*Poster Presentation*)

Teaching Experience:

University of California, Irvine, Department of Chemistry

- *Teaching Assistant, Advanced Inorganic Laboratory* Winters 2013 and 2014
  Instructed students in standard Schlenk line and glovebox techniques in seven-hour laboratory sections with 10–12 students. Taught students how to interpret spectroscopic data.
- *Teaching Assistant, General Chemistry Lecture* Spring 2011, Fall 2013
  Taught students fundamental chemistry principles. Led six one-hour discussion sections each week for 20–30 students. Created worksheets and developed problems for review. Prepared and graded exams.
- *Teaching Assistant, Organic Chemistry Laboratory* Fall 2009, Winters 2010 − 2012
  Instructed students in using standard synthetic techniques in two weekly four-hour laboratory sections with 15-20 students. Taught students how to interpret spectroscopic data.
- *Teaching Assistant, General Chemistry Laboratory* Spring 2010
  Instructed students in the use of various instruments during two weekly four-hour laboratory sections with 20-24 students.

San Jose State University, Learning Assistance Resource Center

- *Instructional Student Assistant* 2006 – 2008
  Assisted SJSU students with math, chemistry, physics. Subjects tutored include general and introductory chemistry courses offered at SJSU.

Awards and Professional Affiliations:

- UCI Regents' Dissertation Fellowship Spring 2014
- Taihi Hong Memorial Graduate Student Education Award Nov. 2012
- American Chemical Society (ACS)
- Iota Sigma Pi (ISP)

Leadership Experience:

Outreach Coordinator, UCI Calcium Chapter of ISP 2011 – 2013

- Coordinate with staff members of various organizations, including Girls Inc. of Orange County and Orange County ACS National Chemistry Week, to organize science-related activities for young children.
- Help design various hands-on experiments, such as making your own butter and extracting DNA from strawberries, to stimulate interest in science for young minds.

ABSTRACT OF THE DISSERTATION

Synthesis, Characterization, and Reactivity Studies of Iron Complexes Supported By the Redox-Active [ONO] Ligand

By

Janice Lin Wong

Doctor of Philosophy in Chemistry

University of California, Irvine, 2014

Professor Alan F. Heyduk, Chair

The work reported herein primarily focuses on the development of new platforms for multi-electron reactivity using iron complexes supported by a redox-active pincer-type ligand. This dissertation details the synthesis, characterization, and reactivity of iron complexes coordinated to the redox-active [ONO] ([ONO]H_3 = bis(3,5-di-*tert*-butyl-2-phenol)amine) ligand.

Chapter 1 provides a general background on ligand-centered and metal-centered redox reactivity. Specifically, the characteristics of redox-active ligands and their ability to promote multi-electron reactivity at redox-inert metal centers is presented. In addition, iron-catalyzed organic transformations in which the metal center undergoes redox changes is also discussed. Finally, ligand-enabled redox reactions mediated by iron complexes containing redox-active ligands is described.

Chapter 2 reports on the complexation of bis(3,5-di-*tert*-butyl-2-phenoxy)amine, [ONHO], and the redox-active [ONO] ligands by iron centers to afford a new family of iron complexes. Characterizations of each compound through a battery of analytical techniques reveal the oxidation states of the metal center and ligand. Furthermore, the electronic properties of each complex were investigated in order to evaluate their potential to facilitate multi-electron reactivity.

Chapter 3 details the reactivity of the [ONO]Fe platform. Metathesis reactions are conducted with $[ONO^{q}]Fe^{III}X_2$ (X = Cl, $N[SiMe_3]_2$) complexes, demonstrating the capability of the fully-oxidized $[ONO^{q}]^{1-}$ to act as a two-electron acceptor to generate the fully reduced $[ONO^{cat}]^{3-}$ that is coordinated to an iron(III) center. Similarly, oxidation of $[ONO^{cat}]Fe^{III}(py)_3$ (py = pyridine) using dihalogens result in two-electron oxidations of the tridentate ligand while the metal oxidation state remains the same. These redox reactions showcase the ability of the [ONO] ligand platform to undergo reversible two-electron oxidation state changes, allowing multi-electron reactivity to occur at the iron center.

The synthesis and characterization of two novel bimetallic complexes of the form $[ONO]M'[ONO]_2M$ (M' = Fe, Zn; M = Fe) are presented in Chapter 4. The rich redox profiles of both complexes suggest that they can potentially impart unique cooperative bimetallic reactivity. The synthetic techniques developed to prepare these complexes lay the foundation for a general method to access new bimetallic combinations that could be promising for multi-electron reactivity.

Finally, Chapter 5 discusses the synthesis, characterization, and electronic comparisons between two homoleptic tris-iminosemiquinonate chromium(III) compounds. While one is coordinated to three *N,N'*-bis(3,5-dimethylphenyl)acenapthenediimino-semiquinonate, $(dmp\text{-}ADI^{sq})^{1-}$, ligands, the other contains three *N,N'*-bis(3,5-dimethylphenyl)phenanthrenediimino-semiquinonate, $(dmp\text{-}PDI^{sq})^{1-}$, ligands. The differences in the electronic properties between each complex likely stems from variation in the diimine ligand backbones. However, further investigation is required to completely understand the complicated behaviors of such complexes, both of which apparently exhibit intramolecular anti-ferromagnetic properties.

Chapter 1

Introduction

1.1 Overview of Redox-Active Ligands and Their Enabled Reactivity

Transition-metal complexes containing "non-innocent" ligands have been the subject of intense research for almost fifty years. In his seminal review published in 1966, Jørgensen coined the term "innocent ligands" when referring to ligands that allowed "oxidation states of the central atoms to be defined."[1,2] For example, *cis*-[$Co(NH_3)_4Cl_2$], a classic Werner-type compound, possesses four neutral L-type and two anionic X-type ligands to provide a Co(II) complex. The ability to classify and assign oxidation states to the ligands allow for subsequent determination of the metal oxidation state. Ligands that are non-innocent, on the other hand, often lead to ambiguity in assigning oxidation states to the metal and ligand entities.[3] Namely, when complexes containing non-innocent ligands are oxidized or reduced, it is difficult to discern whether the oxidation state changes are metal- or ligand-based. This concept is usually apparent in cases where mid- and late-transition metal ions are coordinated to non-innocent ligands.[4] Owing to the favorable overlap between the valence orbitals of the metal and coordinated ligand, the valence electrons of their complexes can readily come from either the metal or ligand. The term "redox-active" is often used interchangeably with non-innocent, although this expression is generally reserved for describing ligands that can exist in multiple stable oxidation states.[5] This term is most appropriate when referring to complexes in which the metal only has one accessible oxidation state and is considered "redox-inert". In this case, redox changes to the overall metal complex are limited to the ligand, allowing formal oxidation states to be made for the metal.

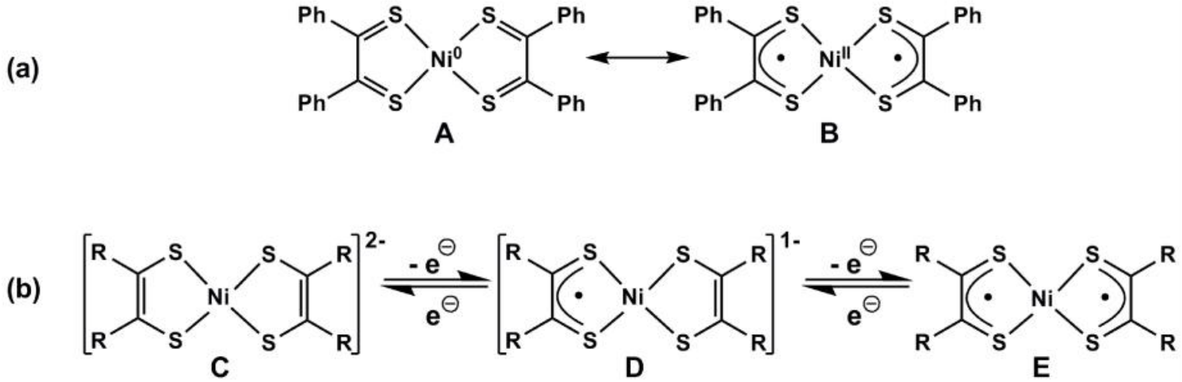

Scheme 1.1. (*a*) Resonance structure of square-planar nickel complexes containing two dithiobenzil ligand moieties prepared by Schrauzer and Mayweg. (*b*) Ligand non-innocence in nickel dithiolene complexes.

One of the first examples of complexes with ligands exhibiting non-innocent behaviors comprised a family of nickel dithiolene complexes.[2] As presented in Scheme 1.1, Schrauzer and Mayweg surmised that coordination of two neutral dithiobenzil ligands to the nickel center should lead to a formal Ni(0) metal center (**A**).[6] However, magnetic measurements supported a square-planar Ni(II) system, suggesting that each dithiobenzil was singly-reduced to form a radical residing in each ligand (**B**). Gray and coworkers later prepared a number of dianionic nickel dithiolene complexes (**C**) which were structurally analogous to the neutral nickel dithiolene compounds (**E**), but differ by two electrons.[7] Subsequently, Davison, *et al.* isolated several monoanionic nickel dithiolene complexes (**D**) which could then be transformed into either the dianionic (**C**) or neutral (**E**) forms via electron transfer processes, demonstrating the facile single-electron redox activity of these nickel species.[8] Careful analyses through molecular orbital calculations revealed a substantial degree of metal–dithiolene covalency and established the primarily ligand-based character of the frontier orbitals of these complexes.[9] Because of this peculiarity, oxidation changes of such complexes mainly occurred at the ligand rather than the metal center.

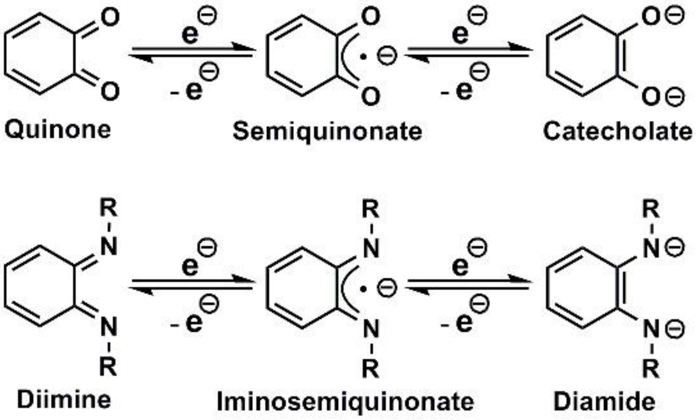

Scheme 1.2. Three accessible oxidation states of the catechol-type and *ortho*-phenylenediimine ligands.

In the ensuing decades, a number of complexes containing transition-metal ions coordinated to various redox-active ligand moieties have been developed to further understand the metal-ligand interplay of such systems. Archetypal models include metal complexes supported by the "dioxolene" ligand set, a term that was introduced by Balch to describe the oxygen-containing analogues of dithiolenes.[10] As illustrated in Scheme 1.2, the catechol-type ligands, perhaps one of the most well-studied dioxolene ligands, possess three viable oxidation states.[11] Upon coordination to a metal ion, the catecholate, semiquinonate, and quinone forms of the ligand act as dianonic, monoanionic, and neutral donors, respectively. In subsequent years, the catechol-type ligand family has expanded to include those with polycyclic π-conjugated backbones (Chart 1.1). As demonstrated through the *ortho*-phenylenediimine platform in Scheme 1.2, ligands of the ~-diimine form also have three accessible oxidation states: doubly-reduced diamide, π radical iminosemiquinonate, and neutral diimine.[12] In contrast to their dithiolene and dioxolene congeners, the ability to vary the substituent bound to each nitrogen donor atom of the ~-diimine ligand permits the structural and electronic profiles of their complexes to be modified. This has led to the development of a range of derivatives based on the phenylenediimine moiety, including those containing extended π-conjugated backbones as well as those with non-extended π systems (Chart 1.2).[12]

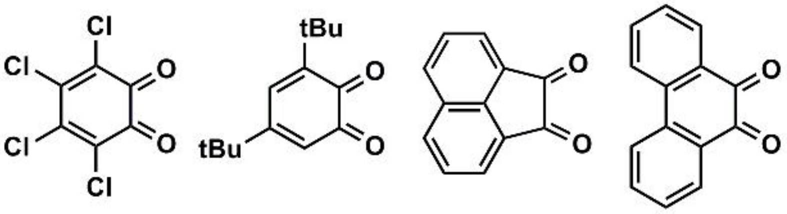

Chart 1.1. Examples of dioxolene ligands in their neutral forms.

Chart 1.2. Examples of ~-diimine ligands in their neutral forms.

To enhance the fundamental understanding of transition metal complexes supported by redox-active ligands, the complicated behaviors of such systems have been explored extensively through a wide range of spectroscopic and computational techniques.[13, 14] These studies reveal a great deal of orbital mixing between the ligand-based π orbitals and metal-based *d* orbitals within such complexes. This behavior may be responsible for the observed formal redox changes in metallated non-innocent ligands, an implication that redox-active ligands can act as electron reservoirs when coordinated to metal ions. The ability of redox-active ligands to behave as electron donors and acceptors has been exploited for the purposes of multi-electron reactivity.

Early work in our group aimed at utilizing redox-active ligands to promote two-electron reactivity at redox-inert d^0 metal centers.[15] As depicted in Scheme 1.3, treatment of $\mathrm{Zr^{IV}(ap)_2(THF)_2}$ ($\mathrm{(ap)^{2-}}$ = 4,6-di-*tert*-butylamidophenolate) with one equivalent of $\mathrm{PhICl_2}$ leads to addition of two chloride ligands to the metal center accompanied by single-electron oxidations at each (ap) ligand to produce $\mathrm{Zr^{IV}(ap^{sq})Cl_2}$.[16] Addition of two equivalents of PhLi to

$Zr^{IV}(ap)_2(THF)_2$ displaces the THF ligands and forms $Li_2[Zr(ap)Ph_2]$, which is then oxidized by two electrons to produce $Zr^{IV}(ap^{sq})Ph_2$.[17] Subsequent extrusion of biphenyl and association of two THF regenerates $Zr^{IV}(ap)_2(THF)_2$. Chelation of the redox-active (ap) ligand to the d^0 zirconium(IV) metal center allows for bond-breaking and forming processes to occur at the metal coordination sphere. While the metal oxidation states remain unchanged, both ligands undergo redox changes to facilitate two-electron molecular oxidative addition and reductive elimination reactions in a zirconium complex where zirconium(II) is not feasible.

However, it soon became apparent that oxidation of d^0 metal complexes containing (ap) ligands produces the coordinatively labile monoanionic or neutral forms of the ligand, leading to product decompositions.[18] For instance, solutions containing $Zr^{IV}(ap^{sq})Cl_2$ are unstable over time, resulting in ligand exchange to form product mixtures. Furthermore, four-electron oxidations of $Zr^{IV}(ap)_2(THF)_2$ result in unstable coordination environments wherein the metal dissociates from the iminoquinone ligands.[16]

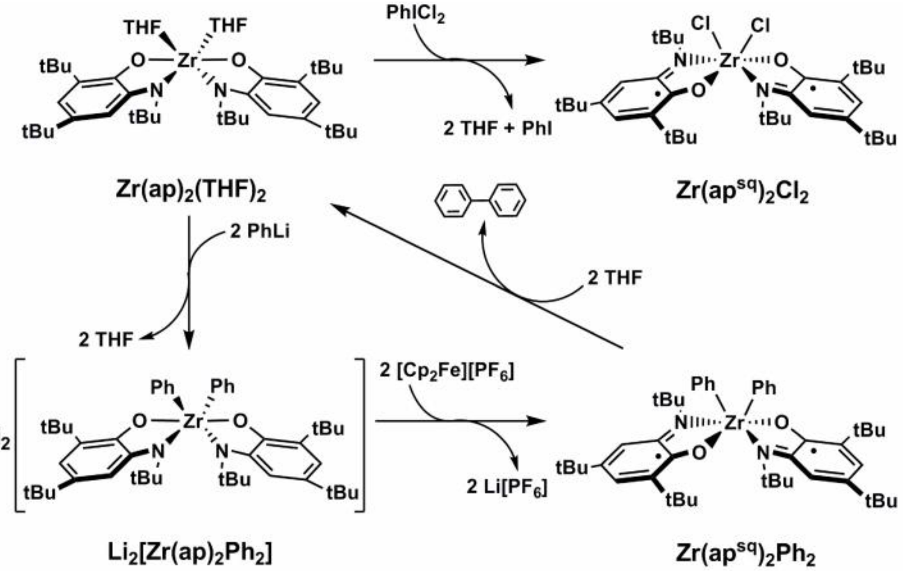

Scheme 1.3. Ligand-enabled oxidative addition and reductive elimination reactivity at d^0 metal center.

To prevent metal dissociation upon oxidation of the ligand platform, our group has developed an array of redox-active tridentate and tetradentate ligands. The tetradentate $[N_2N_2]$

platform ($[N_2N_2^{cat}]^{2-}$ = *N*,*N'*-bis-(3-dimethylamino-propyl)-4,5-dimethoxy-benzene-1,2-diamide) developed in our laboratory exhibits redox behaviors akin to that of *ortho*-phenylenediimine, and as such the ligand also possesses three oxidation states (Scheme 1.4).[19] Upon metallation to a titanium(IV) center, the terminal amines situate in the apical positions of the metal center. However, in the presence of nucleophilic substrates the amine arms can be viewed as hemilabile ligands (Scheme 1.4). This provides a method for introducing new species to the metal coordination sphere, as demonstrated through the ligand exchange reactivity of $[N_2N_2^{cat}]TiCl_2$ wherein the terminal amines are displaced by two 4-dimethylaminopyridines in a stepwise manner. In addition, we have also investigated a series of metal complexes containing redox-active [ONO], [NNN], and [SNS] ligand platforms (Figure 1.1) which coordinate to the metal centers in a meridional fashion. Deprotonation of the neutral $[ONO]H_3$ results in a redox-active ligand moiety where the trianionic catecholate ($[ONO^{cat}]^{3-}$), dianionic semiquinonate ($[ONO^{sq}]^{2-}$), and monoanionic quinonate ($[ONO^{q}]^{1-}$) forms are attainable (Figure 1.1).[20] Analogous oxidation states have also been established for the [NNN] ligand[15, 21] whereas the redox activity of the recently-developed [SNS] ligand platform is currently under investigation.[22]

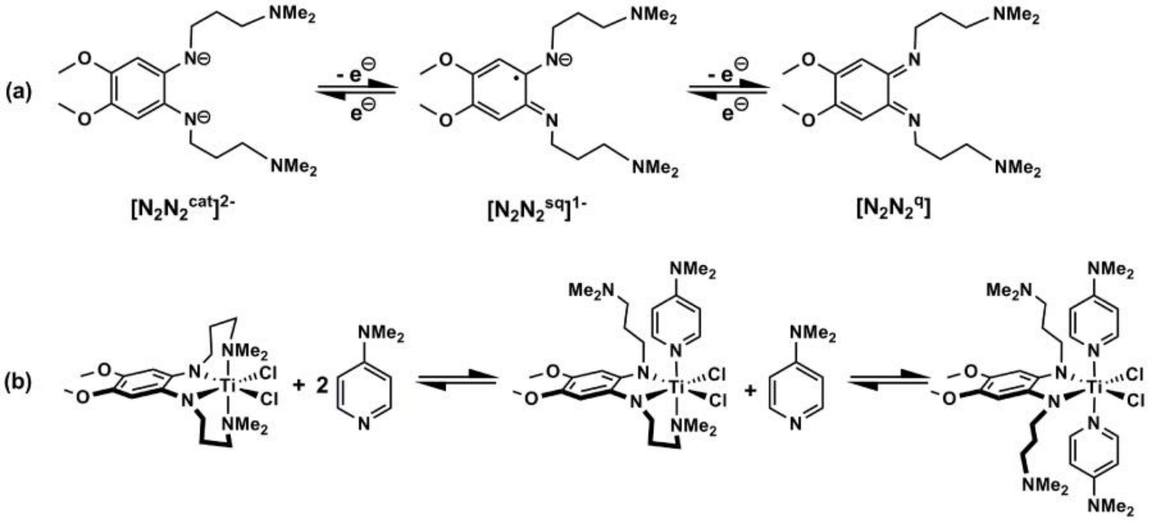

Scheme 1.4. (*a*) Oxidation states of the tetradentate $[N_2N_2]$ ligand platform. (*b*) Ligand substitution reactions of $[N_2N_2^{cat}]TiCl_2$.

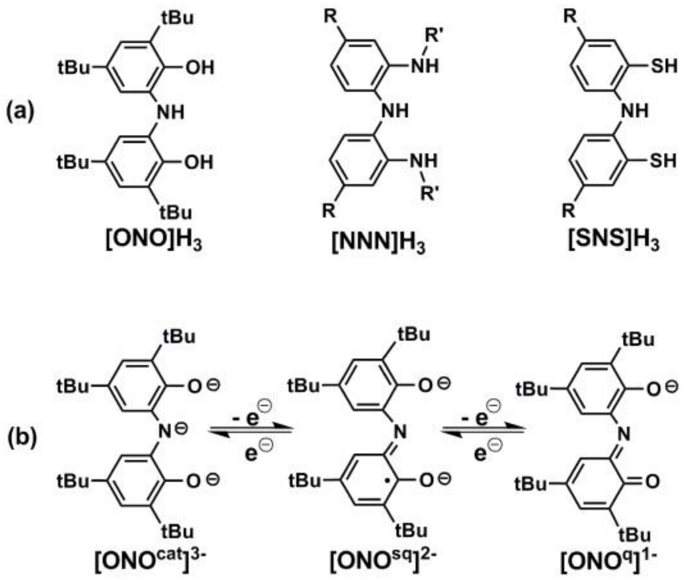

Figure 1.1. (*a*) Structural motifs for tridentate, pincer-type redox-active ligands. (*b*) Three accessible oxidation states of the [ONO] ligand.

1.2 Metal-Centered Redox Chemistry of Iron

The ability of iron-containing metalloenzymes to activate some of the strongest chemical bonds has inspired synthetic chemists to mimic these enzymes and understand their reactivity; specifically, iron can achieve a wide range of oxidation states from −2 to +6.[23, 24] For instance, several groups have endeavored to synthesize the key intermediates in oxygenases in which the oxidation states of iron range from +3 to formally +5.[23, 25] Conversely, iron is also capable of functioning at lower oxidation states of 0 to +2 as observed in nitrogenases.[26] The accessibility of iron's multiple oxidation states is a key aspect in transformations of biologically relevant molecules that involve multi-electron processes.

Redox-active ligands are also prevalent in biological systems,[27] and their presence alongside iron-containing systems often convolutes the exact determination of the metal and ligand oxidation states. This concept is showcased by the process in which the homoprotocatechuate 2,3-dioxygenase, an extradiol aromatic ring-cleaving dioxygenase, transfers the oxygen atoms of O_2 to the catechol ligand. Due to the readily accessible iron(III)/iron(II) redox couple as well as the fully- and partially-reduced forms of the catechol, understanding of the mechanism for extradiol dioxygenases has been relatively elusive.[25, 28] As described in Scheme 1.5, activation of oxygen likely begins with binding of O_2 to form the short-lived $Fe^{III}–O_2^{\bullet-}$ species. Subsequently, the catalytically active species $Fe^{II}–O_2^{\bullet-}$ is produced through intramolecular electron transfer steps that lead to the reduction of iron(III) to iron(II) accompanied by oxidation of the catechol to its semiquinone form.[25] The overall transformation involves a change not only in the oxidation state of the metal center, but of the redox-active ligand as well.

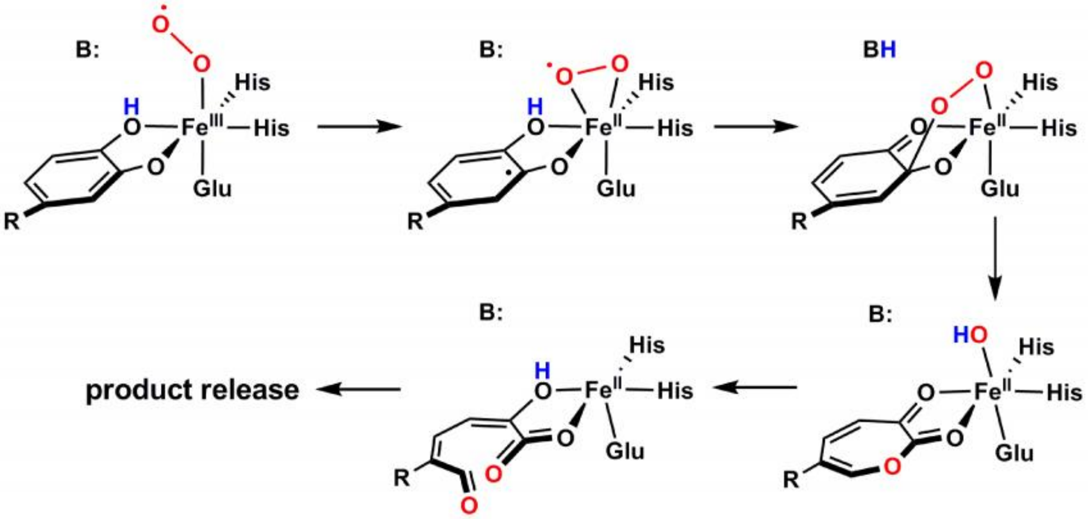

Scheme 1.5. Proposed mechanism extradiol dioxygenases.

In addition to the important roles of iron in organic transformations relevant to biological systems, there have been rising interests in using iron salts as cheaper and more environmentally-benign base-metal catalysts for cross-coupling reactions.[29, 30] However, insights into the mechanism for such reactions has been obscure.[31, 32] In 1971, the Kochi research group reported their pioneering studies on coupling alkenyl halides with Grignard reagents and proposed that the active catalyst is **A**, an Fe^{I} species generated from two-electron reductions of the Fe^{III} pre-catalyst (Scheme 1.6).[33] In contrast to the Fe(III)/ Fe(I) redox couple presumably operative under

Kochi's proposed mechanism, Fürstner and coworkers suggest that the Fe(II−)/ Fe(0) redox couple plays the operative role where the active catalyst is **D** in Scheme 1.7.[31] Since the in-situ formed active catalysts are highly reactive low-valent iron species, further interrogations of the mechanism of iron-catalyzed cross-coupling reactions are challenging. Nonetheless, the benefits of using non-toxic and more cost-effective metals to catalyze bond-forming reactions provides motivation for further development in the area of iron catalysis.

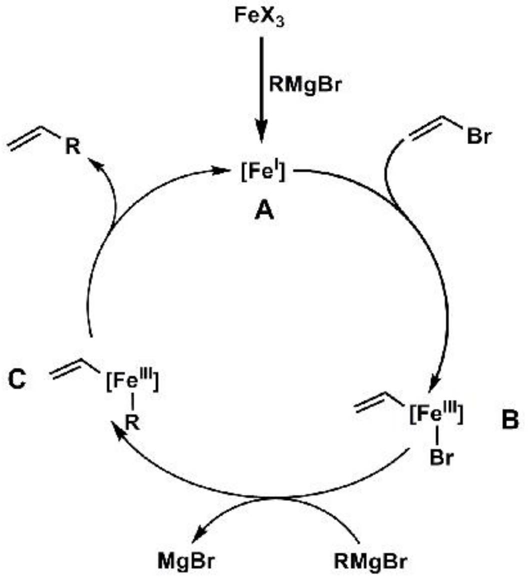

Scheme 1.6. Proposed catalytic cycle by Kochi *et al.* for iron-catalyzed cross-coupling reactions.

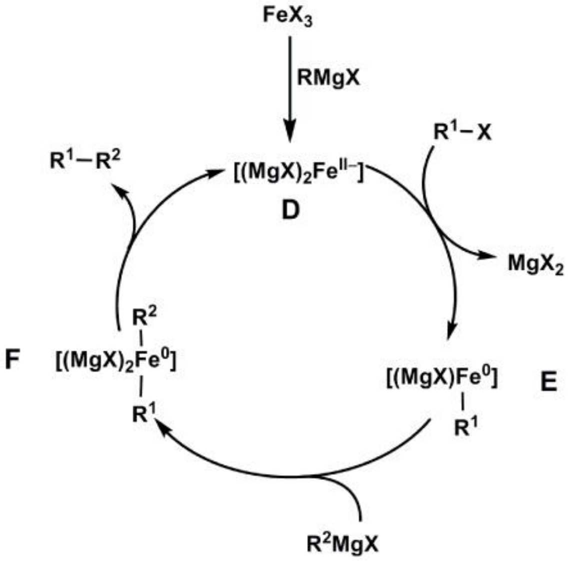

Scheme 1.7. Proposed catalytic cycle by Fürstner *et al.* for iron-catalyzed cross-coupling reactions.

1.3 Iron Complexes Supported by Redox-Active Ligands

One strategy to expand the use of base-metal complexes in catalytic organic transformations is through the use of redox-active ligands, as these ligands can provide the necessary reducing/oxidizing equivalents for such processes.[34] This view is highlighted in the catalytic [2π + 2π] cycloaddition of α,ω-dienes facilitated by [PDI]Fe(N_2)$_2$ ([PDI] = 2,6-pyridine diimine; Scheme 1.8).[35] Originally described as a formal iron(0) species (**A**),[36] the electronic properties of [PDI]Fe(N_2)$_2$ were interrogated through various analytical techniques and later established to be an iron(II) complex supported by the doubly-reduced ligand (**C**).[37] Taking advantage of the non-innocent behavior of the [PDI] platform, iron-mediated cyclization reactions have been carried out under mild conditions in which the transformations are mediated by ligand-centered processes while the metal oxidation state remains unaffected.[35] The electronic dexterity provided by the redox-active ligand has also enabled the hydrogenation and hydrosilation of organic substrates[36, 38] as well as cyclization of 1,6-enynes and diynes using [PDI]Fe(N_2)$_2$ as a catalyst.[39]

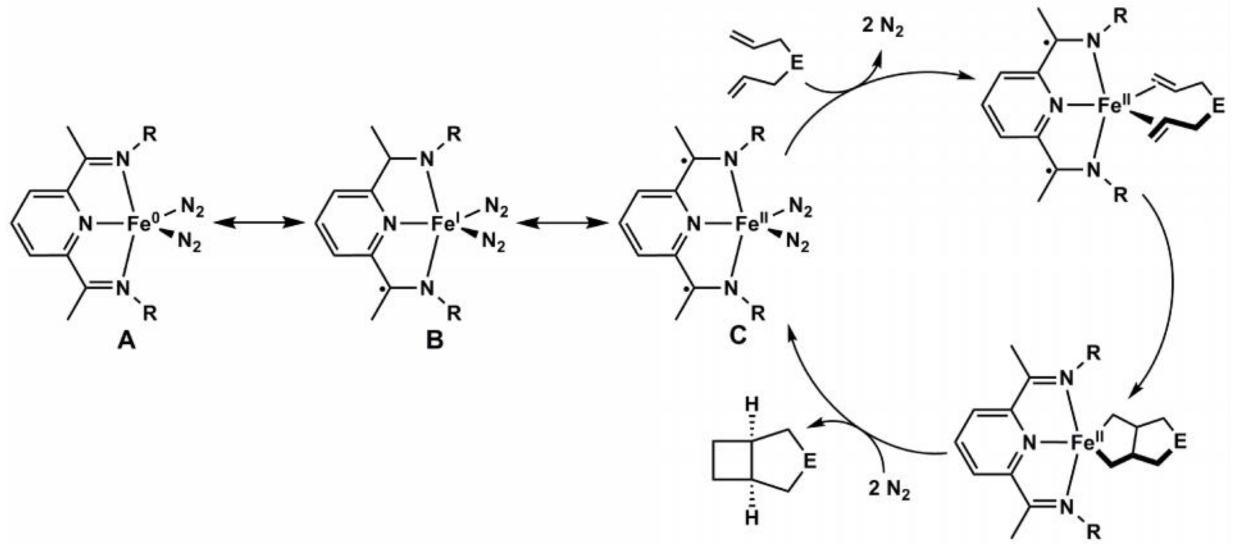

Scheme 1.8. Electronic arrangements of [PDI]Fe(N_2)$_2$ and the catalytic cycloaddition of dienes mediated by [PDI]Fe(N_2)$_2$.

More classic examples of iron complexes containing redox-active ligands include the homoleptic complexes containing catechol-type ligands (Figure 1.2). Six-coordinate iron complexes of the form Fe[SQ]$_3$ ([SQ] = 3,6-di-*tert*-butyl-1,2-semiquinonate or tetrachloro-1,2-semiquinonate) coordinated to three monoanionic π radical semiquinonate ligands.[40, 41] These complexes exhibit complicated magnetic behaviors owing to the exchange coupling between the ligand-based radicals and d^5 metal ion. Another example of a redox-active homoleptic iron complex is Fe[ONO]$_2$, which was first synthesized by Balch and coworkers in the 1970s and further characterized by Pierpont and coworkers fourteen years later.[42] EPR spectroscopic and X-ray crystallographic data indicate that the metal center is supported by $[\mathrm{ONO}^{q}]^{1-}$ and $[\mathrm{ONO}^{sq}]^{2-}$ (Figure 1.1) ligands, providing an iron(III) complex. In addition, Fe[ONO]$_2$ is able to support multi-electron redox changes as evidenced by the multiple reversible redox couples generated through cyclic voltammetry experiments.

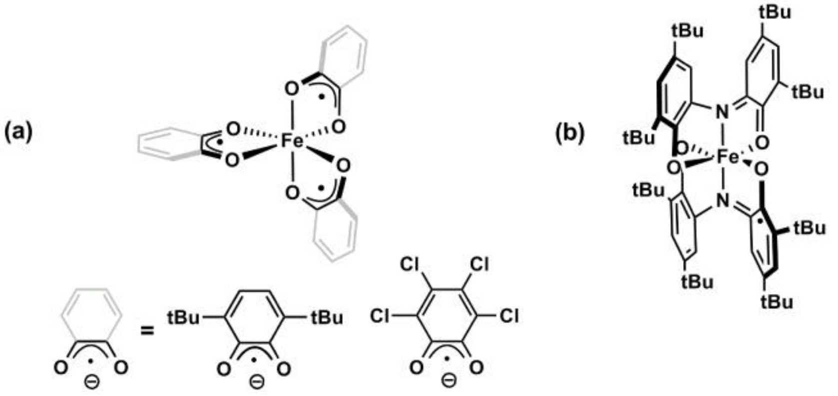

Figure 1.2. (*a*) Fe[SQ]$_3$ complexes. (*b*) Fe[ONO]$_2$ complex.

1.4 Contributions of This Dissertation

While the synthetic community has focused primarily on iron-centered redox chemistry, only a handful of synthetic systems have been developed that incorporate redox-active ligands into the coordination sphere of an iron center. The premise of this work is to develop new platforms for multi-electron reactivity using iron complexes supported by the redox-active [ONO] moiety. Chapters 2 and 3 will detail the synthesis and characterization of a series of iron complexes containing singly-coordinated [ONO] ligands. Their reactivity will also be discussed in the third chapter. The synthesis and characterization of two novel bimetallic compounds of the form [ONO]M'[ONO]$_2$M (M' = Fe, Zn; M = Fe) will be presented in chapter 4. The final chapter will explore how the nature of the ligand backbone affects the redox activity of two homoleptic tris-iminosemiquinonate chromium(III) complexes.

1.5 References

[1] Jørgensen, C. K. *Coord. Chem. Rev.* **1966**, *1*, 164–178.

[2] Eisenberg, R.; Gray, H. B. *Inorg. Chem.* **2011**, *50*, 9741–9751.

[3] Kaim, W. *Inorg. Chem.* **2011**, *50*, 9752–9765.

[4] (a) Gorelsky, S. I.; Dodsworth, E. S.; Lever, A. B. P.; Vlček, A. A. *Coord. Chem. Rev.* **1998**, *174*, 469–494. (b) Gorelsky, S. I.; Lever, A. B. P.; Ebadi, M. *Coord. Chem. Rev.* **2002**, *230*, 97–105.

[5] Chirik, P. J. *Inorg. Chem.* **2011**, *50*, 9737–9740.

[6] Schrauzer, G. N.; Mayweg, V. *J. Am. Chem. Soc.* **1962**, *84*, 3221.

[7] (a) Gray, H. B.; Williams, R.; Bernal, I.; Billig, E. **1962**, *84*, 3596–3597. (b) Gray, H. B.; Billig, E. *J. Am. Chem. Soc*. **1963**, *85*, 2019–2020.

[8] Davison, A.; Edelstein, N.; Holm, R. H.; Maki, A. H. *Inorg. Chem.* **1963**, *2*, 1227–1232.

[9] (a) Shupack, S. I.; Billig, R. H. J.; Clark, R. W.; Gray, H. B. *J. Am. Chem. Soc.* **1964**, *86*, 4594–4602. (b) Stiefel, E. I.; Waters, J. H.; Billig, E.; Gray, H. B. *J. Am. Chem. Soc.* **1965**, *87*, 3016–3017.

[10] (a) Griffith, W. P. *Transit. Met. Chem.* **1993**, *18*, 250–256. (b) Balch, A. L. *J. Am. Chem. Soc.* **1973**, *95*, 2723–2724.

[11] (a) Pierpont, C. G. *Coord. Chem. Rev.* **2001**, *221*, 415–433. (b) Pierpont, C. G.; Buchanan, R. M. *Coord. Chem. Rev.* **1981**, *38*, 45-87.

[12] Caulton, K. G. *Eur. J. Inorg. Chem.* **2012**, *2012*, 435–443.

[13] (a) Herebian, D.; Wieghardt, K.; Neese, F. *J. Am. Chem. Soc.* **2003**, *125*, 10997–11005. (b) Ray, K.; Petrenko, T.; Wieghardt, K.; Neese, F. *Dalton Trans.* **2007**, 1552–1566. (c) Chaudhuri, P.; Verani, C. N.; Bill, E.; Bothe, E.; Weyhermüller, T.; Wieghardt, K. *J. Am. Chem. Soc.* **2001**, *123*, 2213–2223.

[14] Ward, M. D.; McCleverty, J. A. *J. Chem. Soc. Dalt. Trans.* **2002**, 275–288.

[15] (a) Munhá, R. F.; Zarkesh, R. A; Heyduk, A. F. *Dalton Trans.* **2013**, *42*, 3751–3766. (b) Heyduk, A. F.; Zarkesh, R. a; Nguyen, A. I. *Inorg. Chem.* **2011**, *50*, 9849–9863.

[16] (a) Blackmore, K. J.; Ziller, J. W.; Heyduk, A. F. *Inorg. Chem.* **2005**, *44*, 5559–5561. (b) Blackmore, K. J.; Sly, M. B.; Haneline, M. R.; Ziller, J. W.; Heyduk, A. F. *Inorg. Chem.* **2008**, *47*, 10522–10532.

[17] Haneline, M. R.; Heyduk, A. F. *J. Am. Chem. Soc.* **2006**, *128*, 8410–8411.

[18] Borgias, B. A.; Cooper, S. R.; Koh, Y. B.; Raymond, K. N. *Inorg. Chem.* **1984**, *23*, 1009–1016.

[19] Szigethy, G.; Heyduk, A. F. *Inorg. Chem.* **2011**, *50*, 125–135.

[20] Zarkesh, R. A; Ziller, J. W.; Heyduk, A. F. *Angew. Chem. Int. Ed. Engl.* **2008**, *47*, 4715–4718.

[21] (a) Nguyen, A. I.; Blackmore, K. J.; Carter, S. M.; Zarkesh, R. A.; Heyduk, A. F. *J. Am. Chem. Soc.* **2009**, *131*, 3307–3316. (b) Nguyen, A. I.; Zarkesh, R. a.; Lacy, D. C.; Thorson, M. K.; Heyduk, A. F. *Chem. Sci.* **2011**, *2*, 166–169.

[22] Shaffer, D. W.; Szigethy, G.; Ziller, J. W.; Heyduk, A. F. *Inorg. Chem.* **2013**, *52*, 2110–2118.

[23] (a) England, J.; Martinho, M.; Farquhar, E. R.; Frisch, J. R.; Bominaar, E. L.; Münck, E.; Que, Jr.,L. *Angew. Chem. Int. Ed.* **2009**, *48*, 3622–3626. (b) Zang, Y.; Dong, Y.; Que, Jr., L. *J. Am. Chem. Soc.* **1995**, *117*, 1169–1170 (c) Dong, Y.; Fujii, H.; Hendrich, M. P.; Leising, R. A.; Pan, G.; Randall, C. R.; Wilkinson, E. C.; Zang, Y.; Que, Jr., L.; Fox, B. G.; Kauffmann, K.; Münck, E. *J. Am. Chem. Soc.* **1995**, *117*, 2778–2792. (d) Hsu, H.-F.; Dong, Y.; Shu, L.; Young, Jr., V. G.; Que, Jr., L. *J. Am. Chem. Soc.* **1999**, *121*, 5230–5237. (e) Lacy, D. C.; Gupta, R.; Stone, K. L.; Greaves, J.; Ziller, J. W.; Hendrich, M. P.; Borovik, A. S. *J. Am. Chem. Soc.* **2010**, *132*, 12188–12190. (f) de Oliveira, F. T.; Chanda, A.; Banerjee, D.; Shan, X.; Mondal, S.; Que, L. Jr.; Bominaar, E. L.; Münck, E.; Collins, T. J. *Science* **2007**, *315*, 835–838. (g) Grapperhaus, C. A.; Mienert, B.; Bill, E.; Weyhermüller; Wieghardt, K. *Inorg. Chem.* **2000**, *39*, 5306–5317. (h) MacBeth, C. E.; Golombek, A. P.; Young Jr., V. G.; Yang, C.; Kuczera, K.; Hendrich, M. P.; Borovik, A. S. *Science* **2000**, *289*, 938–940. (i) MacBeth, C.; Gupta, R.; Mitchell-Koch, K. R.; Young Jr., V. G.; Lushington, G. H.; Thompson, W. H.; Hendrich, M. P.; Borovik, A. S. *J. Am. Chem. Soc.* **2004**, *126*, 2556–2567. (j) Dey, A.; Ghosh, A. *J. Am. Chem. Soc.* **2002**, *124*, 3206–3207.

[24] Berry, J. F.; Bill, E.; Bothe, E.; George, S. D.; Mienert, B.; Neese, F.; Wieghardt, K. *Science* **2006**, *312*, 1937–1941.

[25] (a) Mbughuni, M. M.; Chakrabarti, M.; Hayden, J. A.; Bominaar, E. L.; Hendrich, M. P.; Münck, E.; Lipscomb, J. D. *PNAS*, **2010**, *107*(39), 16788–1693. (b) Lipscomb, J. D. *Current Opinion in Structural Biology*, *18*, 644–649.

[26] (a) Lee, Y.; Mankad, N. P.; Peters, J. C. *Nat. Chem.* **2010**, *2* (7), 2558–2567. (b) Eckert, N. A.; Stoian, S.; Smith, J. M.; Bominaar, E. L.; Münck, E.; Holland, P. L. *J. Am. Chem. Soc.* **2005**, *127*, 9344–9345. (c) Smith, J. M.; Sadique, A. R.; Cundari, T. R.; Rodgers, K. R.; Lukat-Rodgers, G.; Lachicotte, R. J.; Flaschenriem, C. J.; Vela, J.; Holland, P. L. *J. Am. Chem. Soc.* **2006**, *128*, 756–769. (d) Brown, S. D.; Betley, T. A.; Peters, J. C. *J. Am. Chem. Soc.* **2003**, *125*, 322–323.

[27] Kaim, W.; Schwederski, B. *Coord. Chem. Rev.* **2010**, *254*, 1580–1588.

[28] (a) Cox, D. D.; Que, Jr., L. *J. Am. Chem. Soc.* **1988**, *110*, 8085–8092. (b) Bruijnincx, P. C. A.; Lutz, M.; Spek, A. L.; Hagen, W. R.; Weckhuysen, B. M.; van Koten, G.; Gebbink, R. J. M. K. *J. Am. Chem. Soc.* **2007**, *129*, 2275–2286. (c) Bittner, M. M.; Lindeman, S. V.; Fiedler, A. T. *J. Am. Chem. Soc.* **2012**, *134*, 5460–5463.

[29] (a) Plietker, B., Ed. *Iron Catalysis in Organic Chemistry*; Wiley-VCH: Weinheim, 2008. (b) Plietker, B., Ed. *Iron Catalysis*; Springer-Verlag: Berlin Heidelberg, 2011.

[30] (a) Sherry, B. D. and Fürstner, A. *Acc. Chem. Res.* **2008**, *41*(11), 1500–1511. (b) Czaplik, W. M.; Mayer, M.; Cvengroš; Jacobi von Wangelin, A. *ChemSusChem* **2009**, *2*, 396–417. (c) Fürstner, A.; Leitner, A.; Méndez, M.; Krause, H. *J. Am. Chem. Soc.* **2002**, *124*, 13856–13863.

[31] (a) Plietker, B., Ed. *Iron Catalysis in Organic Chemistry*; Wiley-VCH: Weinheim, 2008. (b) Plietker, B., Ed. *Iron Catalysis*; Springer-Verlag: Berlin Heidelberg, 2011.

[32] (a) Sherry, B. D. and Fürstner, A. *Acc. Chem. Res.* **2008**, *41*(11), 1500–1511. (b) Czaplik, W. M.; Mayer, M.; Cvengroš; Jacobi von Wangelin, A. *ChemSusChem* **2009**, *2*, 396–417. (c) Fürstner, A.; Leitner, A.; Méndez, M.; Krause, H. *J. Am. Chem. Soc.* **2002**, *124*, 13856–13863.

[33] (a) Tamura, M. and Kochi, J. *J. Am. Chem. Soc.* **1971**, *93*, 1487–1489. (b) Smith, R. S. and Kochi, J. K. *J. Org. Chem.*, **1976**, *41*, 502–509.

[34] Chirik, P. J.; Wieghardt, K. *Science* **2010**, *327*, 794–795.

[35] Bouwkamp, M. W.; Bowman, A. C.; Lobkovsky, E.; Chirik, P. J. *J. Am. Chem. Soc.* **2006**, *128*, 13340–13341.

[36] Bart, S. C.; Lobkovsky, E.; Chirik, P. J. *J. Am. Chem. Soc.* **2004**, *126*, 13794–13807.

[37] (a) Bart, S. C.; Lobkovsky, E.; Bill, E.; Chirik, P. J. *J. Am. Chem. Soc.* **2006**, *128*, 5302–5303. (b) Bart, S. C.; Chłopek, K.; Bill, E.; Bouwkamp, M. W.; Lobkovsky, E.; Neese, F.; Wieghardt, K.; Chirik, P. J. *J. Am. Chem. Soc.* **2006**, *128*, 13901–13912. (c) Bart, S. C.; Lobkovsky, E.; Bill, E.; Wieghardt, K.; Chirik, P. J. *Inorg. Chem.* **2007**, *46*, 7055–7063.

[38] Trovitch, R. J.; Lobkovsky, E.; Chirik, P. J. *Inorg. Chem.* **2006**, *45*, 7252–7260.

[39] (a) Sylvester, K. T.; Chirik, P. J. *J. Am. Chem. Soc.* **2009**, *131*, 8772–8774. (b) Russell, S. K.; Lobkovsky, E.; Chirik, P. J. *J. Am. Chem. Soc.* **2011**, *133*, 8858–8861.

[40] (a) Buchanan, R. M.; Kessel, S. L.; Downs, H. H.; Pierpont, C. G.; Hendrickson, D. N. *J. Am. Chem. Soc.* **1978**, *100*, 7894–7900. (b) Attia, S.; Conklin, B. J.; Lange, C. W.; Pierpont, C. G. *Inorg. Chem.* **1996**, *35*, 1033–1038. (c) Boone, S. R.; Purser, G. H.; Chang, H.; Lowery, M. D.; Hendrickson, D. N.; Pierpont, C. G. *J. Am. Chem. Soc.* **1989**, *111*, 2292–2299.

[41] Pierpont, C. G. *Inorg. Chem.* **2011**, *50*, 9766–9772.

[42] (a) Girgis, A. Y.; Balch, A. L. *Inorg. Chem.* **1975**, *14*, 2724–2727. (b) Simpson, C. L.; Boone, S. R.; Pierpont, C. G. *Inorg. Chem.* **1989**, *28*, 4379–4385.

Chapter 2

Synthesis and Characterization of Iron Complexes Coordinated to the Redox-Active [ONO] Ligand

Portions of this work have been reported previously:
Wong, J. L.; Sánchez, R. H.; Logan, J. G.; Zarkesh, R. A.; Ziller, J. W.; Heyduk, A. F. *Chem. Sci.* **2013**, *4*, 1906–1910.

2.1 Introduction

Research in redox-active iron complexes has garnered increasing attention in recent years due to their potential applications catalysis,[1, 2, 3] small-molecule activation reactivity,[4, 5, 6, 7] and other multi-electron transformations.[8, 9, 10] Although the redox activity of many iron complexes is primarily metal-centered due to iron's ability to achieve a large range of oxidation states, redox-active ligands can also provide reducing/oxidizing equivalents.

Chirik and coworkers developed a family of five-coordinate iron complexes derived from [PDI]FeBr$_2$ ([PDI] = pyridine diimine) that exhibit ligand-enabled multi-electron reactivity.[11] As shown in Scheme 2.1, reduction of this complex under a nitrogen atmosphere produces an iron bis(dinitrogen) complex, [PDI]Fe(N$_2$)$_2$.[11] While the resulting complex is formally an iron(0) compound, spectroscopic and magnetic studies indicate that it is better described as a high-spin iron(II) complex with a doubly-reduced [PDI]$^{2-}$ ligand. The redox flexibility afforded by the [PDI]Fe platform has enabled the development of catalysts for the hydrogenation and hydrosilation of organic substrates,[9, 10] cycloaddition of dienes,[12a–b] and cyclization of 1,6-enynes and diynes.[12c–d]

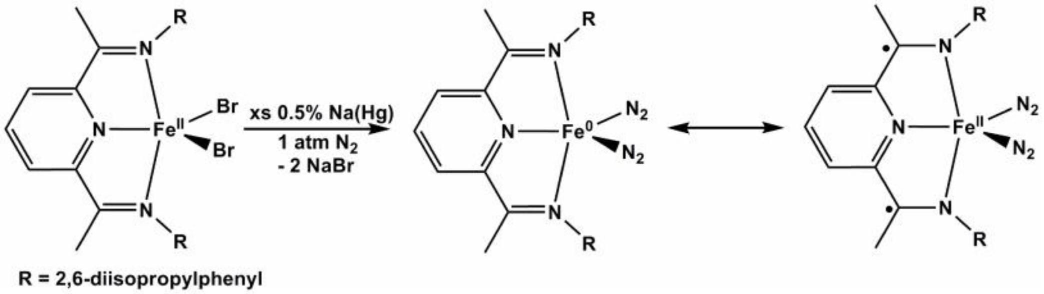

Scheme 2.1. Reduction of [PDI]FeBr$_2$ to form resulting iron bis(dinitrogen) complex. Resonance is shown here to highlight the redox non-innocent nature of the compound.

Another well-studied redox-active pincer-type ligand is the [ONO] ligand ([ONO^{cat}]H$_3$ = bis(3,5-di-*tert*-butyl-2-phenol)amine).[13, 14] An attractive feature of the [ONO] platform is that it can be isolated in three oxidation states, providing a diverse reagent palette for the preparation of new coordination complexes.[15,16,17,18] As shown in Scheme 2.2, deprotonation of neutral $[ONO^{cat}]H_3$ results in a redox-active ligand moiety where the trianionic catecholate ($[ONO^{cat}]^{3-}$), dianionic semiquinonate ($[ONO^{sq}]^{2-}$), and monoanionic quinonate ($[ONO^{q}]^{1-}$) forms are accessible. The potassium salt of $[ONO^{q}]^{1-}$ can be synthesized in high yields by first deprotonating $[ONO^{cat}]H_3$ with three equivalents of KH followed by a two-electron oxidation with $PhI(OAc)_2$.[17] Synthesis of $K_2[ONO^{sq}]$ can be achieved via comproportionation of $K_3[ONO^{cat}]$ and $K[ONO^{q}]$. The $[ONHO]^{2-}$ ligand can also be generated via selective deprotonation of the phenols in $[ONO^{cat}]H_3$, although the protonation of the central nitrogen disrupts the conjugation of the ligand π system, inhibiting the redox-activity.

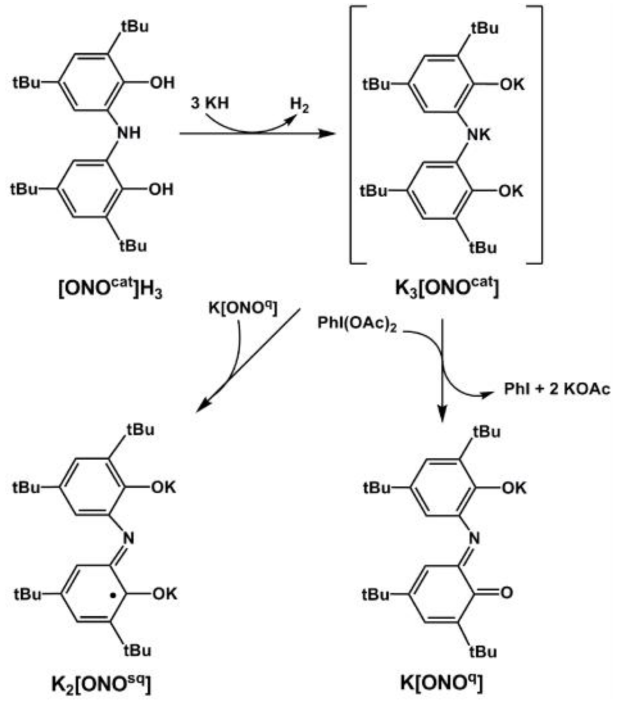

Scheme 2.2. Synthetic routes towards accessing the various oxidation states of the [ONO] ligand.

Towards our goal of developing a new platform for multi-electron reactivity, iron complexes of the [ONO] moiety have been targeted for synthesis.[18] The homoleptic complex $Fe^{III}[ONO]_2$ was the first reported example of an iron complex supported by the [ONO] ligand.[13] Despite its rich redox properties, the saturated coordination environment leaves the pseudo-octahedral complex unsuitable for further reactivity studies. In order to generate iron complexes capable of effecting inner-sphere reactivity, a series of iron complexes coordinated to a single [ONO] ligand have been prepared and characterized.

2.2 Results

2.2.1 Synthesis and Characterization of (BDI-mes)$FeCl_2$

The iron(II) coordination complex, (BDI-mes)$FeCl_2$ (**1**), was prepared according to modified published procedures for use as a synthon in the preparation of new iron complexes containing the [ONO] ligand platform.[19] The *N*,*N'*-bis(2,4,6-trimethylphenyl)-2,3-butanediimine (BDI-mes) directly reacted with iron(II) chloride to generate **1** in 81% yield. X-ray quality red crystals of **1** were grown from a saturated chloroform solution of the complex at −35 °C (Figure 2.1). Table 2.1 shows a list of selected bond lengths and angles for **1**. The Cl(1)–Fe(1)–Cl(2) and N(1)–Fe(1)–N(2) bond angles of 115.52(2)° and 76.23(7)°, respectively, establish that **1** possesses a distorted tetrahedral geometry. The BDI-mes ligand can behave as a non-innocent ligand and adopt one of the following forms: ~-diimine (neutral), iminate ® radical (1−), and ~-diamide (2−). The oxidation state of the ligand is characterized by the C−N and C−C bond lengths.[20] The N(2)–C(1) and C(1)–C(2) bond lengths of 1.279(3) Å and 1.518(3) Å, respectively, are consistent with the C–N double and C–C single bonds of the BDI-mes ligand.[21] Hence, the BDI-mes ligand is in the neutral L_2-type form and the oxidation state of the iron center is +2.

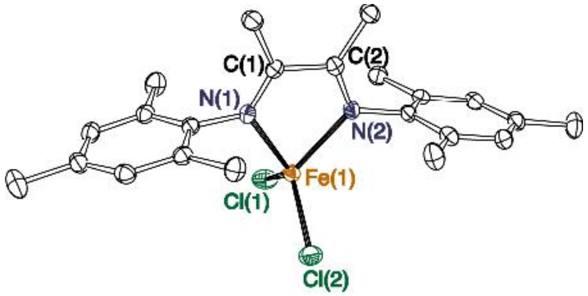

Figure 2.1. ORTEP diagram of the crystal structure of **1**. Thermal ellipsoids are drawn at 50% probability. Hydrogens have been removed for clarity.

Table 2.1. Selected bond lengths (Å) and angles (°) of **1**.

Bond	Length	Bond	Angle
N(2)–C(1)	1.279(3)	Cl(1)–Fe–Cl(2)	115.52(2)
C(1)–C(2)	1.518(3)	N(1)–Fe–N(2)	76.23(7)

2.2.2. Synthesis and Characterization of [ONHO]Fe(BDI-mes)

Complex **2** proved to be a useful starting material for coordination of the doubly-deprotonated [ONHO]$^{2-}$ ligand to iron. As shown in Scheme 2.3, the [ONO$^{\mathrm{cat}}$]H$_3$ was first deprotonated with two equivalents of KH. To the *in-situ* generated K$_2$[ONHO], **1** was added to yield dark green crystals of [ONHO]Fe(BDI-mes) (**2**) by salt metathesis in 69% yield. Single crystals of **2** suitable for X-ray crystallography were grown from saturated pentane solutions at ambient temperature.

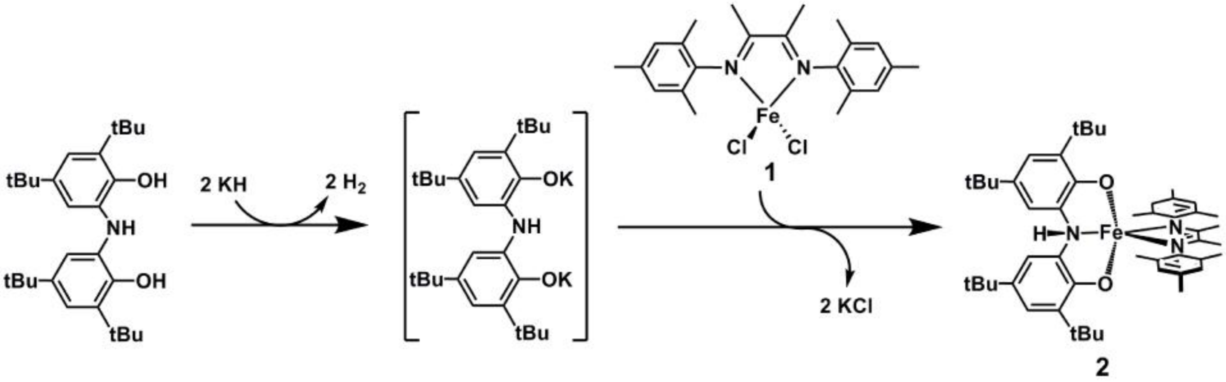

Scheme 2.3. Synthesis of **2** from metathesis of **1** and K$_2$[ONHO].

Analysis of the structural metrics of **2**, obtained by X-ray crystallography, allowed for assignment of possible oxidation states of the ligands and metal centers. The solid-state structure of **2** is shown as an ORTEP diagram in Figure 2.2 and selected bond metrical data for the primary coordination sphere at iron are given in Table 2.2. The geometric parameter ² = (– ~) / 60 (² = 1 for perfectly trigonal bipyramid; 0 for perfectly square pyramid) was used to describe the coordination geometry at the iron center.[22] Given that = ∠N(1)–Fe(1)–N(2) and ~ = ∠O(1)–Fe(1)–O(2), the ² value of 0.75 indicates that **2** is best described as having a distorted trigonal-bipyramidal geometry. The C(1)–N(1)–C(15), H(1)–N(1)–Fe(1) and C(15)–N(1)–Fe(1) bond angles of 117.42(14)°, 113(1)°, and 102.29(11)°, respectively, are consistent with a pseudo-tetrahedral geometry at the protonated N(1) atom. For the BDI-mes portion of **2**, the N(2)–C(29) bond length of 1.296(2) Å indicates a C–N double bond and the C(29)–C(30) bond length of 1.496(3) Å indicates a C–C single bond. The C(15)–N(1) and C(2)–O(1) bond lengths of 1.451(2) Å and 1.343(2) Å, respectively, of the tridentate ligand are consistent with corresponding C(sp^2)–N(sp^3) and C(aryl)–O single bonds.[21] These bond lengths indicate that the BDI-mes remains in its neutral ~-diimine form while the [ONHO] ligand has two anionic oxygen donors.

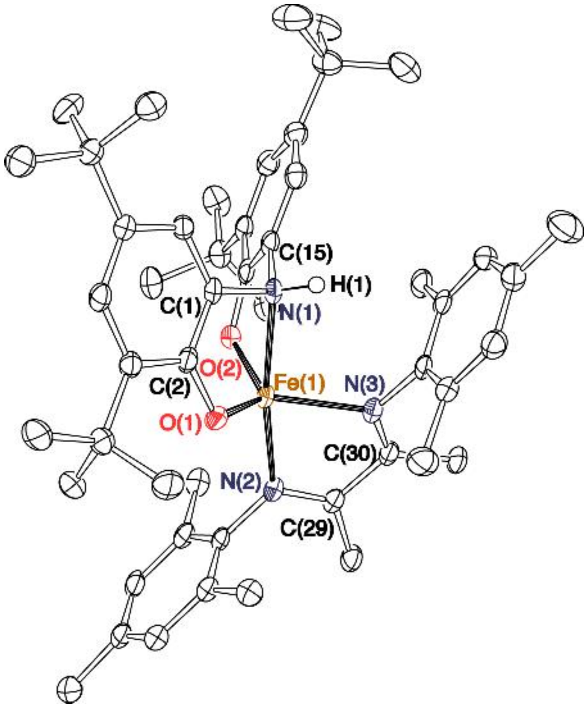

Figure 2.2. ORTEP diagram of the crystal structure of **2**. Thermal ellipsoids are drawn at 50% probability. With the exception of H(1), all hydrogens have been removed for simplicity.

Table 2.2. Selected bond lengths (Å) and angles (°) of **2**.

Bond	Length	Bond	Angle
C(15)–N(1)	1.451(2)	C(1)–N(1)–C(15)	117.42(14)
C(2)–O(1)	1.343(2)	C(15)–N(1)–Fe(1)	105.63(11)
N(2)–C(29)	1.296(2)	C(1)–N(1)–Fe(1)	102.29(11)
C(29)–C(30)	1.496(3)	N(1)–Fe(1)–N(2)	170.76(6)
Fe(1)–N(1)	2.216(2)	N(1)–Fe(1)–N(3)	95.86(6)
Fe(1)–N(2)	2.139(2)	O(1)–Fe(1)–O(2)	125.96(5)
Fe(1)–N(3)	2.095(2)		
Fe(1)–O(1)	1.943(1)		
Fe(1)–O(2)	1.985(1)		

Spectroscopic measurements are consistent with the crystallographically-determined +2 oxidation state of the iron center. A sharp infrared stretch at 3282 cm^{-1} coupled with the tetrahedral geometry at N(1) are evidence that the central nitrogen on the [ONHO] ligand remains protonated and behaves as an L-type ligand. The Mössbauer spectrum of **2** at 80 K, shown in Figure 2.3, displays an isomer shift (δ) of 0.93 mm/s, which is typical of high-spin Fe(II) complexes.[23]

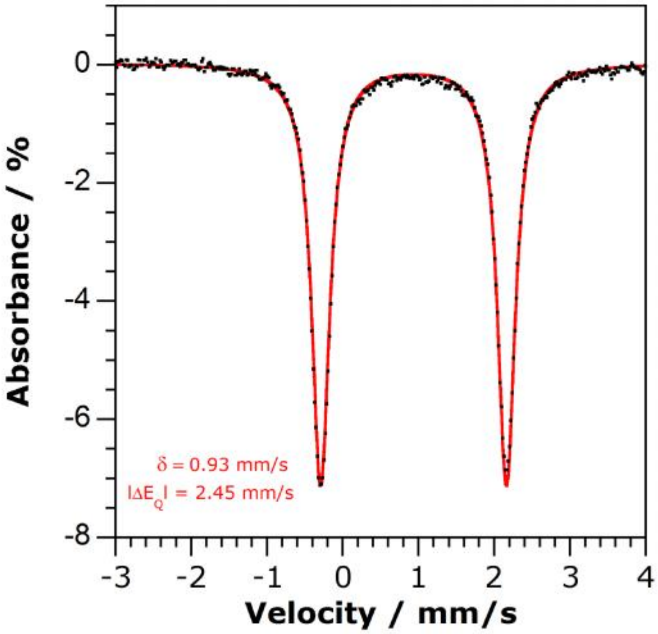

Figure 2.3. Mössbauer spectrum of [ONHO]Fe(BDI-mes) (**2**) collected at 80 K.

Towards our goal of synthesizing new iron complexes supported by a redox-active [ONO] moiety, attempts to deprotonate the [ONHO] ligand of **2** followed by oxidation of the complex by one electron were pursued. As described in Scheme 2.4, to promote π-conjugation in the ligand backbone, **2** was treated with a combination of bases and oxidants for removal of a proton and an electron. However, these reactivity pathways led to extrusion of the BDI-mes ligand, resulting in disproportionation of the product. The challenges posed by the [ONHO]Fe platform motivated us to develop new synthetic routes for generating redox-active iron complexes. When $K_2[ONO^{sq}]$ reacted with (BDI-mes)$FeCl_2$ (**1**), free diimine ligand was also observed and no new iron complex was isolated. Regardless of the reagent stoichiometry, when $K[ONO^{q}]$ reacted with iron(II) salts, only $Fe^{III}[ONO]_2$ could be isolated. These results indicate that [ONO]Fe complexes could not be accessed through iron(II) starting materials.

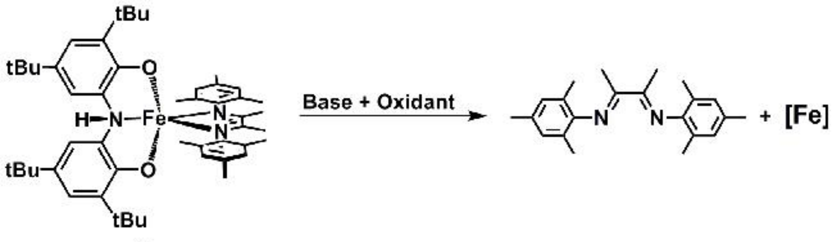

2

Base (equiv.)	Oxidant (equiv.)
Et_3N (1)	$PhI(OAc)_2$ (0.5)
Et_3N (1)	$PhICl_2$ (0.5)
Et_3N (1)	$AgPF_6$ (1)
Et_3N (1)	$FcPF_6$ (1)
n-Butylithium (1)	$FcPF_6$ (1)

Scheme 2.4. Deprotonation and oxidation of complex **2** using various bases and oxidants. All reactions were carried out at ambient temperature using either THF, pentane, or diethyl ether solvents.

2.2.3. Synthesis and Characterization of $[ONO^q]FeX_2$ Complexes

By employing iron(III) salts as starting materials, a new class of $[ONO^q]Fe^{III}X_2$ complexes have been prepared and characterized. As shown in Scheme 2.5, the oxidized ligand synthon, $K[ONO^q]$, provided a direct route for the synthesis of iron complexes of the $[ONO^q]$ platform.[18]

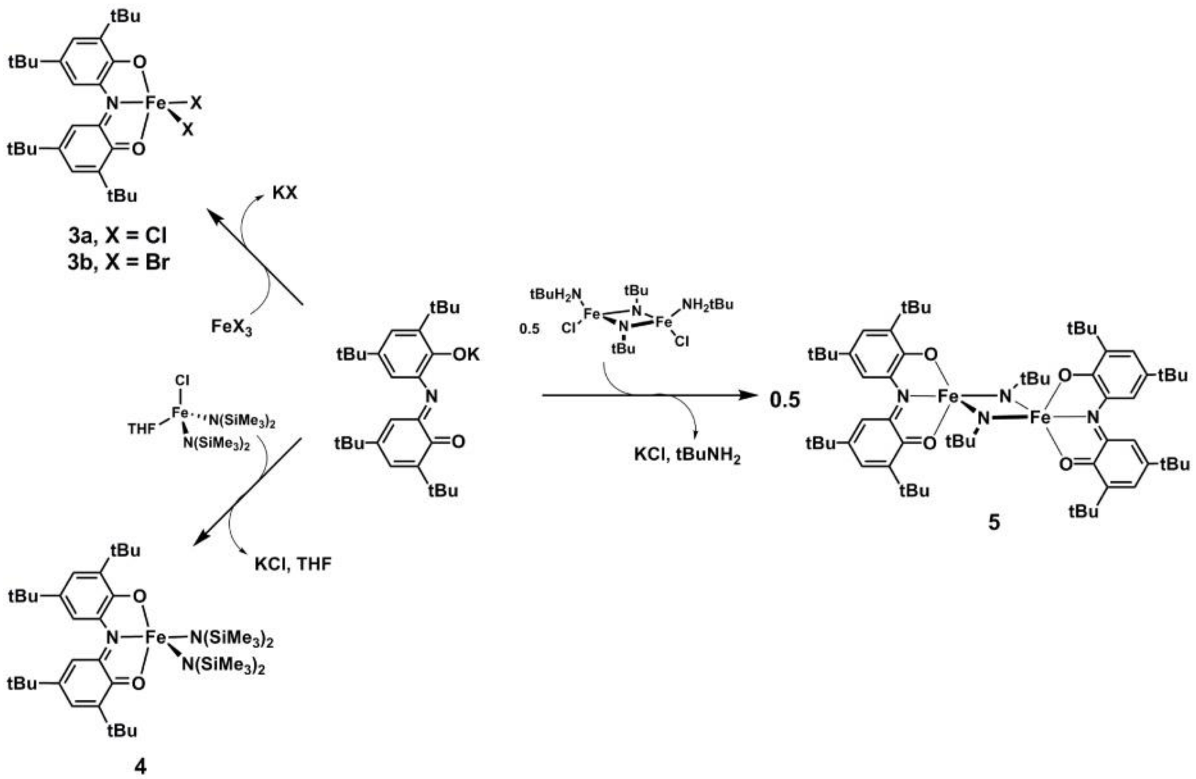

Scheme 2.5. Synthesis of [ONO^q]FeX$_2$ complexes.

Coordination of the [ONO^q]$^{1-}$ ligand to an iron dihalide was carried out via salt metathesis reaction of K[ONO^q] with FeX$_3$. Treatment of FeCl$_3$ in toluene or FeBr$_3$ in diethyl ether with one equivalent of K[ONO^q] resulted in the elimination of potassium halide salts and the concomitant formation of new [ONO^q]FeX$_2$ (X = Cl, (**3a**); Br (**3b**)) in 71% and 72% yields, respectively. Dark red crystals suitable for X-ray crystallography of **3a** were isolated at –35 °C via diffusion of pentane into toluene solutions containing **3a**. Dark red crystals of **3b** were obtained at –35 °C by diffusing pentane into diethyl ether solutions of **3b**.

Intraligand bond distances within the [ONO] ligand of **3a** and **3b** are used as diagnostic tools for determining the ligand and consequently, the metal oxidation states. Figure 2.4 shows an ORTEP diagram for the crystal structure of **3a**. Selected bond measurements of **3a** and **3b** are listed in Table 2.3. Electron delocalization within the molecules influences the C(2)–O(1) and C(16)–O(2) bond lengths to lie between 1.36 Å and 1.21 Å, which are the corresponding

C(aryl)–O single and C(sp^2)–O double bond lengths.[21] The bond lengths of the C(17)–C(18) and C(19)–C(20) bonds of the [ONO] ligand six-membered ring are shorter than those of the other four ring C–C bonds. The two short and four long C–C bonds of the [ONO] ligand backbone are consistent with the bond metrical patterns observed in M[ONO^q]$_2$ (M = Ni, Zn, Pb)[13, 14] and [ONO^q]M (M = Ta,[15] Al[16]) complexes. Thus, the [ONO] ligands of **3a** and **3b** are in the fully-oxidized [ONO^q]$^{1-}$ form, suggesting that both iron dihalide complexes have iron(III) centers. Given that ~ = ∠N(1)–Fe(1)–X(1) and = ∠O(1)–Fe(1)–O(2), the ^{2} values of 0.18 for **3a** and 0.12 for **3b** suggest that both complexes adopt distorted square pyramidal geometries.[22]

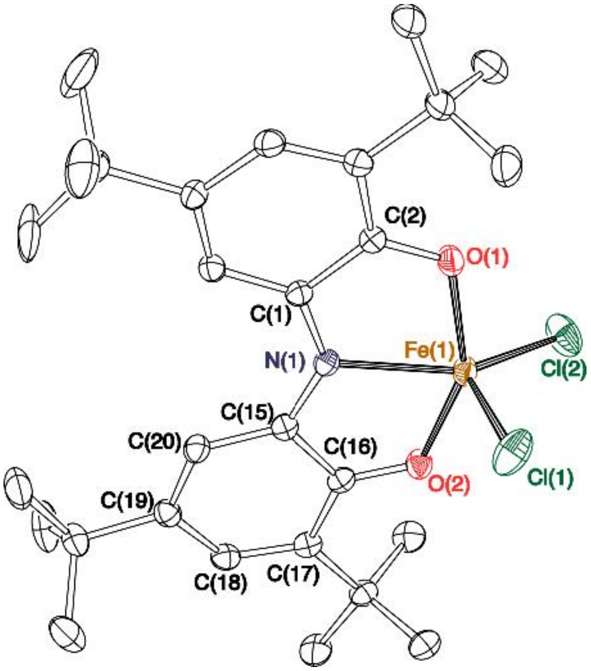

Figure 2.4. Crystal structure of **3a.** The hydrogens and *tert*-butyl groups are removed for simplicity. Thermal ellipsoids drawn at 50% probability.

Table 2.3. Selected bond lengths (Å) and angles (°) of **3a** and **3b**.

Bond lengths/angles	**3a** (X = Cl)	**3b** (X = Br)
C(16)–O(2)	1.268(2)	1.287(2)
C(2)–O(1)	1.296(2)	1.279(2)
C(1)–N(1)	1.359(2)	1.336(3)

C(15)–N(1)	1.332(2)	1.349(3)
C(15)–C(16)	1.474(2)	1.445(3)
C(16)–C(17)	1.443(2)	1.434(3)
C(17)–C(18)	1.360(3)	1.371(3)
C(18)–C(19)	1.444(2)	1.431(3)
C(19)–C(20)	1.357(3)	1.358(3)
C(15)–C(20)	1.427(3)	1.422(3)
Fe(1)–O(1)	1.943(1)	1.963(1)
Fe(1)–O(2)	1.997(1)	1.972(1)
Fe(1)–X(1)	2.2056(6)	2.3609(4)
Fe(1)–X(2)	2.2054(6)	2.3570(4)
Fe(1)–N(1)	2.157(1)	2.162(2)
O(1)–Fe(1)–O(2)	151.23(6)	149.94(6)
O(1)–Fe(1)–N(1)	77.01(5)	75.77(6)
N(1)–Fe(1)–X(1)	140.69(4)	142.88(5)
N(1)–Fe(1)–X(2)	104.87(4)	107.77(5)

Both iron dihalide complexes have been characterized using various analytical techniques in order to investigate the oxidation states and spin states of the metal centers. Mössbauer spectroscopy reveals that **3a** is a high-spin Fe(III) compound with δ = 0.3 mm/s and ΔE_Q = 0.61 mm/s at 80 K (Figure 2.5).[23] Small amounts of high spin Fe(II) impurities (δ = 1.04 mm/s, ΔE_Q = 2.33 mm/s) are also present in the spectrum. The EPR spectrum of **3a** displays a rhombic signal with *g* values of 9.70, 4.32, and 2.00 (Figure 2.6). These resonances are consistent with a high-spin iron(III) species having E/D = 0.33 rhombicity.[24] Mössbauer data of **3b** could not be obtained because the bromide significantly attenuates the gamma rays. Nonetheless, as shown in Figure 2.6, the EPR spectrum of **3b** is also consistent with the metal complex possessing a high-spin iron(III) center.

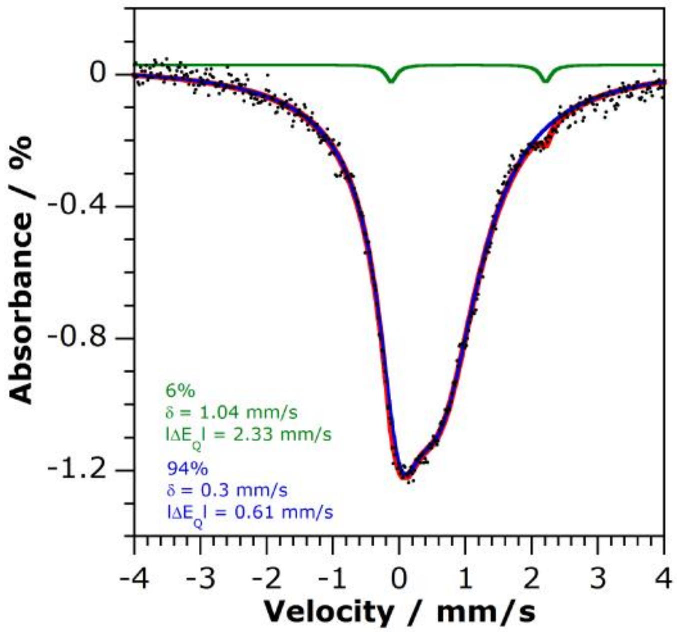

Figure 2.5. Mössbauer spectrum of [ONO^q]FeCl$_2$ (**3a**) collected at 80 K. The iron(III) species major component (94%) is shown in blue while the iron(II) species minor component (6%) is shown in green. The overall data fit is shown in red.

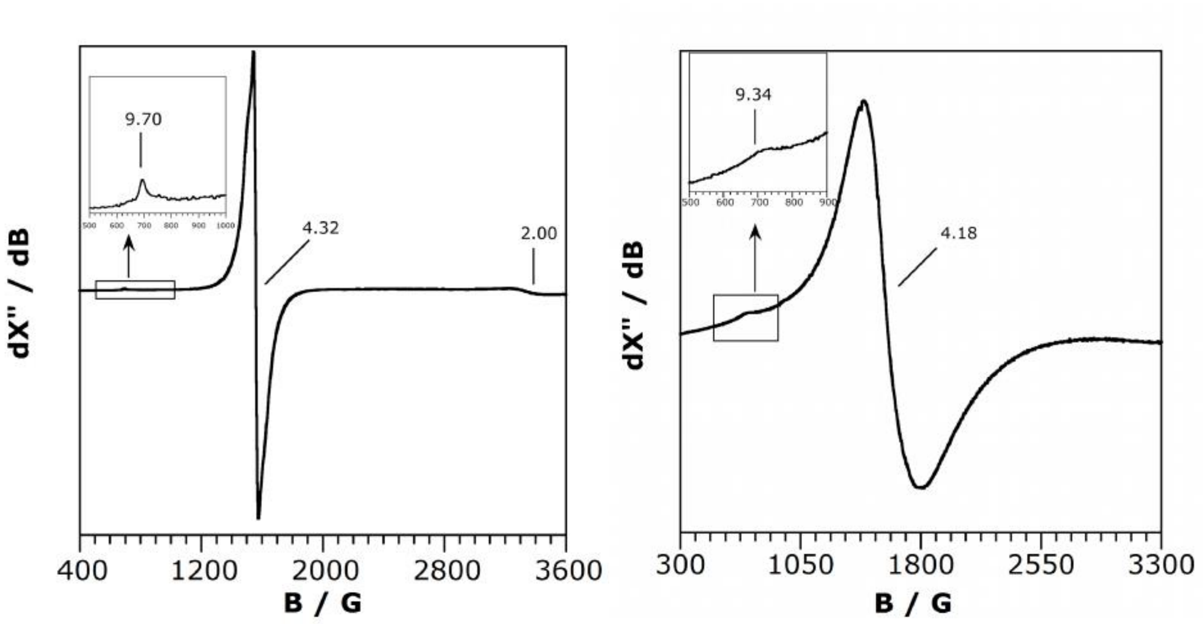

Figure 2.6. X-band EPR spectra of [ONO^q]FeCl$_2$ (**3a**; *left*) and [ONO^q]FeBr$_2$ (**3b**; *right*). Experimental conditions: $B_1 \perp B_0$; solvent, toluene; temperature, 77 K.

Metallation of the $[\mathrm{ONO^q}]^{1-}$ to generate mononuclear iron amide and dinuclear iron imide complexes was achieved by reacting $\mathrm{K[ONO^q]}$ with the $\mathrm{FeCl(THF)[N(SiMe_3)_2]_2}$ and $\{(t\mathrm{BuNH_2})\mathrm{FeCl}(\mu\text{-N}t\mathrm{Bu})\}_2$ synthons developed by Lee and coworkers (Scheme 2.5).[25] Salt metathesis reaction of $\mathrm{K[ONO^q]}$ and $\mathrm{FeCl(THF)[N(SiMe_3)_2]_2}$ in toluene led to precipitation of KCl accompanied by formation of $\mathrm{[ONO^q]Fe[N(SiMe_3)_2]_2}$ (**4**) in 65% yield. Dark brown crystals of **4** suitable for X-ray diffraction were obtained by the diffusion of acetonitrile into toluene solutions of the iron complex at –35 °C. Treatment of $\{(t\mathrm{BuNH_2})\mathrm{FeCl}(\mu\text{-N}t\mathrm{Bu})\}_2$ in toluene with two equivalents of $\mathrm{K[ONO^q]}$ resulted in elimination of KCl to produce $\{\mathrm{[ONO^q]Fe}(\mu\text{-N}t\mathrm{Bu})\}_2$ (**5**) as a dark green product in 60% yield. Crystals of **5** were obtained via the diffusion of acetonitrile into THF solutions of the diiron compound at room temperature.

X-ray diffraction data for **4** help determine the coordination geometry of the metal center as well as the metal and ligand oxidation states. The crystal structure of **4** is depicted as an ORTEP diagram in Figure 2.7 and a list of selected bond measurements is shown in Table 2.4. Provided that ~ = ∠N(1)–Fe(1)–N(2) and = ∠O(1)–Fe(1)–O(2), ² = 0.13 for complex **4**, an indication that the geometry at the iron center is best described as square pyramidal.[22] The C–O bond lengths of 1.28 Å lie between 1.36 Å and 1.21 Å, which are the corresponding C(aryl)–O single and $\mathrm{C(sp^2)}$–O double bond lengths. In addition, localization of double bond character within the [ONO] ligand backbone is also observed, as evidenced by the two short C(16)–C(17) and C(18)–C(19) bond lengths in comparison to the four long C–C bonds. These bond metrical patterns are consistent with what has been observed in other metal complexes coordinated to the $[\mathrm{ONO^q}]^{1-}$ ligand.[13, 14, 15, 16]

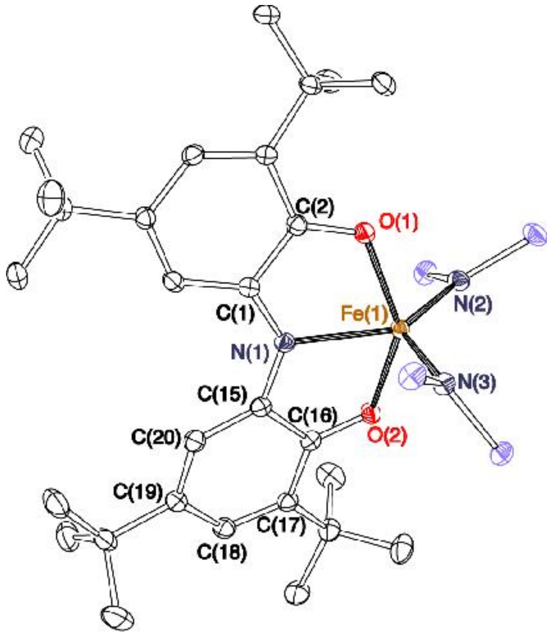

Figure 2.7. Crystal structure of **4**. The hydrogens and silicon-bound methyl groups are removed for simplicity. Thermal ellipsoids are drawn at 50% probability.

Table 2.4. Selected bond lengths (Å) and angles (°) of **4**.

Bond	Lengths	Bond	Angles
C(15)–O(2)	1.277(2)	O(1)–Fe(1)–O(2)	143.46(4)
C(1)–O(1)	1.275(2)	O(1)–Fe(1)–N(1)	74.38(4)
C(15)–N(1)	1.342(2)	N(1)–Fe(1)–N(2)	135.50(5)
C(6)–N(1)	1.345(2)	N(1)–Fe(1)–N(3)	104.04(5)
C(15) –C(16)	1.454(2)		
C(16) –C(17)	1.366(2)		
C(17) –C(18)	1.433(3)		
C(18) –C(19)	1.355(2)		
C(19) –C(20)	1.429(2)		
C(15) –C(20)	1.454(2)		
Fe(1)–O(1)	2.048(1)		
Fe(1)–O(2)	2.093(1)		
Fe(1)–N(1)	2.188(1)		
Fe(1)–N(2)	1.933(1)		
Fe(1)–N(3)	1.940(1)		

The coordinated $[\mathrm{ONO^q}]^{1-}$ and bis(trimethylsilyl)amide ligands are evidence that the oxidation state of iron in **4** is +3, a contention that is further supported by EPR spectroscopy. As shown in Figure 2.8, the EPR spectrum of **4** collected at 77 K shows an axial signal with *g* values of 5.37 and 2.00. These resonances are in agreement with **4** being an iron(III), $S = \frac{5}{2}$ complex.[24]

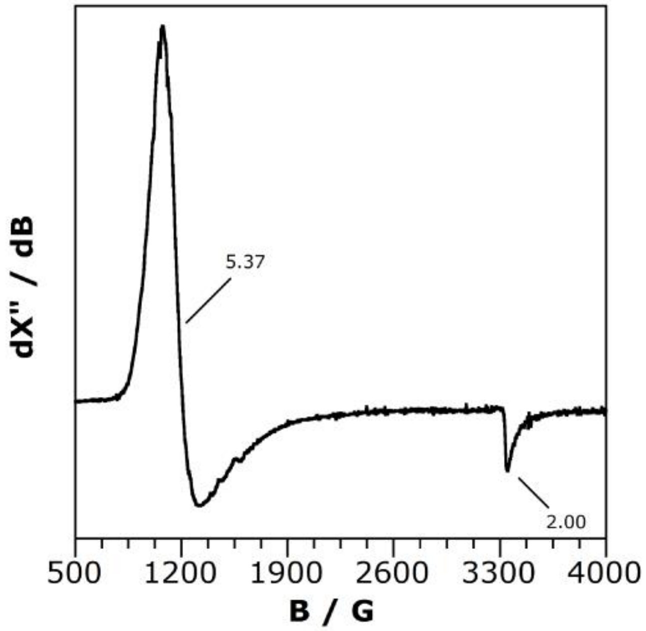

Figure 2.8. X-band EPR spectrum of $[\mathrm{ONO^q}]\mathrm{Fe[N(SiMe_3)_2]_2}$ (**4**). Experimental conditions: $B_1 \perp B_0$; solvent, toluene; temperature, 77 K.

The solid-state structure of $\{[\mathrm{ONO^q}]\mathrm{Fe}$(«-N*t*Bu)$\}_2$ (**5**) provides an overall description of the physical and electronic characteristics of the dimer (Figure 2.9). As listed in Table 2.5, the O(1)–Fe(1)–O(2) angle of 128.06(7)° ( ) and N(1)–Fe(1)–N(2) angle of 166.86(8)° (~) results in a ² value of 0.65, an indication that the geometry at each iron center lies in between square pyramid and trigonal bipyramid.[22] The asymmetric unit of this diiron complex consists of half the dimer, revealing the highly symmetric nature of **5**. The carbon–carbon bond measurements of the six-membered rings of the [ONO] backbone are also consistent with the bond metrics expected for the $[\mathrm{ONO^q}]^{1-}$ ligand.[13, 14, 15, 16] The average iron–imide bond lengths of 1.80 Å indicates that the imido ligands are coordinated almost equidistant from each iron center. In addition, the Fe(1)–N(2)–Fe(1A) and N(2)–Fe(1)–N(2A) bond angles of 89.20(8)° and 90.80(8)°, respectively, indicate that the shape of the diiron core is a rhomboid. The Fe(1)–Fe(1A) distance of 2.5344(5) Å is longer than the length of an Fe–Fe single bond of 2.48 Å,[26] but similar to other diiron compounds with bridging imido ligands.[25b] Coordination of two bridging imidos and one $[\mathrm{ONO}^{q}]^{1-}$ at each metal provides evidence that **5** possesses two iron(III) centers.

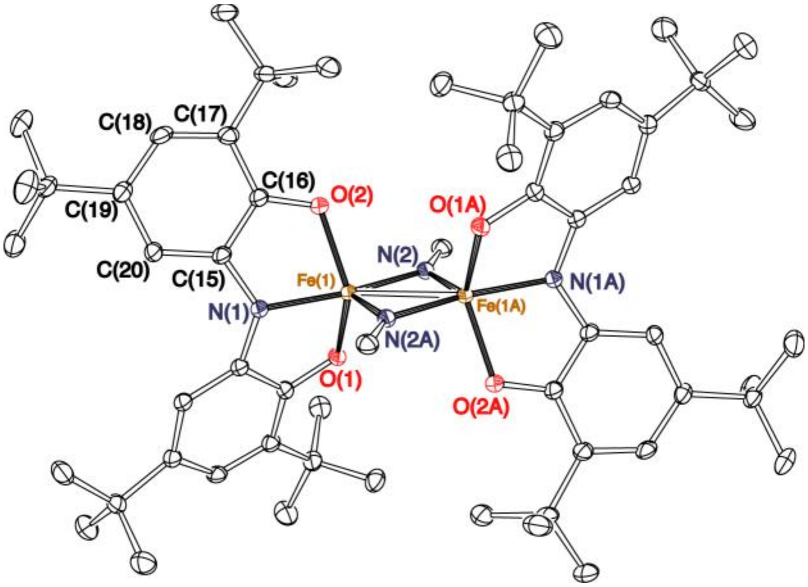

Figure 2.9. Crystal structure of **5**. The hydrogens, imido *tert*-butyl groups, solvent molecules and a crystallographically unique but structurally analogous molecule of **5** are omitted for clarity. Thermal ellipsoids are drawn at 50% probability.

Table 2.5. Selected bond lengths (Å) and angles (°) of **5**.

Bond	Lengths	Bond	Angles
Fe(1)–Fe(1A)	2.5344(5)	O(1)–Fe(1)–O(2)	128.06(7)
Fe(1)–N(2)	1.785(2)	O(2)–Fe(1)–N(1)	81.72(7)
Fe(1)–N(2A)	1.824(2)	N(1)–Fe(1)–N(2)	166.86(8)
Fe(1)–O(2)	1.919(2)	N(1)–Fe(1)–N(2A)	102.34(8)
Fe(1)–O(1)	1.915(2)	Fe(1)–N(2)–Fe(1A)	89.20(8)
C(16) –O(2)	1.322(3)	N(2)–Fe(1)–N(2A)	90.80(8)
C(15) –N(1)	1.383(3)		
C(15) –C(16)	1.421(3)		
C(16) –C(17)	1.424(4)		
C(17) –C(18)	1.382(3)		

C(18) –C(19)	1.413(3)
C(19) –C(20)	1.371(4)
C(15) –C(20)	1.404(3)

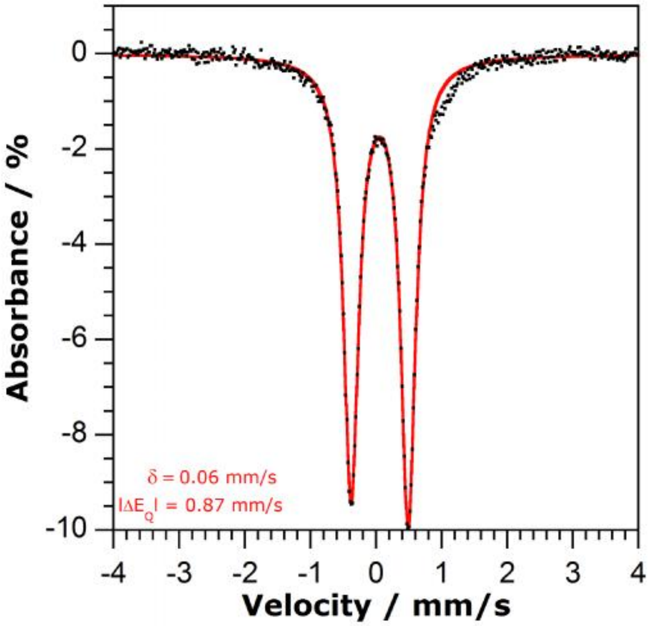

Figure 2.10. Mössbauer spectrum of $\{[ONO^q]Fe(«\text{-N}t\text{Bu})\}_2$ (**5**). Data collected at 95 K.

The structural and electronic properties of **5** have also been investigated through NMR and Mössbauer spectroscopy. Interestingly, complex **5** is diamagnetic in contrast to other [ONO]Fe complexes reported in this chapter. The ^{13}C NMR spectrum of this compound reveals a resonance at 173 ppm, corresponding to a C=O fragment, and is in agreement with the presence of the carbonyl found in the $[ONO^q]^{1-}$ ligand. The ^{1}H NMR spectrum of the diiron complex displays four resonances and the ^{13}C NMR spectrum shows twelve resonances, an implication that **5** likely adopts a D_{4h} symmetric structure in solution. The Mössbauer spectrum of **5** shows one quadrupole doublet with ΔE_Q = 0.87 mm/s (Figure 2.10), ascertaining that both iron centers have identical coordination environments and consistent with the argument that the structure of **5** is highly symmetric. An isomer shift value of 0.06 mm/s indicates that the diiron complex contains low-spin Fe(III) centers.[23]

2.2.4 Synthesis and Characterization of [ONO^{cat}]FeL$_n$ Complexes

Iron complexes containing the fully-reduced form of the [ONO] ligand were accessed via reaction of [ONO^{cat}]H$_3$ and FeCl$_3$ in the presence of coordinative L-type ligands and a base. The synthetic routes towards preparation of [ONO^{cat}]Fe(dppe) (**6**) and [ONO^{cat}]Fe(py)$_3$ (**7**) (py = pyridine; dppe = 1,2-bis(diphenylphosphino)ethane) are shown in Scheme 2.6. To toluene solutions containing the FeCl$_3$, dppe, and triethylamine, the addition of [ONO^{cat}]H$_3$ at ambient temperature led to precipitation of triethylammonium chloride salts and concomitant generation of **6** in 98% yield. Dark red crystals of **6** were isolated in saturated acetonitrile solutions of the compound at room temperature for X-ray crystallography measurements. Treatment of FeCl$_3$ with [ONO^{cat}]H$_3$ in pyridine solutions containing triethylamine led to elimination of triethylammonium chloride salts and simultaneous formation of **7** in 70% yield. Green crystals of **7** suitable for X-ray crystallography were isolated via diffusion of acetonitrile into pyridine solutions of the compound at –35 °C.

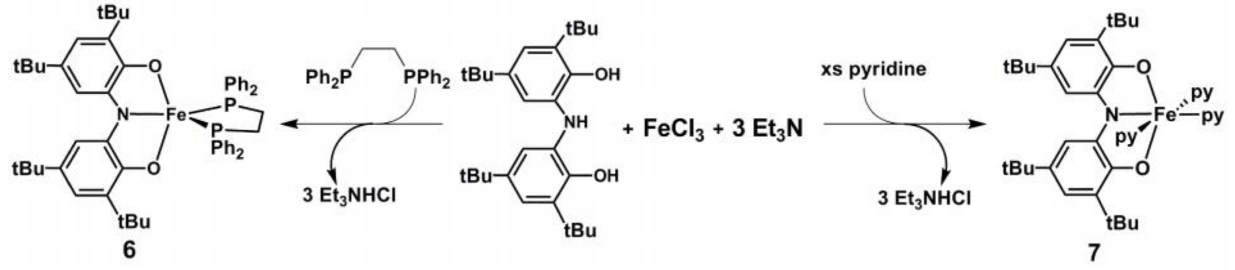

Scheme 2.6. Synthesis of [ONO^{cat}]FeL$_n$ complexes.

The structural properties and ligand and metal oxidation states of **6** have been investigated through X-ray crystallographic data. An ORTEP diagram of **6** as well as the selected bond measurements are shown in Figure 2.11 and Table 2.6, respectively. Given that ~ = ∠O(1)–Fe(1)–O(2) and = ∠N(1)–Fe(1)–P(1), ² = 0.59, an implication that the geometry of the solid-state structure of **6** lies in between square pyramidal and trigonal bipyramidal geometries.[22]

The carbon–oxygen bond distances within the [ONO] ligand backbone average to be 1.34 Å, consistent with a C(aryl)–O single bond. The average C(1)–N(1) and C(15)–N(1) bond lengths of 1.39 Å indicate carbon–nitrogen single bond characters. Finally, the variation in the carbon–carbon bond lengths within the six-membered rings is consistent with electron delocalization within an aromatic system.[21] These bond metrical patterns are observed in other $[ONO^{cat}]M$ complexes (M = Ta,[15] Nb,[27] Rh[17]), indicating that the [ONO] ligand of complex **6** adopts the $[ONO^{cat}]^{3-}$ form and the oxidation state of iron is +3.

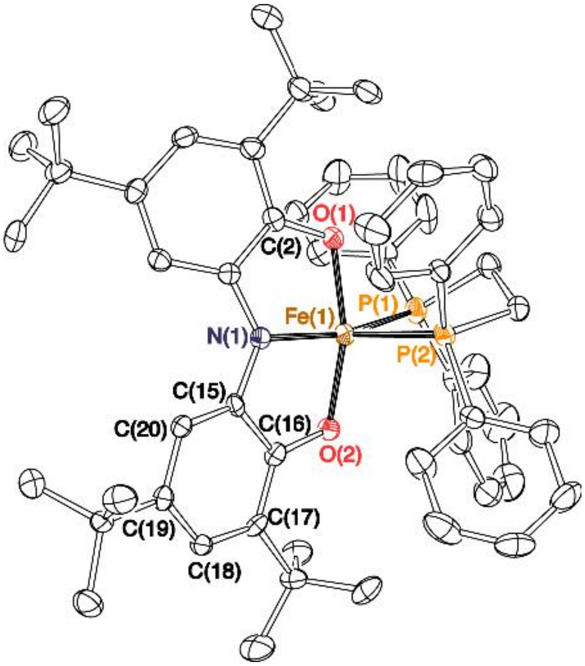

Figure 2.11. Crystal structure of **6**. The hydrogens and two crystallographically unique but identical crystal structures of **6** are removed for simplicity. Thermal ellipsoids are drawn at 50% probability.

Table 2.6. Selected bond lengths (Å) and angles (°) for **6**.

Bond	Length	Bond	Angle
C(2)–O(1)	1.341(5)	N(1)–Fe(1)–P(1)	133.1(1)
C(16)–O(2)	1.348(4)	N(1)–Fe(1)–O(1)	83.6(1)
C(1)–N(1)	1.406(4)	P(1)–Fe(1)–P(2)	83.18(4)
C(15)–N(1)	1.397(5)	O(1)–Fe(1)–O(2)	168.2(1)

C(15)–C(16)	1.417(5)
C(16)–C(17)	1.408(5)
C(17)–C(18)	1.384(6)
C(18)–C(19)	1.406(6)
C(19)–C(20)	1.388(6)
C(15)–C(20)	1.391(6)
Fe(1)–P(1)	2.2569(9)
Fe(1)–P(2)	2.248(1)
Fe(1)–N(1)	1.815(3)
Fe(1)–O(1)	1.895(3)
Fe(1)–O(2)	1.881(3)

EPR spectroscopy has been employed to probe the electron properties of **6**. Figure 2.12 displays rhombic EPR signals for **6** with *g* values of 2.04, 2.13, and 2.22. These resonances are consistent with the metal complex exhibiting low-spin iron(III) behavior. A small signal at $g = 4.23$ is indicative of the presence of high-spin iron(III) impurity.[24]

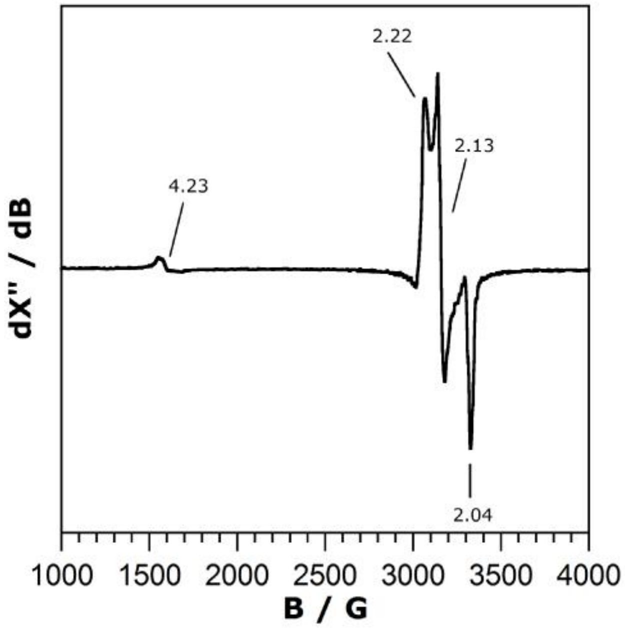

Figure 2.12. X-band EPR spectrum of [ONO^{cat}]Fe(dppe) (**6**). Experimental conditions: $B_1 \perp B_0$; solvent, toluene; temperature, 77 K.

Single-crystal X-ray crystallography has also been applied to interrogate the structural properties [ONO^{cat}]Fe(py)$_3$ (**7**) in order to assign formal charges to the metal and ligand. The ORTEP diagram of **7** is shown in Figure 2.13 while selected bond lengths and angles are listed in Table 2.7. The average C(2)–O(1) and C(16)–O(2) bond length of 1.34 Ǻ is consistent with the presence of carbon–oxygen single bonds in the [ONO] ligand backbone. The C(1)–N(1) and C(15)–N(1) bonds have very similar lengths of 1.395(3) Å and 1.392(3) Å, respectively, which are indicative of C–N single bond character. The variation in the carbon–carbon bond lengths within the six-membered rings are also consistent with electron delocalization within an aromatic system.[21] These bond length measurements also confirm that the [ONO] ligand of **7** adopt the [ONO^{cat}]$^{3-}$ form. The N(1)–Fe(1)–N(2), N(1)–Fe(1)–N(4), and O(1)–Fe(1)–O(2) bond angles of 178.73(7)°, 90.70(7)°, and 163.68(6)°, respectively, is consistent with a pseudo-octahedral geometry at the iron center of **7**.

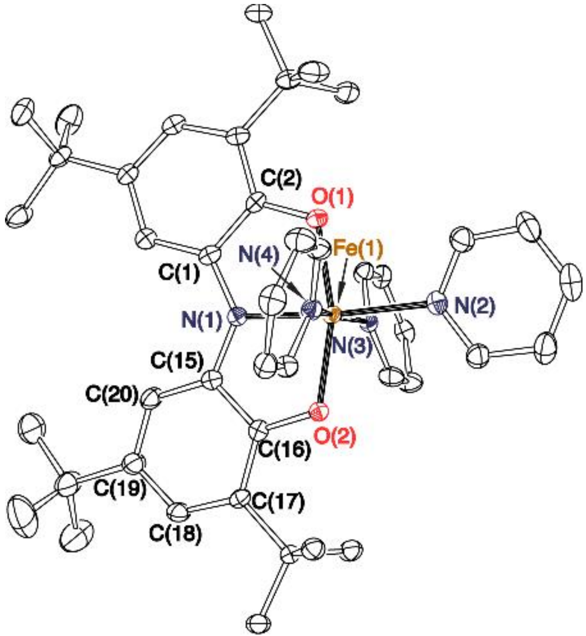

Figure 2.13. Crystal structure of [ONO^{cat}]Fe(py)$_3$ (**7**). Hydrogen atoms, solvent molecules, and a crystallographically unique but structurally analogous molecule of **7** have been omitted for clarity. Thermal ellipsoids are drawn at 50% probability.

Table 2.7. Selected bond lengths (Å) and angles (°) of **7**.

Bond	Length	Bond	Angle
C(2)–O(1)	1.338(3)	O(1)–Fe(1)–O(2)	163.68(6)
C(16)–O(2)	1.344(2)	N(1)–Fe(1)–N(2)	178.73(7)
C(1)–N(1)	1.395(3)	N(1)–Fe(1)–N(4)	93.70(7)
C(15)–N(1)	1.392(3)		
C(15)–C(16)	1.441(3)		
C(16)–C(17)	1.402(3)		
C(17)–C(18)	1.401(3)		
C(18)–C(19)	1.392(3)		
C(19)–C(20)	1.400(3)		
C(15)–C(20)	1.401(3)		
Fe(1)–O(1)	1.950(2)		
Fe(1)–O(2)	1.949(2)		
Fe(1)–N(1)	1.982(2)		
Fe(1)–N(2)	2.145(2)		
Fe(1)–N(3)	2.252(2)		
Fe(1)–N(4)	2.238(2)		

Complex **7** has been further characterized through spectroscopic methods in order to investigate the electronic behavior of the metal center. Figure 2.14 displays the Mössbauer and EPR spectra of **7**. The isomer shift value of 0.37 mm/s indicates **7** is an $S = \frac{5}{2}$ system.[23] The EPR spectrum shows *g* values of 9.34 and 4.03, in agreement with the metal complex adopting a high-spin iron(III) center.[24]

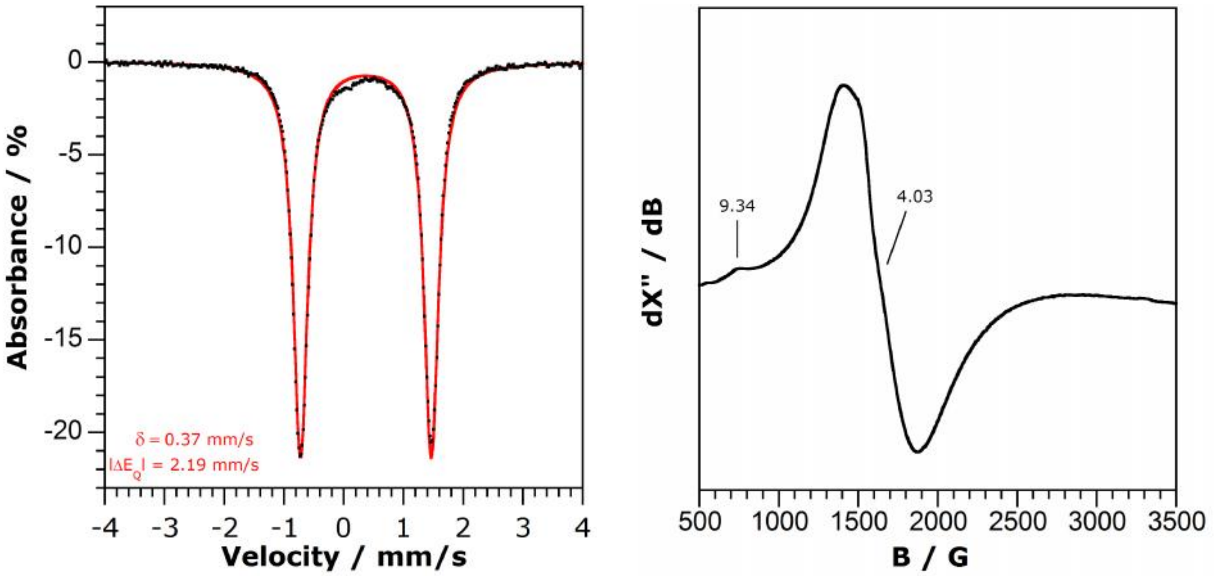

Figure 2.14. (*Left*) Mössbauer spectrum of [ONO^{cat}]Fe(py)$_3$ (**7**). Data collected at 90 K. (*Right*) X-band EPR spectrum of **7**. Experimental conditions: $B_1 \perp B_0$; solvent, pyridine; temperature, 77 K.

2.3 Discussion

2.3.1 Reactivity of [ONHO]Fe^{II}(BDI-mes)

Towards our goal of preparing new iron complexes that exhibit ligand-based redox activity, we attempted to remove the amino proton of the [ONHO] ligand of [ONHO]Fe(BDI-mes) (**2**) and subsequently oxidize the complex. However, these synthetic routes led to decomposition product (Scheme 2.4). We postulated that upon deprotonation and oxidation, the putative iron product could adopt one of the following forms: [ONO^{cat}]Fe^{III}(BDI-mes) or [ONO^{sq}]Fe^{II}(BDI-mes) (Scheme 2.7). Due to the hardness of iron(III), coordination of the soft diimine ligand may not be preferable, leading to disproportionation of the putative iron(III) compound. Thus, [ONO^{cat}]Fe^{III}(BDI-mes) could not be observed. Reaction of K$_2$[ONO^{sq}] and (BDI-mes)FeCl$_2$ (**1**) led to extrusion of the free diimine, an indication that coordination of the redox-active [ONO] ligand to iron(II) was unfavored and formation of [ONO^{sq}]Fe^{II}(BDI-mes) was not possible. These factors motivated us to prepare redox-active [ONO]Fe complexes through the use of iron(III) salts and fully-deprotonated forms of the [ONO] ligand synthons.

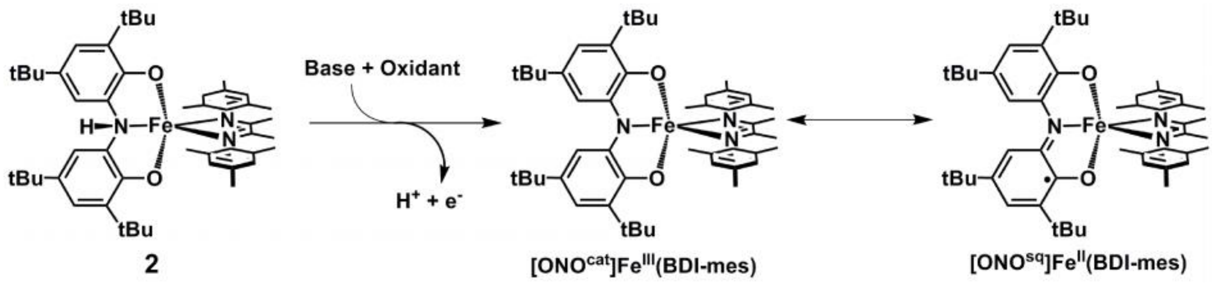

Scheme 2.7. Deprotonation and oxidation of **2** leading to putative iron product containing two possible isomers.

2.3.2 Ligand and Metal Oxidation State Assignments

Coordination of the redox-active [ONO] ligand to the iron center leads to ambiguity in determining the oxidation states of the ligand and metal center. Reaction of K[ONO^{q}] with various iron(III) salts produces formally iron(III) complexes of the formula: [ONO^{q}]FeX$_2$ (X =Cl (**3a**); Br (**3b**); N(SiMe$_3$)$_2$ (**4**); «-N*t*Bu (**5**)). Because the [ONO] ligand is able to collect single electrons, the ligand can be in the [ONO^{sq}]$^{2-}$ form coordinated to an iron (IV) metal center. With the exception of several non-heme iron enzymes, complexes containing formal iron(IV) metal centers are rarely observed.[28] Another possible isomer is the [ONO^{cat}]$^{3-}$ ligand coordinated to the iron(V) metal center. However, with the exception of select "true" non-heme iron(V)–oxo or iron(V) nitride species, most formally iron(V) complexes are better described as iron(IV) compounds possessing ligand radical species.[29] Hence, the best way to describe **3J5** is an iron(III) complex coordinated to [ONO^{q}]$^{1-}$. These electronic assignments are further supported by the structural data obtained from X-ray crystallography as well as EPR, Mössbauer, and NMR spectroscopic data for the metal complexes.

On the other hand, complexes **6** and **7** have been assigned as [ONO^{cat}]FeL$_n$, an implication that both are formally iron(III) compounds. Because the fully reduced form of the ligand can donate single electrons, two plausible electron distributions also exist: [ONO^{q}]Fe^{I}L$_n$ or [ONO^{sq}]Fe^{II}L$_n$. Low-valent iron(I) complexes have been invoked as intermediates in various cross-coupling catalytic cycles.[1] However, their instability has precluded further spectroscopic studies to confirm the identity and oxidation states of the iron species. While a family of dinuclear iron(I) complexes have been prepared and characterized that exhibit unique reactivity,[7] the ability to isolate metal complexes containing iron(I) is nonetheless uncommon.[6, 8d] Iron(II) complexes ligated to redox-active ligands have been reported in the literature,[9, 10, 11] which suggests that synthesis of $[ONO^{sq}]Fe^{II}L_n$ is theoretically possible. However, as we have established earlier, coordination of the $[ONO^{sq}]^{2-}$ to an iron(II) center is not favored. Furthermore, crystallographic and spectroscopic evidences support that complexes **6** and **7** are best described as iron(III) complexes supported by the $[ONO^{cat}]^{3-}$ ligand.

2.3.3 Electronic Properties of [ONO]Fe Complexes

The diamagnetic nature of **5** gives rise to the question of how the electrons interact within the diiron compound. The Fe–Fe distance of 2.5344(5) Å in complex **5** is only slightly longer than a Fe–Fe bond length of 2.48 Å.[26] Since the two irons lie close to each other, it is possible that the singly unpaired electron at each metal facilitate an iron–iron bond. Another possibility is that the radicals at each iron are antiferromagnetically coupled to one another, making **5** an $S = 0$ system.

Qualitative analyses based on coordination geometries can be used to describe the electronic differences among the iron(III) complexes **3**–**6**. While all five complexes possess distorted five-coordinate geometry, the ^{2} values of 0.18, 0.12, and 0.13 for $[ONO^{q}]FeCl_2$ (**3a**), $[ONO^{q}]FeBr_2$ (**3b**), and $[ONO^{q}]Fe[N(SiMe_3)_2]_2$ (**4**), respectively, indicate that their geometries lie much closer to a square pyramid than trigonal bipyramid. In contrast, ^{2} values of 0.64 and 0.59 for $\{[ONO^{q}]Fe(«\text{-N}t\text{Bu})\}_2$ (**5**) and $[ONO^{cat}]Fe(dppe)$ (**6**), correspondingly, suggest that neither complexes show clear preferences for square pyramidal or trigonal bipyramidal geometries. Nevertheless, both complexes deviate from the square pyramidal geometries, which may lead to destabilization of the d_{z^2} orbital. The higher energy of the orbitals of $d_{x^2-y^2}$ and d_{z^2} parentage may have provided for the low-spin $S = \frac{1}{2}$ configuration observed for complexes **5** and **6** as opposed to the high-spin $S = \frac{5}{2}$ configuration for **3a**, **3b**, and **4**. While the electronic behaviors of complexes **3–6** can be described through qualitative observations, quantitative analyses using techniques such as DFT calculations may provide more accurate explanations.

2.4 Summary and Conclusions

The versatility of the [ONO] ligand platform offers a wide array of pathways towards the synthesis of various [ONO] metal complexes. Due to the accessibility of all three [ONO] ligand scaffold oxidation states, a new series of redox-active complexes have been prepared where a single [ONO] ligand is coordinated to iron. The electronic properties of the $[\mathrm{ONHO}]\mathrm{Fe}^{\mathrm{II}}$(BDI-mes), $[\mathrm{ONO}^{\mathrm{q}}]\mathrm{Fe}^{\mathrm{III}}\mathrm{X}_2$, and $[\mathrm{ONO}^{\mathrm{cat}}]\mathrm{Fe}^{\mathrm{III}}\mathrm{L}_n$ compounds have been explored in order to evaluate their potential to facilitate multi-electron reactivity. While oxidation of the iron(II) complex leads to decomposition product, coordination of the redox-active [ONO] moiety to iron(III) suggest that redox reactivity should be achievable through these complexes. Chapter 3 will detail the reactivity of the $[\mathrm{ONO}^{\mathrm{q}}]\mathrm{FeX}_2$ and $[\mathrm{ONO}^{\mathrm{cat}}]\mathrm{FeL}_n$ complexes.

2.5 Experimental

General Procedures. All compounds and reactions reported below require manipulations to be carried out under air- and moisture-free conditions using standard glovebox techniques or Schlenk techniques. Solvents were sparged with argon and then deoxygenated and dried by passage through Q5 and activated alumina columns, respectively. To test for effective oxygen and water removal, solvents were treated with a few drops of a purple solution of sodium benzophenone ketyl in THF. The C_6D_6 NMR solvent was dried in sodium-potassium amalgam benzophenone ketyl for two days, followed by trap-to-trap vacuum distillation and several freeze-pump-thaw cycles.

The compounds $FeCl(THF)[N(SiMe_3)_2]_2$,[25a] $\{(t\text{BuNH}_2)\text{FeCl}(\mu\text{-N}t\text{Bu})\}_2$,[25b] $K[ONO^q]$,[17] and $[ONO^{cat}]H_3$ [15, 30] were synthesized according to published procedures. The synthesis of complexes **3a**, **4**, and **7** have also been reported previously.[18] Diphenylhydrazine was purchased from Alfa Aesar and sublimed before use. The pyridine (Macron), *tert*-butylthiol (Alfa Aesar), and triethylamine (Fisher Scientific) were dried with 4 Å molecular sieves (Fisher Scientific) overnight and then distilled under reduced pressure into a Straus flask and degassed through several freeze-pump-thaw cycles. Potassium hydride (Alfa Aesar) was washed with pentane to remove the oil prior to usage. The $FeCl_3$, $FeBr_3$, and 1,2-bis(diphenylphosphino)ethane were purchased from Strem and used without further purification.

Physical Measurements. The UV-vis-NIR spectra were recorded with Perkin–Elmer Lambda 800 Spectrometer as solutions in toluene, THF or pyridine. Electrospray ionization mass spectrometry MS(ESI) was performed at the Mass Spectrometry Facility at University of California, Irvine. NMR spectra were acquired on a Bruker Avance 400/500/600 MHz spectrometer. Perpendicular-mode X-band EPR spectra were collected using Bruker EMX spectrometer equipped with ER041XG microwave bridge. ^{57}Fe Mössbauer spectra were measured on liquid nitrogen cooled samples at zero magnetic field with a constant acceleration spectrometer (SEE Co., Edina, MN). Elemental analysis experiments have been performed on all new compounds, and the results of those that fall in the expected mass ranges are reported.

Crystallographic Methods. X-ray diffraction data were collected on crystals mounted on glass fibers using a Bruker CCD platform diffractometer equipped with a CCD detector. Measurements were carried out using Mo K_α (λ = 0.71073 Å) radiation, which was wavelength selected with a single-crystal graphite monochromator. A full sphere of data was collected for each crystal structure. The APEX2 program package was used to determine unit-cell parameters and to collect data.[31] The raw frame data were processed using SAINT[32] and SADABS[33] to yield the reflection data files. Subsequent calculations were carried out using the SHELXTL[34] program suite. Structures were solved by direct methods and refined on F^2 by full-matrix least-squares techniques to convergence. Analytical scattering factors for neutral atoms were used throughout the analyses. Hydrogen atoms, though visible in the difference Fourier map, were generated at calculated positions and their positions refined using the riding model. ORTEP diagrams were generated using ORTEP-3 for Windows[35] and all thermal ellipsoids are drawn at the 50% probability level.

Table 2.8. X-ray diffraction data-collection and refinement parameters for complexes **1**, **2**, **3a**, **3b**.

	1•($CHCl_3$)	**2**•1.5(C_5H_{12})	**3a**•C_7H_8	**3b**•2(C_7H_8)
Empirical formula	$C_{22}H_{29}Cl_2N_2Fe$• ($CHCl_3$)	$C_{50}H_{69}N_3O_2Fe$• 1.5(C_5H_{12})	$C_{28}H_{40}NO_2Cl_2Fe$• C_7H_8	$C_{28}H_{40}NO_2Cl_2Fe$• 2(C_7H_8)
Formula weight	566.58	911.13	641.49	822.55
Crystal system	Monoclinic	Monoclinic	Monoclinic	Orthorhombic
Space group	$P2_1/c$	$P2_1/n$	$P2_1/n$	$Pbca$
T	143(2) K	88(2) K	143(2) K	143(2) K
a	12.7925(6) Å	16.7902(9) Å	10.1903(6) Å	14.7919(9) Å
b	14.7081(7) Å	14.7504(8) Å	12.5783(8) Å	19.0608(12) Å
c	14.1838(7) Å	22.0971(12) Å	27.2498(17) Å	28.5218(18) Å
α	90°	90°	90°	90°
β	91.2696(6)°	99.2130(10)°	96.2952(8)°	90°
¥	90°	90°	90°	90°
V	2668.1(2) $Å^3$	5402.0(5) $Å^3$	3470.4(4) $Å^3$	8041.6(9) $Å^3$
Z	4	4	4	8
Reflections collected	30568	47699	36819	48014
data/restraints/parameters	6359 / 0 / 288	13013 / 1 / 612	7105 / 0 / 468	5804 / 0 / 447
R1 [$I > 2\sigma(I)$][a]	0.0378	0.0423	0.0341	0.0220
wR2 (all data)[a]	0.0964	0.1124	0.0802	0.0553
GOF[a]	1.038	0.746	1.026	1.027

[a] $R1 = \Sigma||F_o| - |F_c||/\Sigma|F_o|$; $wR2 = [\Sigma[w(F_o^2 - F_c^2)^2]/\Sigma[w(F_o^2)^2]]^{1/2}$; $GOF = [\Sigma w(|F_o| - |F_c|)^2/(n - m)]^{1/2}$

Table 2.9. X-ray diffraction data-collection and refinement parameters for complexes **4**, **5**, **6**, **7**.

	4	**5**•(C_4H_8O)	**6**	**7**•(C_2H_3N)
Empirical formula	$C_{40}H_{76}N_3O_2Si_4Fe$	$C_{64}H_{98}N_4O_4Fe_2$• (C_4H_8O)	$C_{54}H_{64}NO_2P_2Fe$	$C_{43}H_{55}N_4O_2Fe$• (C_2H_3N)
Formula weight	799.25	1171.26	876.85	756.81
Crystal system	Monoclinic	Triclinic	Triclinic	Monoclinic
Space group	$P2_1/c$	$P\bar{1}$	$P\bar{1}$	$P2_1$
T	143(2) K	88(2) K	143(2) K	88(2) K
a	11.9269(7) Å	13.7409(6) Å	15.7749(11) Å	14.0101(6) Å
b	17.5744(10) Å	14.4065(6) Å	19.6249(14) Å	15.7187(7) Å
c	24.1583(13) Å	18.4223(8) Å	25.7121(19) Å	19.9340(8) Å
α	90°	70.9781(5)°	101.1161(11)°	90°
β	111.5826(6)°	88.5738(5)°	103.8271(11)°	97.6912(5)°
¥	90°	82.8514(5)°	104.4414(10)°	90°
V	4708.75 Å^3	3420.4(3) Å^3	7210.4(9) Å^3	4350.38 Å^3
Z	4	2	6	4
Reflections collected	11228	37006	72624	47597
data/restraints/parameters	11228 / 0 / 756	13907 / 0 / 713	26313 / 0 1657	17560 / 1 / 981
R1 [$I > 2\sigma(I)$][a]	0.0297	0.0432	0.0559	0.0354
wR2 (all data)[a]	0.0737	0.1204	0.1219	0.0877
GOF[a]	1.032	1.039	0.974	1.008

[a] $R1 = \Sigma||F_o| - |F_c||/\Sigma|F_o|$; $wR2 = [\Sigma[w(F_o^2 - F_c^2)^2]/\Sigma[w(F_o^2)^2]]^{1/2}$; $GOF = [\Sigma w(|F_o| - |F_c|)^2/(n - m)]^{1/2}$

Synthesis of (BDI-mes)FeCl$_2$ (1). A solution containing 1.38 g of BDI-mes (4.31 mmol, 1 equiv.) in 25 mL of THF was cooled at 77 K and then charged with 543 mg of iron(II) chloride (4.32 mmol, 1 equiv.). After stirring for 12 hours as inside the glovebox as it warms to ambient temperature, the resulting dark green solution was placed under vacuum to remove the solvent and revealed red solids. Solids were recrystallized from layer diffusion of dichloromethane and diethyl ether at 238 K overnight to yield dark red crystalline material. ^{1}H Yield: 1.57 g (81%). ^{1}H NMR (500 MHz, $CDCl_3$) δ/ppm: 1.869 (s, 12H), 11 (s, 8H), 14.778 (s, 4H), 99 (s, 4H).

Synthesis of [ONHO]Fe(BDI-mes) (2). A solution containing 400 mg of [ONO^{cat}]H_3 (0.941 mmol, 1 equiv.) in 30 mL of THF was cooled at 77 K and then charged with 84.8 mg of KH (2.12 mmol, 2.25 equiv.). After stirring at room temperature for 2 hours, the light green solution was cooled again at 77 K before 420 mg of **1** (0.940 mmol, 1 equiv.) was added. After stirring at room temperature for 24 hours, the resulting dark brown-green solution was placed under vacuum to remove the solvent. Following coevaporation of the residue with diethyl ether and then with pentane, the product was extracted with pentane and concentrated to half the volume before cooling at 238 K overnight. Dark green crystalline materials were isolated and liquid filtrate was concentrated to half the volume before cooling again overnight to recover more product. Yield: 517 mg (69%). IR (KBr) ν(N–H)/cm^{-1}: 3282. UV-vis-NIR (THF) λ_{max}/nm (ε/ M^{-1}cm^{-1}): 302 (6,000).

Synthesis of [ONO^q]FeCl$_2$ (3a). A 75 mL toluene suspension of 1.13 g of $FeCl_3$ (6.97 mmol, 1 equiv.) was cooled at 77 K followed by addition of 3.22 g K[ONO^q] (6.98 mmol, 1 equiv.). After stirring for 15 hours at ambient temperature, the solid byproducts were removed via vacuum filtration and washed with toluene. The combined toluene fractions were then concentrated to 50 mL and recrystallized from a mixture of toluene and pentane solution at 238 K overnight. Dark brown crystalline solids were obtained in 71% yield (2.70 g). Anal. calc. (Found) for $C_{28}H_{40}NO_2Cl_2Fe$ (%): C, 61.22 (60.99); H, 7.34 (7.25); N, 2.55 (2.48). UV-vis-NIR (Toluene) λ_{max}/nm (ε/ M^{-1} cm^{-1}): 318 (13,200), 456 (7,000), 840 (7,000), 930 (10,600). MS(ESI$^-$) m/z: 548.14 (M+), 550.14 (M+2), 552.15 (M+4).

Synthesis of [ONO^q]FeBr$_2$ (3b). A solution containing 762 mg of $FeBr_3$ (2.58 mmol, 1 equiv.) in 50 mL THF was cooled at 77K and then charged with 1.19 g of K[ONO^q] (2.58 mmol, 1 equiv.). After stirring for 15 hours, dark green solution was placed under vacuum to remove the solvent. The residue was coevaporated and then extracted with diethyl ether. The residue was recrystallized from layer diffusion of diethyl ether and pentane and cooled at 238 K overnight. Dark brown solids were isolated and the liquid filtrate was concentrated before adding more pentane to the solution and cooled overnight at 238 K. Yield: 1.18 g (72%). UV-vis-NIR (THF)

λ_{max}/nm (ε/ $M^{-1}cm^{-1}$): 226 (14,400), 438 (11,700), 664 (4,200), 856 (7,600). MS(ESI^{-}) m/z: 636.09 (M+), 638.09 (M+2), 640.09 (M+4).

Synthesis of [ONO^{q}]Fe[N(SiMe$_3$)$_2$]$_2$ (4). To a 50 mL pentane solution containing 2.63 g of FeCl(THF)[N(SiMe$_3$)$_2$]$_2$ (5.69 mmol, 1 equiv.), 2.74 g of K[ONO^{q}] (5.69 mmol, 1 equiv.) was slowly added. After stirring for 15 hours, the solid byproducts were removed via vacuum filtration and washed with pentane. The combined pentane fractions were taken to dryness and the dark brown residue was recrystallized from a mixture of toluene and acetonitrile solution at 238 K overnight. Dark brown solids were obtained in 65% yield (2.97 g). UV-vis-NIR (Toluene) λ_{max}/nm (ε/ $M^{-1}cm^{-1}$): 458 (10,100), 872 (10,600), 914 (11,000). Anal. Calc. (Found) for $C_{40}H_{76}N_3O_2Si_4Fe$ (%): C, 60.11 (60.10); H, 9.58 (9.82); N, 5.26 (5.09). 7.57 H 798.35 (M+), 799.98 (M+1).

Synthesis of ([ONO^{q}]Fe)$_2$(*μ*-N^{t}Bu)$_2$ (5). A 30 mL THF solution containing 380 mg of {(*t*BuNH$_2$)FeCl(*μ*-N*t*Bu)}$_2$ (0.812 mmol, 1 equiv.) was cooled at 77 K and then charged with 750 mg of K[ONO^{q}] (1.63 mmol, 2 equiv.). After stirring for 15 hours, the dark green solution was placed under vacuum to remove the solvents followed by coevaporation with pentane (2x15 mL). The product was extracted with 20 mL diethyl ether and concentrated to 8 mL. Acetonitrile was then added and dark green solution was cooled to 238 K for two days. Yield: 539 mg (60%). ^{1}H NMR (400 MHz, C_6D_6) δ/ppm: 1.49–1.50 (overlap, 72H, *t*Bu), 1.701 (s, 18H, N*t*Bu), 7.330 (s, 4H, aryl-H), 8.159 (s, 4H, aryl-H). UV-vis-NIR (THF) λ_{max}/nm (ε/ $M^{-1}cm^{-1}$): 470 (15,000), 762 (21,000).

Synthesis of [ONO^{cat}]Fe(dppe) (6). To a 10 mL toluene slurry containing 37.5 mg of $FeCl_3$ (0.231 mmol, 1 equiv.), 92.0 mg of 1,2-bis(diphenylphosphino)ethane (0.231 mmol, 1 equiv.) was added followed by addition of 96 μL triethylamine (0.69 mmol, 3 equiv.). Upon addition of the $[ONO^{cat}]H_3$ at ambient temperature, the dark red solution stirred at ambient temperature for 15 hours. The solid byproducts were isolated via vacuum filtration and washed with approximately 20 mL toluene. The liquid filtrate was then removed under vacuum to reveal dark red powder, which was subsequently washed with 5 mL of acetonitrile. Yield: 198 mg (98%).

Synthesis of $[ONO^{cat}]Fe(py)_3$ (7). To a 25 mL pyridine solution containing 970 mg of $FeCl_3$ (5.98 mmol, 1 equiv.), 2.70 mL of triethylamine (19.5 mmol, 3.26 equiv.) was added. Addition of the $[ONO^{cat}]H_3$ at ambient temperature produced a dark green solution accompanied formation of solids. After stirring for 20 hours, the dark green mixture was filtered to remove solid byproducts and washed with 25 mL of pyridine. The dark green solution was then concentrated to approximately 20 mL, after which acetonitrile was added and the solution was cooled to 238 K overnight to yield dark green microcrystalline solids. Yield: 2.90 g (69%). UV-vis-NIR (Pyridine) λ_{max}/nm (ε/ $M^{-1}cm^{-1}$): 342 (sh; 12,200), 384 (6,700), 432 (sh; 4,100), 504 (sh; 2,700), 618 (2,300), 1137 (3,000). Anal. calc. (Found) for $C_{43}H_{55}N_4O_2Fe$ (%): C, 72.15 (70.72); H, 7.75 (7.88); N, 7.83 (7.75).

2.6 References

[1] (a) Sherry, B. D. and Fürstner, A. *Acc. Chem. Res.* **2008**, *41*(11), 1500−1511. (b) Czaplik, W. M.; Mayer, M.; Cvengroš; Jacobi von Wangelin, A. *ChemSusChem* **2009**, *2*, 396−417. (c) Fürstner, A.; Leitner, A.; Méndez, M.; Krause, H. *J. Am. Chem. Soc.* **2002**, *124*, 13856−13863. (d) Tamura, M. and Kochi, J. *J. Am. Chem. Soc.* **1971**, *93*, 1487−1489. (e) Smith, R. S. and Kochi, J. K. *J. Org. Chem.*, **1976**, *41*, 502–509.

[2] (a) King, E. R.; Hennessy, E. T.; Betley, T. a *J. Am. Chem. Soc.* **2011**, *133*, 4917–4923. (b) Hennessy, E. T.; Betley, T. A. *Science* **2013**, *340*, 591–595.

[3] (a) *Iron Catalysis in Organic Chemistry*; Plietker, B., Ed.; Wiley-VCH: Weinheim, 2008. (b) *Iron Catalysis Fundamentals and Applications*; Plietker, B., Ed.; Springer-Verlag: Berlin Heidelberg, 2011.

[4] *Activation of Small Molecules*; Tolman, W. B., Ed.; Wiley-VCH: Weinheim, 2006.

[5] (a) Lee, Y.; Mankad, N. P.; Peters, J. C. *Nat. Chem.* **2010**, *2*, 558–565. (b) Moret, M.-E.; Peters, J. C. *J. Am. Chem. Soc.* **2011**, *133*, 18118–18121. (c) Takaoka, A.; Mankad, N. P.; Peters, J. C. *J. Am. Chem. Soc.* **2011**, *133*, 8440–8443. (d) Russell, S. K.; Darmon, J. M.; Lobkovsky, E.; Chirik, P. J. *Inorg. Chem.* **2010**, *49*, 2782–2792.

[6] (a) Lee, Y.; Kinney, R. A.; Hoffman, B. M.; Peters, J. C. *J. Am. Chem. Soc.* **2011**, *133*, 16366–16369. (b) Mankad, N. P.; Whited, M. T.; Peters, J. C. *Angew. Chemie* **2007**, *119*, 5870–5873. (c) Kisko, J. L.; Hascall, T.; Parkin, G. *J. Am. Chem. Soc.* **1998**, *7863*, 10561–10562.

[7] (a) Yu, Y.; Sadique, A. R.; Smith, J. M.; Dugan, T. R.; Cowley, R. E.; Brennessel, W. W.; Flaschenriem, C. J.; Bill, E.; Cundari, T. R.; Holland, P. L. *J. Am. Chem. Soc.* **2008**, *130*, 6624–6638. (b) Dugan, T. R.; Holland, P. L. *J. Organomet. Chem.* **2009**, *694*, 2825–2830.

[8] (a) Cowley, R. E.; Eckert, N. A.; Elhaïk, J.; Holland, P. L. *Chem. Commun.* **2009**, *48*, 1760–1762. (b) Mankad, N.; Müller, P.; Peters, J. C. *J. Am. Chem. Soc.* **2010**, *132*, 4083–4085. (c) Jensen, M. P.; Mehn, M. P.; Que, Jr., L. *Angew. Chem.* **2003**, *115*, 4493–4496. (d) Brown, S. D.; Betley, T. A.; Peters, J. C. *J. Am. Chem. Soc.* **2003**, *125*, 322–323. (e) Bowman, A. C.; Milsmann, C.; Bill, E.; Turner, Z. R.; Lobkovsky, E.; DeBeer, S.; Wieghardt, K.; Chirik, P. J. *J. Am. Chem. Soc.* **2011**, *133*, 17353–17369.

[9] Bart, S. C.; Lobkovsky, E.; Chirik, P. J. *J. Am. Chem. Soc.* **2004**, *126*, 13794–13807.

[10] Trovitch, R. J.; Lobkovsky, E.; Chirik, P. J. *Inorg. Chem.* **2006**, *45*, 7252–7260.

[11] (a) Bart, S. C.; Lobkovsky, E.; Bill, E.; Chirik, P. J. *J. Am. Chem. Soc.* **2006**, *128*, 5302–5303. (b) Bart, S. C.; Chłopek, K.; Bill, E.; Bouwkamp, M. W.; Lobkovsky, E.; Neese, F.; Wieghardt, K.; Chirik, P. J. *J. Am. Chem. Soc.* **2006**, *128*, 13901–13912. (c) Bart, S. C.; Lobkovsky, E.; Bill, E.; Wieghardt, K.; Chirik, P. J. *Inorg. Chem.* **2007**, *46*, 7055–7063.

[12] (a) Chirik, P. J.; Wieghardt, K. *Science* **2010**, *327*, 794–795. (b) Bouwkamp, M. W.; Bowman, A. C.; Lobkovsky, E.; Chirik, P. J. *J. Am. Chem. Soc.* **2006**, *128*, 13340–13341. (c) Sylvester, K. T.; Chirik, P. J. *J. Am. Chem. Soc.* **2009**, *131*, 8772–8774. (d) Russell, S. K.; Lobkovsky, E.; Chirik, P. J. *J. Am. Chem. Soc.* **2011**, *133*, 8858–8861.

[13] (a) Girgis, A. Y.; Balch, A. L. *Inorg. Chem.* **1975**, *14*, 2724–2727. (b) Simpson, C. L.; Boone, S. R.; Pierpont, C. G. *Inorg. Chem.* **1989**, *28*, 4379–4385.

[14] (a) Chauduri, P.; Hess, M.; Weyhermuller, T.; Wieghardt, K. *Inorg. Chem.* **1999**, *38*, 2781–2790. (b) McGarvey, B. R.; Ozarowski, A.; Tian, Z.; Tuck, D. G. *Can. J. Chem.* **1995**, *73*, 1213–1222. (c) Attia, A. S.; Conklin, B. J.; Lange, C. W.; Pierpont, C. G. *Inorg. Chem.* **1996**, *35*, 1033–1038.

[15] Zarkesh, R. A.; Ziller, J. W.; Heyduk, A. F. *Angew. Chem. Int. Ed.* **2008**, *47*, 4715–4718.

[16] Szigethy, Géza; Heyduk, A. *Dalton Trans.* **2012**, *41*, 8144–8152.

[17] Szigethy, G.; Shaffer, D. W.; Heyduk, A. F. *Inorg. Chem.* **2012**, *51*, 12606–12618.

[18] Wong, J. L.; Sánchez, R. H.; Logan, J. G.; Zarkesh, R. A.; Ziller, J. W.; Heyduk, A. F. *Chem. Sci.* **2013**, *4*, 1906–1910.

[19] Bart, S. C.; Hawrelak, E. J.; Schmisseur, A. K.; Lobkovsky, E.; Chirik, P. J. *Organometallics* **2004**, *23,* 237–246.

[20] (a) Ghosh, M.; Sproules, S.; Weyhermüller, T.; Wieghardt, K. *Inorg. Chem.* **2008**, *47*, 5963–5970. (b) Khusniyarov, M. M.; Weyhermüller, T.; Bill, E.; Wieghardt, K. *J. Am. Chem. Soc.* **2009**, *131*, 1208–1221.

[21] Allen, F. H.; Kennard, O.; Watson, D. G. *J. Chem. Soc. Perkin Trans. II* **1987**, S1–S19.

[22] Trans, D.; Addison, A. W.; Rao, T. N. *J. Chem. Soc. Dalt. Trans.* **1984**, 1349–1356.

[23] Gütlich, P.; Bill, E.; Trautwein, A. X. *Mössbauer Spectroscopy and Transition Metal Chemistry*; Springer-Verlag: Berlin Heidelberg, 2011; p 85.

[24] Que, Jr., L. *Physical Methods in Bioinorganic Chemistry*; University Science Books: Sausalito, CA, 1999; 134–185.

[25] (a) Duncan, J. S.; Tamim, M. N.; Verma, A. K.; Lee, S. C. *Inorg. Chem.* **2003**, *42*, 1211–1224. (b) Duncan, J. S.; Zdilla, M. J., and Lee, S. C. *Inorg. Chem.* **2007**, *46*, 1071–1080.

[26] (a) Pauling, L. *Proc. Natl. Acad. Sci. USA* **1976**, *73*(12), 4290–4293. (b) Cotton, F. A.; Wilkinson, G.; Murillo, C. A.; Bochmann, M. *Advanced Inorganic Chemistry*, 6th ed., Wiley, New York, **1999**, p. 795.

[27] Hananouchi, S. P. MS Thesis, University of California, Irvine, 2014.

[28] (a) Lacy, D. C.; Gupta, R.; Stone, K. L.; Greaves, J.; Ziller, J. W.; Hendrich, M. P.; Borovik, A. S. *J. Am. Chem. Soc.* **2010**, *132*, 12188–12190. (b) Nam, W. *Acc. Chem. Res.* **2007**, *40*, 522–531.

[29] (a) Dey, A.; Ghosh, A. *J. Am. Chem. Soc.* **2002**, *124*, 3206–3207. (b) de Oliveira, F. T.; Chanda, A.; Banerjee, D.; Shan, X.; Mondal, S.; Que, L. Jr.; Bominaar, E. L.; Münck, E.; Collins, T. J. *Science*, **2007**, *315*, 835–838. (c) Grapperhaus, C. A.; Mienert, B.; Bill, E.; Weyhermüller; Wieghardt, K. *Inorg. Chem.*, **2000**, *39*, 5306–5317.

[30] Chaudhuri, P.; Hess, M.; Weyhermüller, T.; Wieghardt, K. *Angew. Chem. Int. Ed.* **1999**, *38*, 1095–1098.

[31] APEX2, Version 2008.3-0 / 2.2-0, Bruker AXS, Inc.; Madison, WI 2007.

[32] SAINT Version 7.53a / 7.46a, Bruker AXS, Inc.; Madison, WI 2007.

[33] Sheldrick, G. M. *SADABS*, Version 2007/4, Bruker AXS, Inc.; Madison, WI 2007.

[34] Sheldrick, G. M. *SHELXTL*, Version 6.12; Brucker AXS, Inc.: Madison, WI, 2001.

[35] International Tables for X-Ray Crystallography 1992, Vol. C., Dordrecht: Kluwer Academic Publishers.

Chapter 3

Reactivity of Iron Complexes Coordinated to the Redox-Active [ONO] Ligand

Portions of this work have been reported previously:
Wong, J. L.; Sánchez, R. H.; Logan, J. G.; Zarkesh, R. A.; Ziller, J. W.; Heyduk, A. F. *Chem. Sci.* **2013**, *4*, 1906–1910.

3.1 Introduction

Driven by the need to develop cost-effective and environmentally benign alternatives to toxic and expensive metal catalysts, research in iron-catalyzed organic transformations has been gaining momentum in recent years.[1] Multi-electron transformations tend to be catalyzed most efficiently by precious metals such as Pd, Ir, and Rh due to their strong proclivity towards two-electron changes to their oxidation states.[2] In contrast, iron complexes are typically dominated by the one-electron $Fe^{III/II}$ redox couple, making their complexes generally not amenable to well-controlled two-electron transformations. One strategy to promote two-electron reactivity at the base-metal center is through the use of redox-active ligands.[3]

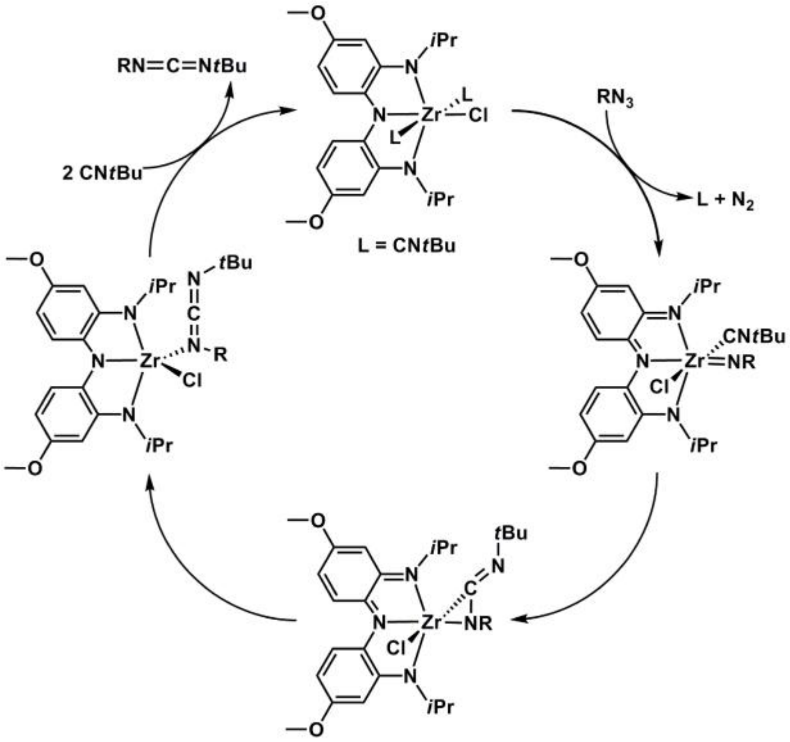

Scheme 3.1. Catalytic nitrene transfer reactivity mediated by Zr(IV) coordinated to a redox-active ligand.

Redox-active ligands are capable of accessing multiple oxidation states and thus hold promise as electron or hole reservoirs when coordinated to a metal ion. This view is exemplified through the ligand-enabled redox-reactivity pathways of early-transition metal complexes.[4, 5, 6] As illustrated in Scheme 3.1, coordination of the redox-active [NNN] ligand platform

([NNN^{cat}]H$_3$ = bis(2-isopropylamino-4-methoxyphenylamine)) to a zirconium(IV) metal center allows for redox reactivity to occur at the redox-inert d^0 metal center.[6, 7] While the metal oxidation states remain unchanged, the ligand undergoes reversible two-electron oxidation state changes, facilitating catalytic turnovers in a zirconium complex where zirconium(II) is not readily accessible.

By examining redox-active ligands in the context of base-metal complexes, the ligand redox activity can be exploited to promote two-electron reactivity previously unprecedented in such systems. Iron(II) complexes containing the redox-active [PDI] ligand scaffold ([PDI] = pyridine diimine) have been shown to undergo ligand-enabled bond activation of small molecules and catalytic transformations.[3, 8, 9] As discussed in Chapter 2, a series of redox-active iron complexes containing the [ONO] ligand scaffold ([ONO^{cat}]H$_3$ = bis(3,5-di-*tert*-butyl-2-phenol)amine) has been developed in our laboratory.[10] To further develop the chemistry of the [ONO]Fe platform, oxidative addition and reductive elimination reactions have been pursued as a way to investigate the multi-electron chemistry imparted by the redox-active ligand set. These studies provide deeper insights into how the interaction between the iron and the ligand can influence the bond-breaking and bond-forming processes that are potentially useful in catalysis.

3.2 Results

3.2.1 Synthesis and Characterization of {[ONO^q]Fe(cat-Cl$_4$)}$_2$ and [ONO^q]Fe(cat-Cl$_4$)(py)

The basicity of the amide ligands of [ONO^q]Fe[N(SiMe$_3$)$_2$]$_2$ (**4**) suggested that protonolysis might be a suitable method for introducing new X-type ligands to the [ONO]Fe platform.[10] As shown in Scheme 3.2, addition of one equivalent of tetrachlorocatechol (cat-Cl$_4$) to benzene solutions of **4** at room temperature produced the dimer {[ONO^q]Fe(cat-Cl$_4$)}$_2$ (**8**). X-ray quality green crystals of **8** were obtained from saturated pentane solutions of the bimetallic complex at −35 °C. Dimer **8** was highly soluble in organic solvents and as such, crystalline yields of the complex were low. To circumvent solubility issues, the monomeric form of the dimer was targeted for synthesis. Treatment of **8** in diethyl ether with excess pyridine afforded the [ONO^q]Fe(cat-Cl$_4$)(py) (**9**) in 63% yield. Green crystals of **9** suitable for X-ray crystallography were obtained from saturated diethyl ether solutions of the monomer at −35 °C.

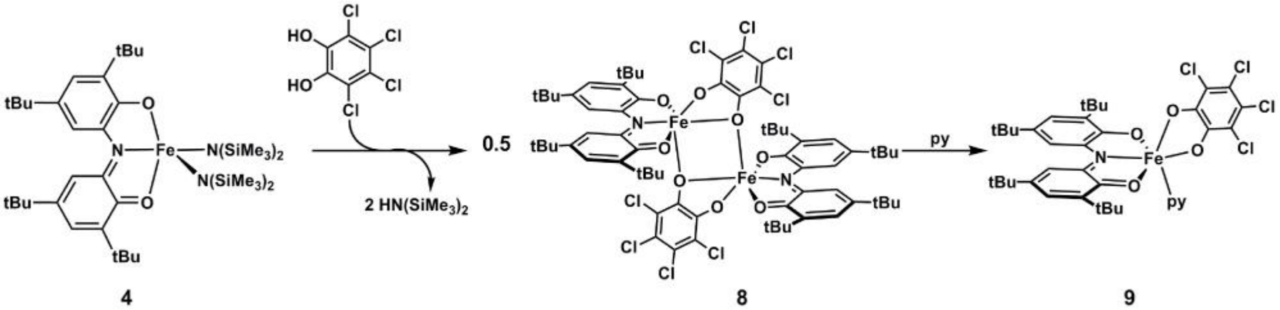

Scheme 3.2. Synthesis of **8** and **9** from protonolysis of **4**.

Single-crystal X-ray diffraction have been applied to establish the structural characteristics of complexes **8** and **9**. ORTEP diagrams of both iron complexes are displayed in Figure 3.1 while Table 3.1 lists selected bond lengths and angles. The bond angle measurements of both metal complexes establish that the geometry at each iron center is pseudo-octahedral. Intraligand bond distances within each [ONO] and (cat-Cl$_4$) ligand scaffolds are used to determine the ligand oxidation states. For both complexes, electron delocalization within the [ONO] ligand influences the C(2)–O(1) and C(16)–O(2) bond lengths to lie between 1.36 Å and 1.21 Å, which are the corresponding C(aryl)–O single and C(sp^2)–O double bond lengths.[11] Such C−O bond distances are also observed in other M[ONO^q]$_2$ (M = Ni, Zn, Pb)[12, 13] and [ONO^q]M (M = Ta,[4] Al[14]) complexes. The C(16)−C(17) and C(19)−C(20) bond lengths of 1.34 Ǻ and 1.35 Ǻ, respectively, are shorter than the bond lengths of the other four carbon−carbon bonds within the six-membered ring of the [ONO] backbone for both **8** and **9**. The pattern of two short and four long C−C bonds is characteristic of the tridentate ligand adopting the [ONO^q]$^{1-}$ form.[4,12,13,14]

The (cat-Cl$_4$) moiety also has three accessible oxidation states: tetrachlorocatecholate (2−), tetrachlorosemiquinonate (1−), and tetrachloroquinone (neutral).[15] For both **8** and **9**, only small variations are observed in the six-membered ring, in accordance with electronic delocalization and aromaticity.[11] The C(29)–O(3) and C(34)–O(4) bond lengths for both iron complexes are in the range of 1.32–1.35 Å, consistent with C(aryl)–O single bond attributes.[11] Diagnostic examinations of these bond lengths establish that the bidentate ligand is in the dianionic tetrachlorocatecholate form. These catecholate carbon–oxygen bond lengths are also observed in other catecholato iron complexes.[16] Thus, coordination of the [ONO^q]$^{1-}$ and (cat-Cl$_4$)$^{2-}$ ligands indicate iron(III) centers for **8** and **9**.

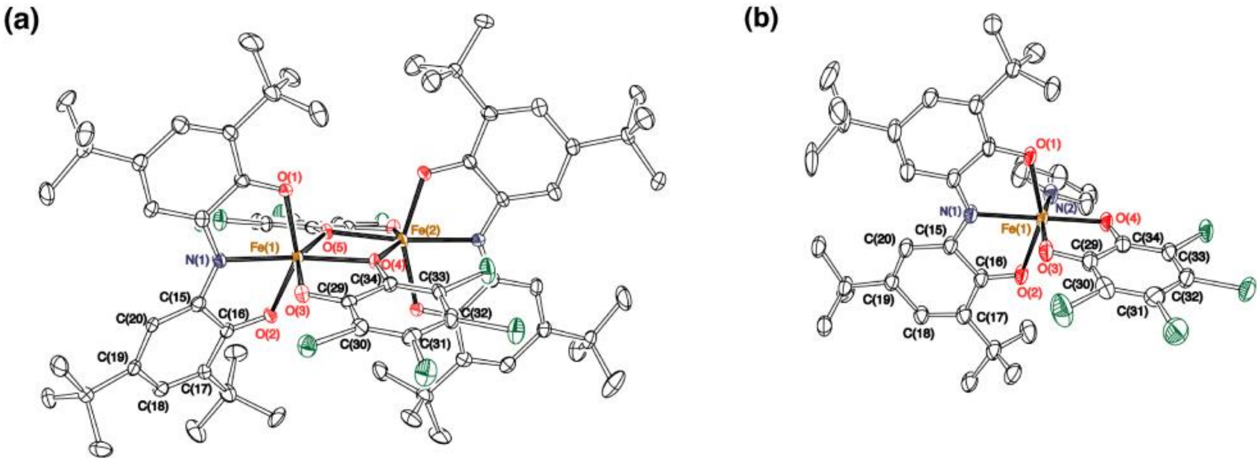

Figure 3.1 Crystal structure of **8** (*a*) and **9** (*b*). Thermal ellipsoids are shown at 50% probability. Hydrogen atoms and solvent molecules have been omitted for clarity.

Table 3.1. Selected bond lengths (Å) and bond angles (°) of **8** and **9**.

Bond	**8**	**9**
C(16)–O(2)	1.284(3)	1.269(4)
C(2)–O(1)	1.282(3)	1.285(4)
C(15)–N(1)	1.341(3)	1.332(5)
C(15)–C(16)	1.458(4)	1.463(6)
C(16)–C(17)	1.447(4)	1.453(6)
C(17)–C(18)	1.360(4)	1.360(5)

C(18)–C(19)	1.442(4)	1.433(6)
C(19)–C(20)	1.355(4)	1.349(6)
C(15)–C(20)	1.421(3)	1.443(6)
C(29)–C(30)	1.392(3)	1.381(7)
C(30)–C(31)	1.398(3)	1.410(7)
C(31)–C(32)	1.379(4)	1.380(5)
C(32)–C(33)	1.397(3)	1.385(7)
C(33)–C(34)	1.378(3)	1.385(6)
C(29)–C(34)	1.413(4)	1.415(5)
C(29)–O(3)	1.318(3)	1.329(6)
C(34)–O(4)	1.353(3)	1.329(5)
Fe(1)–N(1)	2.156(2)	2.157(3)
Fe(1)–N(2)	–	2.163(3)
Fe(1)–O(1)	1.987(2)	2.006(3)
Fe(1)–O(2)	2.023(2)	2.064(3)
Fe(1)–O(3)	1.950(2)	1.967(3)
Fe(1)–O(4)	2.091(2)	1.931(3)
Fe(1)–O(5)	2.018(2)	–
O(3)–Fe(1)–N(2)	–	166.6(1)
O(1)–Fe(1)–O(2)	148.21(7)	150.8(1)
O(4)–Fe(1)–N(1)	157.65(7)	177.0(1)
O(3)–Fe(1)–O(5)	150.35(7)	–
O(4)–Fe(1)–O(5)	72.96(6)	–
Fe(1)–O(4)–Fe(2)	106.46(7)	–

The electronic properties of complex **9** are further probed using EPR spectroscopy. As shown in Figure 3.2, the EPR spectrum of the mononuclear complex features a rhombic signal with g values of 2.00, 1.95, and 1.88. This is consistent with the metal center of **9** adopting a low-spin iron(III) configuration, engendering an overall $S = \frac{1}{2}$ system.[17]

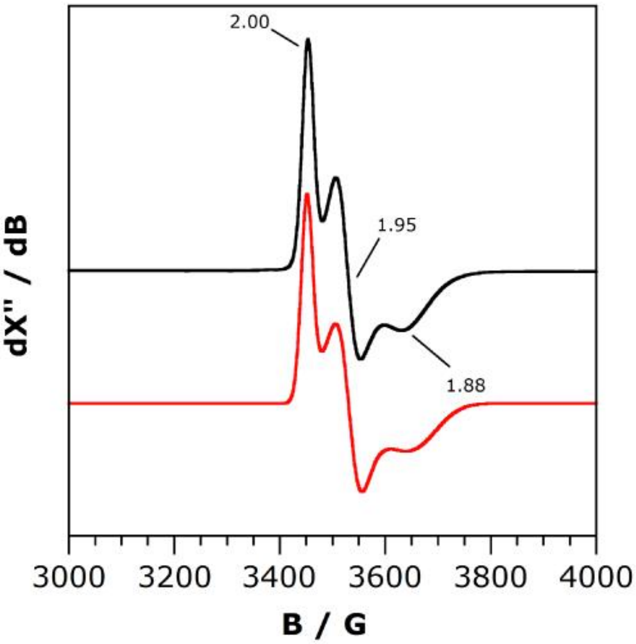

Figure 3.2. X-band EPR spectrum of [ONO^q]Fe(cat-Cl$_4$)(py) (**9**; black) and simulation (red). Experimental conditions: $B_1 \perp B_0$; solvent, toluene; temperature, 4 K.

3.2.2 Metathesis Reactions of the [ONO^q]FeX$_2$ Platform

To explore the reactivity of the [ONO^q]Fe^{III}X$_2$ platform, metathesis reactions were performed with [ONO^q]FeCl$_2$ (**3a**) and [ONO^q]Fe[N(SiMe$_3$)$_2$]$_2$ (**4**), as summarized in Scheme 3.3.[10] Treatment of **4** with two equivalents of *tert*-butylthiol in neat pyridine produced a green solution containing [ONO^{cat}]Fe(py)$_3$ (**7**) and di-*tert*-butyl disulfide in 81% yield. Complex **7** could be prepared by two other methods: either by hydrogenation of **4** with one equivalent of diphenylhydrazine (and concomitant formation of azobenzene in 94% yield), or by reduction of **3a** with two equivalents of KC$_8$. These reduction reactions showcase the ability of the [ONO^q]Fe^{III}X$_2$ platform to undergo ligand-based two-electron redox reactivity.

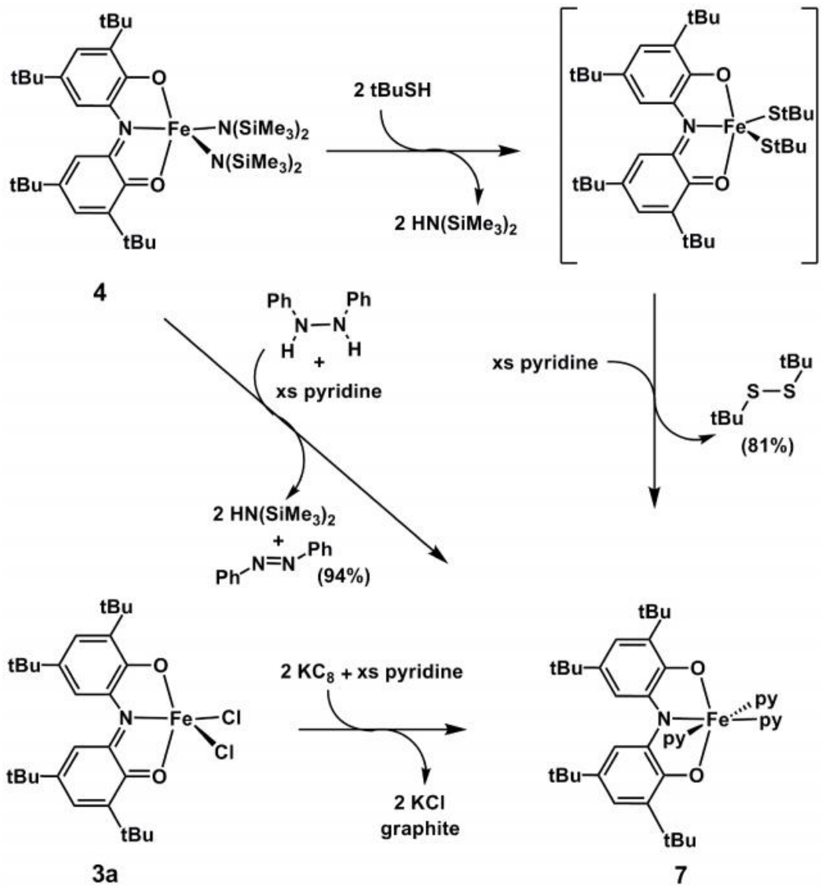

Scheme 3.3. Reductions of **3a** and **4** in the presence of excess pyridine to produce **7**.

In the absence of pyridine, treatment of **3a** and **4** using the same reductants described in Scheme 3.3 led to elimination of the corresponding byproducts and isolation of a diiron complex (Scheme 3.4). The structure of this bimetallic complex, formed in sub-stoichiometric quantities, was established to be $Fe_2[ONO]_3$ by single-crystal X-ray crystallography and features five- and six-coordinate iron centers. The formation of this bimetallic complex through multiple reaction pathways elicited our interest in developing a rational method for preparing this unique diiron complex. Detailed synthesis and characterization of $Fe_2[ONO]_3$ will be discussed in Chapter 4.

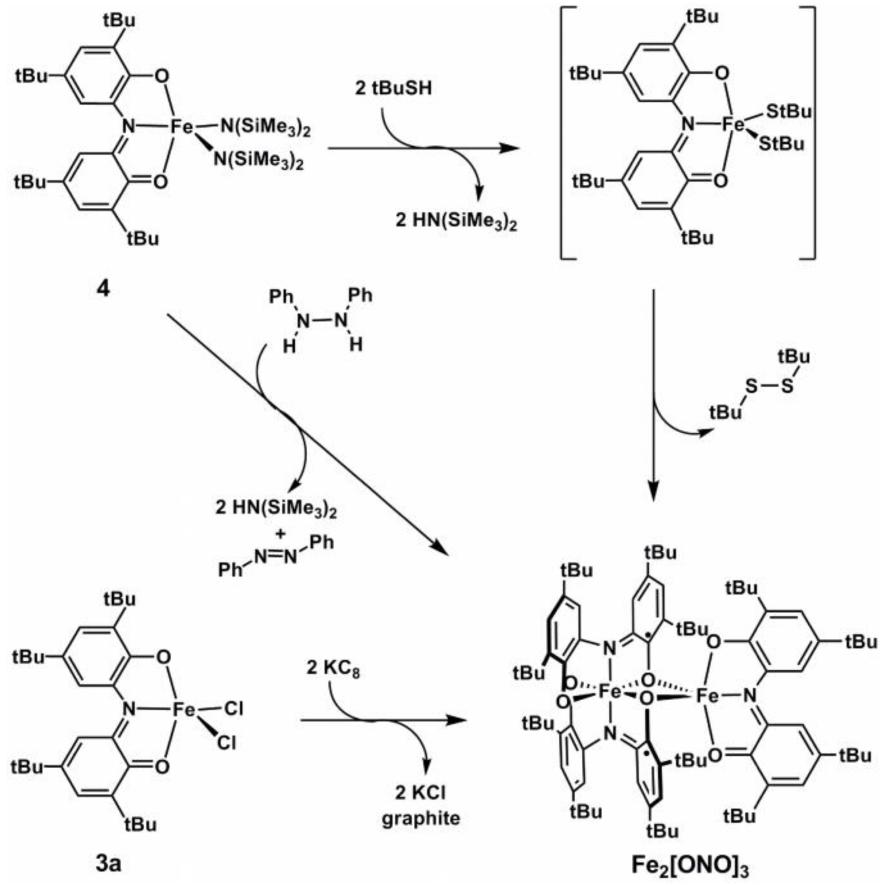

Scheme 3.4. Reductions of **3a** and **4** in the absence of pyridine to produce the diiron complex $Fe_2[ONO]_3$.

3.2.3 Synthesis and Characterization of the Dimer $\{[ONO^{cat}]Fe(py)\}_2$

When reductions of **3a** and **4** were carried out using excess pyridine in non-pyridine solvents, dark purple solutions were generated that contained a new dimer alongside complex **7**. In the presence of 10 equivalents of pyridine, addition of two equivalents of *tert*-butylthiol in diethyl ether solutions of **4** resulted in formation of the disulfide while reduction of **3a** with two equivalents of KC_8 in THF eliminated KCl salts. Through the diffusion of acetonitrile into THF solutions containing the iron product, dark microcrystalline materials were obtained and established through X-ray crystallography to be complex **7**. In contrast, treatment of **4** in benzene with one equivalent of diphenylhydrazine and 100 equivalents of pyridine led to formation of the azobenzene byproduct and isolation of a diiron compound, $\{[ONO^{cat}]Fe(py)\}_2$ (**10**). Dark purple crystals of **10** suitable for X-ray crystallography were obtained via diffusion of acetonitrile into THF solutions containing the dimer at −35 °C. As illustrated through the ORTEP diagram of **10** in Figure 3.3, **10** is a dimer in which the two iron centers are bridged by the nitrogen donors of the [ONO] ligand backbone.

Through X-ray crystallography, the structural properties of **10** are investigated. The geometric parameter ² = (J ~) / 60 (² = 1 for perfectly trigonal bipyramid; 0 for perfectly square pyramid) is used to describe the geometry at each iron center of **10** based on the bond angle measurements provided in Table 3.2.[18] Given that ~ = ∠O(1)–Fe(1)–O(2); = ∠N(2)–Fe(1)–N(1), ² = 0.53, an indication that the geometry at each metal center lie in between square pyramid and trigonal bipyramid. The small variations in the carbon–carbon bond lengths of the [ONO] ligand six-membered ring are characteristic of electronic delocalization within an aromatic system.[11] The C(1)–N(1) and C(15)–N(1) bond lengths of 1.44 Å lie within the C(aryl)–N(sp^2) and C(sp^2)–N(sp^2) single bond lengths, suggestive of C–N single bond character.[11] Finally, the C(2)–O(2) and C(16)–O(1) bond lengths of 1.339 Å are consistent with C(aryl)–O single bonds.[11] These bond metrical patterns are observed in other $[\mathrm{ONO^{cat}}]$M (M = Ta,[4] Nb,[19] Rh[20]) complexes, indicating that complex **10** has two $[\mathrm{ONO^{cat}}]^{3-}$ ligands each coordinated to an iron(III) center.

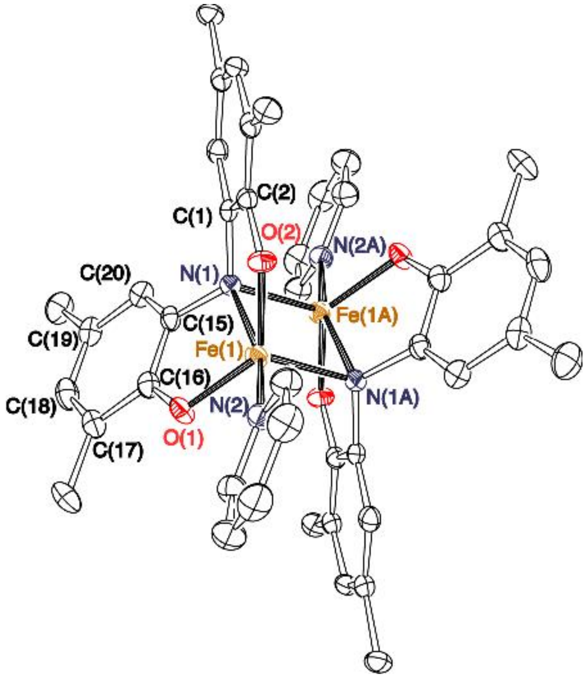

Figure 3.3. ORTEP diagram of complex **10**. Hydrogen atoms and *tert*-butyl groups have been omitted for clarity. Thermal ellipsoids are shown at 50% probability.

Table 3.2. Selected bond lengths (Ǻ) and angles (°) of **10**.

Bond	Length	Bond	Angle
C(2)–O(1)	1.339(3)	O(1)–Fe(1)–O(2)	131.31(7)
C(16)–O(2)	1.339(3)	N(1)–Fe(1)–N(2)	162.89(7)
C(1)–N(1)	1.440(3)	Fe(1)–N(1)–Fe(1A)	88.02(7)
C(15)–N(1)	1.440(2)	N(1)–Fe(1)–N(1A)	91.98(7)
C(15)–C(16)	1.410(3)		
C(16)–C(17)	1.414(3)		
C(17)–C(18)	1.381(3)		
C(18)–C(19)	1.395(4)		
C(19)–C(20)	1.389(3)		
C(15)–C(20)	1.395(3)		
Fe(1)–O(1)	1.879(1)		
Fe(1)–O(2)	1.873(1)		
Fe(1)–N(1)	2.163(2)		
Fe(1)–N(2)	2.134(2)		
Fe(1)–N(1A)	1.992(2)		
Fe(1)–Fe(1A)	2.8889(5)		

The ability to isolate {[ONO^{cat}]Fe(py)}$_2$ (**10**) and [ONO^{cat}]Fe(py)$_3$ (**7**) through similar reaction pathways suggested that both complexes exist concurrently in solution. As described in chapter 2, pure crystalline solids of **7** were obtained through diffusion of acetonitrile into neat pyridine solutions containing the monomer. The EPR and electronic spectra were collected in pyridine in order to obtain data of neat compound **7**. When green crystalline materials of **7** were dissolved in non-pyridine solvents, the UV-vis-NIR spectrum of the resulting purple solution displayed features consistent with those observed in the electronic spectrum of solutions containing **10**. Likewise, when dark purple solids containing the dimer were dissolved in pyridine to produce a dark green solution, its UV-vis-NIR spectrum featured absorptions characteristic of the electronic spectrum of **7**. These results suggest that in non-pyridine solvents, two coodinatively-labile pyridine ligands of **7** can dissociate and the resulting {[ONO^{cat}]Fe(py)} fragments will dimerize to form **10** (Scheme 3.5).

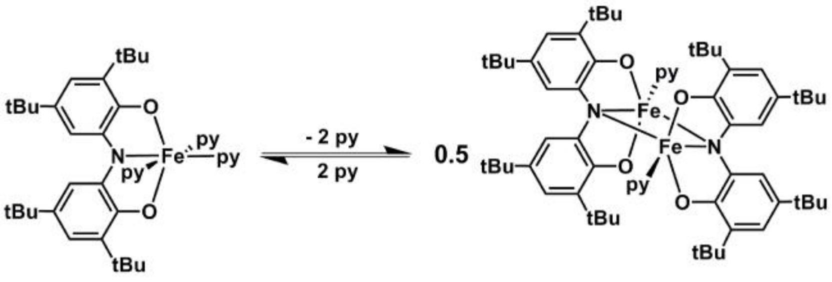

7 **10**

Scheme 3.5. Equilibrium between **7** and **10** in non-pyridine solvents.

To further support this conjecture, EPR spectroscopic experiments were performed. When green crystalline materials of **7** were dissolved in non-pyridine solvents to produce a dark purple mixture, silent EPR signals were observed at room temperature and at 77 K. The same observations were made when the EPR spectrum of the dark purple solids containing **10** were collected in THF or toluene solutions. Upon removing the solvent under vacuum, the dark purple residue was dissolved in pyridine, and the EPR spectrum of the resulting dark green mixture revealed resonances consistent with the $S = \frac{5}{2}$, iron(III) monomer **7**.[10] Thus, in non-pyridine solutions, the monomer and dimer exist in equilibrium with one another.

3.2.4 Reactivity of [ONO$^{\text{cat}}$]Fe(py)$_3$

Coordination of labile pyridine ligands to the iron(III) center of [ONO$^{\text{cat}}$]Fe(py)$_3$ (**7**) indicated that ligand substitution would be an appropriate method for installing new ligands to the iron coordination sphere. Addition of ~-diimine ligands to solutions of **7** did not result in isolation of new [ONO$^{\text{cat}}$]FeL$_n$ complexes and free diimine substrates were observed. The hardness of the iron(III) center suggested that coordination of the soft diimine ligands was disfavored. On the other hand, reaction of **7** with one equivalent of diphenylphosphino ethane (dppe), a strong-field ligand, produced [ONO$^{\text{cat}}$]Fe(dppe) (**6**) in 90% yield (Scheme 3.6).

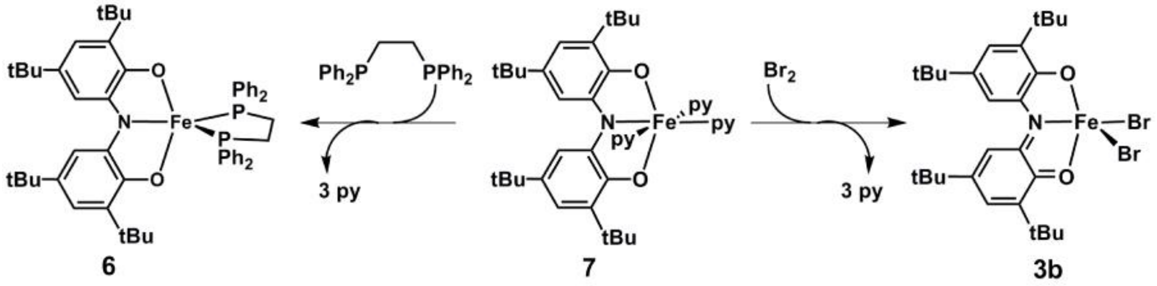

Scheme 3.6. Ligand substitution and oxidative-addition reactivity of **7**.

Ligand-enabled redox reactivity of **7** was investigated through the use of dihalogens as oxidants. Since halogen-containing compounds have mass spectrometric patterns based on the relative peak abundances (molecular ion [M], [M+2], [M+4], and so on) unique to the type and number of halogens present, electrospray ionization mass spectrometry (ESI/MS) was employed for initial confirmation of the successful preparation of iron–halide complexes (Figure 3.4).[21] As described in Scheme 3.6, addition of pentane solutions of bromine to toluene solutions of **7** led to isolation of dark red crystalline solids in 62% yield. The ESI/MS chromatogram of this material displayed the following m/z peaks: 636.09 ([M]; 54%), 638.09 ([M+2]; 100%), and 640.09 ([M+4]; 42%), consistent with the isotope patterns of the iron dibromide complex, $[ONO^q]FeBr_2$ (**3b**). To further verify the identity of this product, EPR spectroscopy was utilized and the spectrum revealed resonances characteristic of the $S = \frac{5}{2}$ system, complex **3b** (see chapter 2). Through the additions of $PhICl_2$ and iodine to **7**, the syntheses of the corresponding $[ONO^q]FeCl_2$ (**3a**) and $[ONO^q]FeI_2$ were also pursued. While the ESI/MS chromatogram of the resulting crude products indicated that both iron dihalide complexes were formed (Figure 3.4), clean isolation of either compounds could not be achieved. Because $PhICl_2$ is fairly unstable and decomposes slowly over time,[22] treatment of **7** with the likely contaminated starting material resulted in the formation of product mixtures rather than quantitative yields of **3a**. The high solubility of the putatative $[ONO^q]FeI_2$ in organic solvents also led to difficulties in purification and isolation of clean crystalline material. Nonetheless, the distinctive peak patterns observed in the ESI/MS spectrum of all three $[ONO^q]FeX_2$ complexes demonstrate the ability of **7** to undergo ligand-based two-electron oxidation.

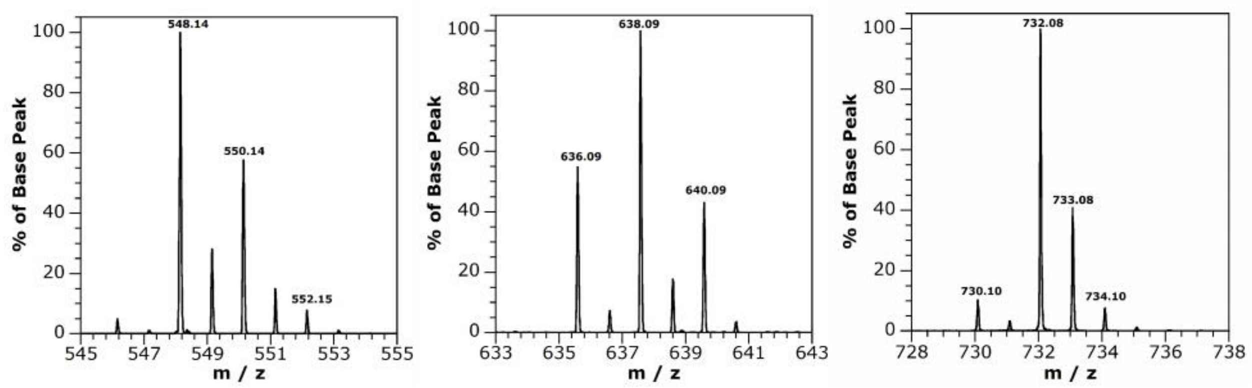

Figure 3.4. ESI/MS chromatograms of $[ONO^q]FeCl_2$ (**3a**; left), $[ONO^q]FeBr_2$ (**3b**; center), $[ONO^q]FeI_2$ (right).

The reversibility of the ligand-based two-electron oxidation state changes of the [ONO]Fe platform prompted our interest in probing the ability of **7** to catalyze nitrene-transfer reactivity using organoazides (RN_3) as the imido precursor. We surmised that treatment of **7** with

(RN_3) should lead to formation of the transient iron nitrene complex, which could possibly dimerize to form diiron compounds with bridging imidos. This hypothesis was tested through the reaction of **7** with one equivalent of *tert*-butyl azide in C_6D_6 at ambient temperature or 70 °C (Scheme 3.7). However, by monitoring the experiment through ^{1}H NMR, neither consumption of the azide nor formation of the diamagnetic {[ONO^q]Fe(«-N*t*Bu)}$_2$ (**5**) were observed. Furthermore, under analogous conditions, addition of excess pyridine to **5** did not result in elimination of the di-*tert*-butyl diazene to form **7**. These results indicate that azido ligands do not have strong enough driving forces to displace the pyridines bound to the iron center of **7**.

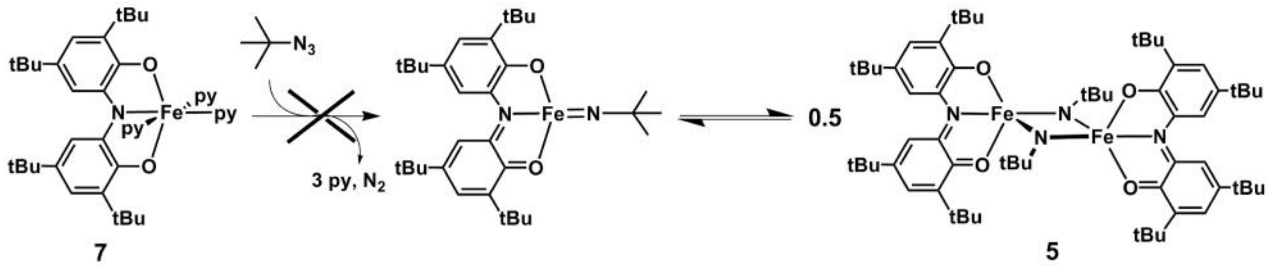

Scheme 3.7. Proposed mechanism to form **5** through treatment of **7** with *tert*-butyl azide.

3.3 Discussion

3.3.1 Reactivity Patterns of Iron Complexes Supported by [ONO] Ligand

The extrusion of di-*tert*-butyl disulfide through treatment of [ONO^q]Fe[N(SiMe$_3$)$_2$]$_2$ (**2**) with two equivalents of *tert*-butylthiol gives rise to mechanistic questions of the formation of new sulfur–sulfur bonds. As illustrated in Scheme 3.3, we hypothesize that this reaction proceeds through formation of the transient [ONO^q]Fe^{III}(S*t*Bu)$_2$ complex followed by reductive elimination of the two sulfide ligands to form the disulfide. The resulting {[ONO^{cat}]Fe} fragment is then captured by pyridine ligands to form [ONO^{cat}]Fe(py)$_3$ (**7**). Since elimination of a disulfide from an iron complex is rare,[23] our studies show that this unusual result is achievable through the cooperative redox reactivity of the metal and redox-active ligand.

Metallation of the [ONO] ligand to the iron(III) center promotes two-electron reactivity at the metal coordination sphere while avoiding formation of potentially unstable iron intermediates. Metathesis reactions of the $[ONO^{q}]Fe^{III}X_2$ complexes lead to two-electron reduction of the redox-active ligand, circumventing the Fe(I) intermediate which is not feasible.[24, 25] Oxidative addition of dihalogens to **7** results in the two-electron oxidation of the [ONO] moiety, bypassing the formation of unstable Fe(V) species.[26] When the reactions were carried out with sub-stoichiometric quantities of reductants or oxidants, there was no evidence for formation of the one-electron reduced or one-electron oxidized iron complexes. The reactivity pathways of the [ONO]Fe platform lend support to the argument that coordination of the redox-active [ONO] ligand to iron strongly prefers the +3 metal oxidation state.

Towards designing metal complexes capable of facilitating group-transfer reactivity, the coordination environment of the metal center must be taken into consideration. Chelation of the fully-reduced $[ONO^{cat}]^{3-}$ to the iron(III) center of **7** suggests that the complex is an appropriate pre-catalyst for this type of reactivity. While the labile pyridine ligands should be displaceable through the use of relevant substrates, this may be difficult to be achieved by many common organic precursors used in group-transfer catalysis. Coordinatively-unsaturated iron complexes have been shown to mediate nitrene-transfer reactions.[27] As such, coordinatively-unsaturated iron complexes containing the $[ONO^{cat}]^{3-}$, such as $[ONO^{cat}]$Fe(dppe) (**6**), should be more suitable candidates for this type of catalytic organic transformations.

3.4 Summary and Conclusion

Coordination of the redox-active [ONO] ligand to iron provides a new platform for multi-electron reactivity. This concept is showcased through the ligand-enabled redox chemistry of the [ONO]Fe platform. Although conventional reductive elimination chemistry involves two-electron reduction at the metal center, the cooperative redox reactivity of the metal and ligand can facilitate formation of new bonds.[5b] Likewise, this type of metal-ligand cooperativity also mediates oxidative addition processes that circumvents two-electron oxidation at the metal center.[5a] Hence, upon coordination to the iron center, the [ONO] ligand is capable of providing the necessary electron equivalents in order to facilitate bond-activation processes.

3.5 Experimental

General Procedures. All compounds and reactions reported below were carried out under air and moisture-free conditions using standard glovebox or Schlenk techniques. Solvents were sparged with argon and then deoxygenated and dried by passage through Q5 and activated alumina columns, respectively. To test for effective oxygen and water removal, solvents were treated with a few drops of a purple solution of sodium benzophenone ketyl in THF. The C_6D_6 NMR solvent was dried over sodium-potassium amalgam benzophenone ketyl for two days, followed by trap-to-trap vacuum distillation and several freeze-pump-thaw cycles.

The compounds potassium graphite KC_8,[28] $[ONO^{cat}]H_3$,[4, 29] $K[ONO^q]$,[20] and 1,2-bis(4-methylphenyl)diazene[30] were synthesized according to published procedures. The synthetic procedures for $[ONO^qFeCl_2$ (**3a**) and $[ONO^q]Fe[N(SiMe_3)_2]_2$ (**4**) have been reported in chapter 2 as well as in the literature.[10] Diphenylhydrazine and azobenzene were purchased from Alfa Aesar and sublimed before use. The pyridine (Macron), *tert*-butylthiol (Alfa Aesar), diisopropyl disulfide (Acros), and di-*tert*-butyl disulfide (Acros) were dried over activated 4 Å molecular sieves (Fisher Scientific) overnight and then distilled under reduced pressure into a Straus flask and degassed through several freeze-pump-thaw cycles. Tetrachlorocatechol was purchased from Sigma Aldrich and used without further purification. Potassium hydride (Alfa Aesar) was washed in pentane to remove the oil prior to usage.

Physical Measurements. UV-vis-NIR spectra were recorded on toluene or pyridine solutions using a Perkin–Elmer Lambda 800 Spectrometer. Electrospray ionization mass spectrometry (ESI/MS) and gas chromatography mass spectrometry (GC/MS) were performed at the Mass Spectrometry Facility at University of California, Irvine. X-band EPR spectra ($B1 \perp B0$) were collected using Bruker EMX spectrometer equipped with ER041XG microwave bridge. Elemental analysis experiments have been performed on all new compounds, and the results of those that fall in the expected mass ranges are reported.

Crystallographic Methods. X-ray diffraction data were collected on crystals mounted on glass fibers using a Bruker CCD platform diffractometer equipped with a CCD detector. Measurements were carried out using Mo K_α (λ = 0.71073 Å) radiation, which was wavelength selected with a single-crystal graphite monochromator. A full sphere of data was collected for each crystal structure. The APEX2 program package was used to determine unit-cell parameters and to collect data.[31] The raw frame data were processed using SAINT[32] and SADABS[33] to yield the reflection data files. Subsequent calculations were carried out using the SHELXTL[34] program suite. Structures were solved by direct methods and refined on F^2 by full-matrix least-squares techniques to convergence. Analytical scattering factors for neutral atoms were used throughout the analyses. Hydrogen atoms, though visible in the difference Fourier map, were generated at calculated positions and their positions refined using the riding model. ORTEP diagrams were generated using ORTEP-3 for Windows[35] and all thermal ellipsoids are drawn at the 50% probability level.

Table 3.3. X-ray diffraction data-collection and refinement parameters for complexes **8**, **9**, and **10**.

	8•1.5 (C_5H_{12})	**9**•($C_4H_{10}O$)	**10**
Empirical formula	$C_{68}H_{72}Cl_8Fe_2N_2O_8$• 1.5 ($C_5H_{12}$)	$C_{39}H_{45}Cl_4FeN_2O_4$• ($C_4H_{10}O$)	$C_{66}H_{90}Fe_2N_4O_4$
Formula weight	1556.86	877.54	1115.12

Crystal system	Triclinic	Monoclinic	Monoclinic
Space group	$P\bar{1}$	$P2_1/n$	$P2_1/c$
T	143(2) K	88(2) K	143(2) K
a	14.8709(8) Å	12.6068(11) Å	14.1943(10) Å
b	15.7470(8) Å	24.431(2) Å	14.2798(10) Å
c	17.9214(10) Å	16.6177(14) Å	17.1104(13) Å
~	94.0663(7)°	90°	90°
	111.4278(7)°	111.8027(9)°	113.9953(9)°
¥	95.5142(7)°	90°	90°
V	3863.0(4) Å^3	4752.1(7) Å^3	3168.4(4) Å^3
Z	2	4	2
Reflections collected	42365	46245	33737
data/restraints/parameter	15780 / 0 / 893	8703 / 11 / 498	6485 / 0 / 355
R1 [$I > 2\sigma(I)$]^a	0.0401	0.0610	0.0413
wR2 (all data)^a	0.0999	0.1709	0.1125
GOF^a	1.074	1.019	1.014

^{a} R1 = $\Sigma||F_o| - |F_c||/\Sigma|F_o|$; wR2 = $[\Sigma[w(F_o^2 - F_c^2)^2]/\Sigma[w(F_o^2)^2]]^{1/2}$; GOF = $[\Sigma w(|F_o| - |F_c|)^2/(n - m)]^{1/2}$

Synthesis of {[ONO^q]Fe(cat-Cl$_4$)}$_2$ (8). To the frozen 10 mL benzene solution containing 210 mg of **4** (0.263 mmol, 1 equiv.), 65.9 mg of tetrachlorocatehol (0.266 mmol, 1 equiv.) was added. Upon thawing at ambient temperature, the dark brown solution became dark green as it continued to stir overnight (> 12 hours). Removal of the solvent revealed dark green residue which was subsequently co-evaporated with pentane (2 x 10 mL). Yield: 140 mg (73%).

Synthesis of [ONO^q]Fe(cat-Cl$_4$)(py) (9). To the 10 mL cold dark brown benzene solution containing 211 mg of **4** (0.264 mmol, 1 equiv.), 65.5 mg of tetrachlorocatehol (0.264 mmol, 1 equiv.) was added. The solution warmed to ambient temperature as the color changed to dark green. Upon stirring overnight (>12 hours), the solvent was removed under pressure to yield dark green residue. After dissolving the residue in diethyl ether, 69.5 μL of pyridine (0.861 mmol, 3.26 equiv.) was added and the mixture stirred at room temperature for 30 minutes, after which the dark green solution was cooled overnight at 238 K to afford dark green solids of **9** in 63% yield (134 mg). UV-vis-NIR (Toluene) λ_{max}/nm (ε/ M^{-1}cm^{-1}): 310 (5,100), 458 (5,100), 556 (3,000), 828 (4,500).

Synthesis of {[ONO^{cat}]Fe(py)}$_2$ (10). To the 10 mL cold benzene solution containing 79.8 mg of **4** (1.00 mmol, 1 equiv.) and 805 μL of pyridine (100 mmol, 100 equiv.), 18.5 mg of 1,2-diphenylhydrazine (1.00 mmol, 1 equiv.) was added. The dark brown-green solution was stirred overnight (>12 hours), after which the solvent was removed under vacuum. The dark residue was dissolved in THF to yield dark purple solution. Diffusion of acetonitrile into the concentrated THF solution at 238 K overnight afforded dark microcrystalline solids. Yield: 361 mg.

Synthesis of [ONO^{q}]FeBr$_2$ (3b) from [ONO^{cat}]Fe(py)$_3$ (7). A dark purple toluene solution containing 153 mg of **7** (0.214 mmol, 1 equiv.) and a red pentane solution of 11 μL of bromine (0.215 mmol, 1 equiv.) were cooled at 77 K. As the dark purple solution stirred at ambient temperature, solutions of bromine were added drop-wise. After stirring for 6.5 hours, the resulting dark green mixture was placed under reduced pressure to remove the volatiles and subsequently co-evaporated using toluene (3 x 10 mL) until the solution was no longer green. Extraction of the dark residue using toluene produced dark red-brown solutions which were then concentrated to half volume. Diffusion of pentane to the toluene solution led to isolation of dark red-brown crystalline material. Yield: 85.2 mg (62%). UV-vis-NIR (THF) λ_{max}/nm (ε/ M^{-1}cm^{-1}): 226 (14,400), 438 (11,700), 664 (4,200), 856 (7,600). MS(ESI^{-}) m/z: 636.09 (M+), 638.09 (M+2), 640.09 (M+4).

Analytical Quantification Procedures

All reactions were monitored via gas chromatography mass spectrometry (GC/MS). Calibration curves were generated using benzene solutions of 1,2-bis(4-methylphenyl)diazene (0.00150 mM) and di-isopropyldisulfide (0.0314 mM) as internal standards along with solutions of azobenzene (0.000500–0.00250 mM) and di-*tert*-butyl disulfide (0.000414–0.00207 mM), respectively, as the analytes. These samples were then injected into the GC/MS instrument. Ratios of area of analyte: area of internal standards were plotted against known concentrations of the analyte.

Quantification of di-*tert*-butyldisulfide

To a thawing solution of **4** (0.251–0.253 mmol, 1 equiv.) in 15 mL of benzene and 2.0 mL of pyridine (25 mmol, 100 equiv), 57 μL of *tert*-butylthiol (0.51 mmol, 2 equiv.) was added. The dark brown-green solution was stirred at ambient temperature for 16 hours, after which a 1 mL aliquot of the reaction mixture was taken to prepare a 100 mL benzene solution. From this stock solution, three 10 mL benzene solutions of the GC/MS samples were prepared, each containing 1 mL aliquot of the stock solution and known amounts of the internal standard. These steps were repeated two more times, generating a total of nine samples that were then injected into the GC/MS instrument. The average yield of the di-*tert*-butyl disulfide was determined to be 81% based on initial quantities of **4**.

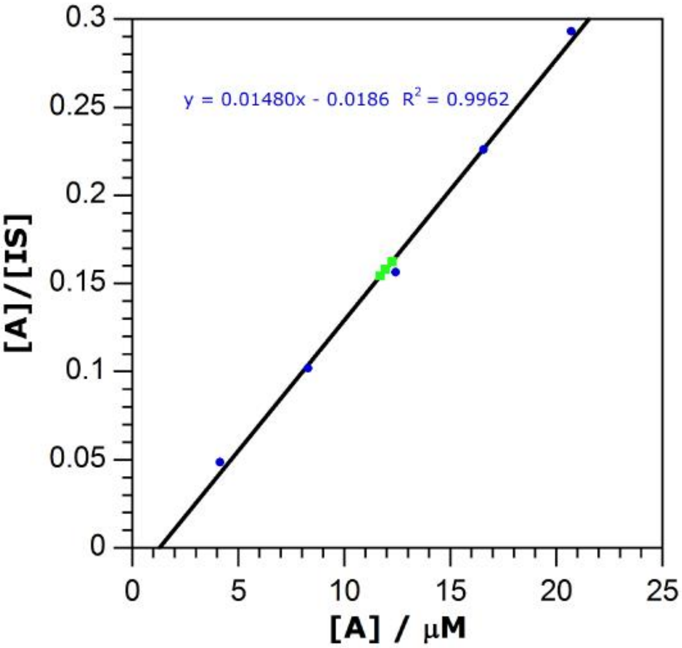

Figure 3.5. Plot of calibration curve (blue) and quantification of di-*tert*-butyl disulfide (green). [A]/[IS] describes the ratio of analyte peak area (A): internal standard peak area (IS). [A] corresponds to the concentration of di-*tert*-butyl disulfide.

Quantification of azobenzene

To a thawing solution of **4** (0.251 mmol, 1 equiv.) in 15 mL of benzene and 2.0 mL of pyridine (25 mmol, 100 equiv), 12 mg of diphenylhydrazine (0.25 mmol, 1 equiv.) was added. The dark brown-green solution was stirred at ambient temperature for 16 hours, after which a 1 mL aliquot of the reaction mixture was taken to prepare a 100 mL benzene solution. From this stock solution, three 10 mL benzene solutions of the GC/MS samples were prepared, each containing 1 mL aliquot of the stock solution and known amounts of the 1,2-bis(4-methylphenyl)diazene internal standard. These steps were repeated two more times, generating a total of nine samples that were then injected into the GC/MS instrument. The average yield of the azobenzene was determined to be 94% based on initial quantities of **4**.

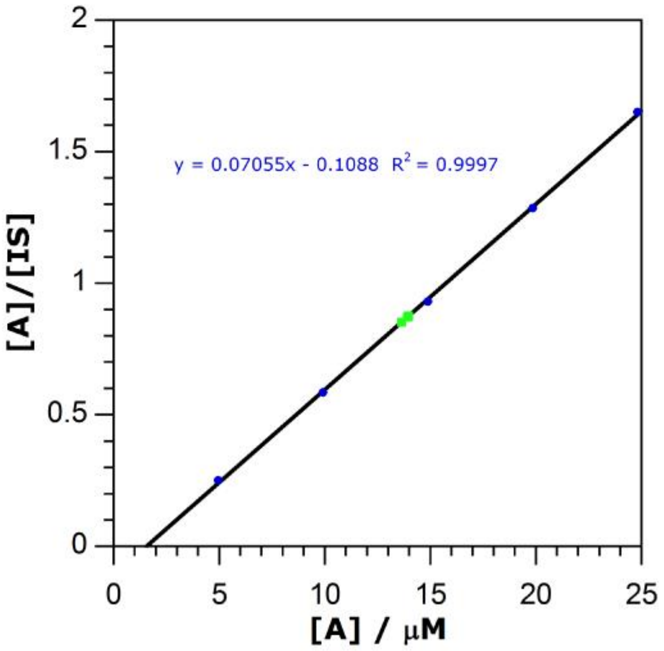

Figure 3.6. Plot of calibration curve (blue) and quantification of azobenzene (green). [A]/[IS] describes the ratio of analyte peak area (A): internal standard peak area (IS). [A] corresponds to the concentration of azobenzene.

3.6 References

[1] (a) Plietker, B., Ed. *Iron Catalysis in Organic Chemistry*; Wiley-VCH: Weinheim, 2008. (b) Plietker, B., Ed. *Iron Catalysis*; Springer-Verlag: Berlin Heidelberg, 2011.

[2] (a) Praneeth, V. K. K.; Ringenberg, M. R.; Ward, T. R. *Angew. Chem. Int. Ed.* **2012**, *51*, 10228–10234. (b) Crabtree, R. H.; Luca, O. R. *Chem. Soc. Rev.* **2013**, *42*, 1440–1459.

[3] Chirik, P. J.; Wieghardt, K. *Science* **2010**, *327*, 794–795.

[4] Zarkesh, R. A.; Ziller, J. W.; Heyduk, A. F. *Angew. Chem. Int. Ed.* **2008**, *47*, 4715–4718.

[5] (a) Blackmore, K. J.; Ziller, J. W.; Heyduk, A. F. *Inorg. Chem.* **2005**, *44*, 5559–5561. (b) Haneline, M. R.; Heyduk, A. F. *J. Am. Chem. Soc.* **2006**, *128*, 8410–8411. (c) Blackmore, K. J.; Lal, N.; Ziller, J. W.; Heyduk, A. F. *J. Am. Chem. Soc.* **2008**, *130*, 2728–2729.

[6] (a) Heyduk, A. F.; Zarkesh, R. A.; Nguyen, A. I. *Inorg. Chem.* **2011**, *50*, 9849–9863. (b) Munhá, R. F.; Zarkesh, R. A.; Heyduk, A. F. *Dalton Trans.* **2013**, *42*, 3751–3766.

[7] Nguyen, A. I.; Zarkesh, R. A.; Lacy, D. C.; Thorson, M. K.; Heyduk, A. F. *Chem. Sci.* **2011**, *2*, 166–9.

[8] (a) Bart, S. C.; Lobkovsky, E.; Bill, E.; Chirik, P. J. *J. Am. Chem. Soc.* **2006**, *128*, 5302–5303. (b) Bart, S. C.; Chłopek, K.; Bill, E.; Bouwkamp, M. W.; Lobkovsky, E.; Neese, F.; Wieghardt, K.; Chirik, P. J. *J. Am. Chem. Soc.* **2006**, *128*, 13901–13912. (c) Bart, S. C.; Lobkovsky, E.; Bill, E.; Wieghardt, K.; Chirik, P. J. *Inorg. Chem.* **2007**, *46*, 7055–7063. (d) Bart, S. C.;

Lobkovsky, E.; Chirik, P. J. *J. Am. Chem. Soc.* **2004**, *126*, 13794–13807. (e) Trovitch, R. J.; Lobkovsky, E.; Chirik, P. J. *Inorg. Chem.* **2006**, *45*, 7252–7260.

[9] (a) Thammavongsy, Z.; Seda, T.; Zakharov, L. N.; Kaminsky, W.; Gilbertson, J. D. *Inorg. Chem.* **2012**, *51*, 9168–9170. (b) Thammavongsy, Z.; LeDoux, M. E.; Breuhaus-Alvarez, A. G.; Seda, T.; Zakharov, L. N.; Gilbertson, J. D. *Eur. J. Inorg. Chem.* **2013**, *20*, 4008–4015.

[10] Wong, J. L.; Sánchez, R. H.; Logan, J. G.; Zarkesh, R. A.; Ziller, J. W.; Heyduk, A. F. *Chem. Sci.* **2013**, *4*, 1906–1910.

[11] Allen, F. H.; Kennard, O.; Watson, D. G. *J. Chem. Soc. Perkin Trans. II* **1987**, S1–S19.

[12] (a) Girgis, A. Y.; Balch, A. L. *Inorg. Chem.* **1975**, *14*, 2724–2727. (b) Simpson, C. L.; Boone, S. R.; Pierpont, C. G. *Inorg. Chem.* **1989**, *28*, 4379–4385.

[13] (a) Chauduri, P.; Hess, M.; Weyhermuller, T.; Wieghardt, K. *Inorg. Chem.* **1999**, *38*, 2781–2790. (b) McGarvey, B. R.; Ozarowski, A.; Tian, Z.; Tuck, D. G. *Can. J. Chem.* **1995**, *73*, 1213–1222. (c) Attia, A. S.; Conklin, B. J.; Lange, C. W.; Pierpont, C. G. *Inorg. Chem.* **1996**, *35*, 1033–1038.

[14] Szigethy, Géza; Heyduk, A. *Dalton Trans.* **2012**, *41*, 8144–8152.

[15] (a) Pierpont, C. G. *Coord. Chem. Rev.* **2001**, *221*, 415–433. (b) Zanello, P.; Corsini, M. *Coord. Chem. Rev.* **2006**, *250*, 2000–2022.

[16] (a) Cox, D. D.; Que, Jr., L. *J. Am. Chem. Soc.* **1988**, *110*, 8085–8092. (b) Bruijnincx, P. C. A.; Lutz, M.; Spek, A. L.; Hagen, W. R.; Weckhuysen, B. M.; van Koten, G.; Gebbink, R. J. M. K. *J. Am. Chem. Soc.* **2007**, *129*, 2275–2286. (c) Zirong, D.; Bhattacharya, S.; McCusker, J. K.; Hendrick, D. N.; Pierpont, C. G. *Inorg. Chem.* **1992**, *31*, 870–877. (d) Buchanan, R. M.; Kessel, S. L.; Downs, H. H.; Pierpont, C. G.; Hendrickson, D. N. *J. Am. Chem. Soc.* **1978**, *100*, 7894–7900.

[17] Que, Jr., L. *Physical Methods in Bioinorganic Chemistry*; University Science Books: Sausalito, CA, 1999; 134–185.

[18] Trans, D.; Addison, A. W.; Rao, T. N. *Dalton Trans.* **1984**, 1349–1356.

[19] Hananouchi, S. P. MS Thesis, University of California, Irvine, 2014.

[20] Szigethy, G.; Shaffer, D. W.; Heyduk, A. F. *Inorg. Chem.* **2012**, *51*, 12606–12618.

[21] Silversteine, R. M.; Webster, F. X.; Kiemle, D. J. *Spectrometric Identification of Organic Compounds*, 7th ed.; Wiley: New Jersey, 2005.

[22] Lucas, H. J.; Kennedy, E. R. *Org. Synth.* **1942**, *22*, 69.

[23] O' Toole, M. G.; Kreso, M.; Kozlowski, P. M.; Mashuta, M. S.; Grapperhaus, C. A. *J. Biol. Inorg. Chem.* **2008**, *13*, 1219–1230.

[24] (a) Lee, Y.; Kinney, R. A.; Hoffman, B. M.; Peters, J. C. *J. Am. Chem. Soc.* **2011**, *133*, 16366–16369. (b) Mankad, N. P.; Whited, M. T.; Peters, J. C. *Angew. Chem. Int. Ed.* **2007**, *119*, 5870–5873. (c) Kisko, J. L.; Hascall, T.; Parkin, G. *J. Am. Chem. Soc.* **1998**, *7863*, 10561–10562. (d) Brown, S. D.; Betley, T. A.; Peters, J. C. *J. Am. Chem. Soc.* **2003**, *125*, 322–323.

[25] (a) Yu, Y.; Sadique, A. R.; Smith, J. M.; Dugan, T. R.; Cowley, R. E.; Brennessel, W. W.; Flaschenriem, C. J.; Bill, E.; Cundari, T. R.; Holland, P. L. *J. Am. Chem. Soc.* **2008**, *130*, 6624–6638. (b) Dugan, T. R.; Holland, P. L. *J. Organomet. Chem.* **2009**, *694*, 2825–2830.

[26] (a) Dey, A.; Ghosh, A. *J. Am. Chem. Soc.* **2002**, *124*, 3206–3207. (b) de Oliveira, F. T.; Chanda, A.; Banerjee, D.; Shan, X.; Mondal, S.; Que, L. Jr.; Bominaar, E. L.; Münck, E.; Collins, T. J. *Science*, **2007**, *315*, 835–838. (c) Grapperhaus, C. A.; Mienert, B.; Bill, E.; Weyhermüller; Wieghardt, K. *Inorg. Chem.*, **2000**, *39*, 5306–5317.

[27] (a) Cowley, R. E.; Eckert, N. A.; Elhaïk, J.; Holland, P. L. *Chem. Commun.* **2009**, *48*, 1760–1762. (b) Mankad, N.; Müller, P.; Peters, J. C. *J. Am. Chem. Soc.* **2010**, *132*, 4083–4085. (c) Jensen, M. P.; Mehn, M. P.; Que, Jr., L. *Angew. Chem.* **2003**, *115*, 4493–4496.

[28] I. S. Weitz and M. Rabinovitz *J. Chem. Soc. Perkin Trans.* **1993**, *1*, 117−120.

[29] Chaudhuri, P.; Hess, M.; Weyhermüller, T.; Wieghardt, K. *Angew. Chem. Int. Ed.* **1999**, *38*, 1095–1098.

[30] S. Laha and R. G. Luthy *Environ. Sci. Technol.* **1990**, *24*, 363–373.

[31] APEX2, Version 2008.3-0 / 2.2-0, Bruker AXS, Inc.; Madison, WI 2007.

[32] SAINT Version 7.53a / 7.46a, Bruker AXS, Inc.; Madison, WI 2007.

[33] Sheldrick, G. M. *SADABS*, Version 2007/4, Bruker AXS, Inc.; Madison, WI 2007.

[34] Sheldrick, G. M. *SHELXTL*, Version 6.12; Brucker AXS, Inc.: Madison, WI, 2001.

[35] International Tables for X-Ray Crystallography 1992, Vol. C., Dordrecht: Kluwer Academic Publishers.

Chapter 4

Synthesis and Characterization of Homo- and Heterobimetallic Complexes of the Formula: [ONO]M'$[ONO]_2$M

4.1 Introduction

The study of multi-metallic complexes has become an important area of research owing to the ability of such complexes to facilitate multi-electron transformations. Homo- and heterobimetallic complexes are often found in catalyst precursors or active catalysts for cross-coupling,[1, 2, 3, 4] polymerization,[1, 5] and small molecule activation reactions.[1, 6, 7] In addition to their potential roles in catalytic processes, bimetallic combinations are often featured in the active sites of many metalloenzymes.[8, 9] In particular, the [FeFe] and [NiFe] hydrogenases possess two metal centers in the active sites that work cooperatively to facilitate bond activation of hydrogen.[8, 9]

One approach to developing bimetallic systems entails the design of a suitable ligand framework that allows the coordination environment of the metal centers to mimic those of metalloenzyme active sites.[10, 11] Figure 4.1 displays the dinucleating ligand platform, XDK (H_2XDK = *m*-xylenediamine bis(Kemp's triacid imide), employed by the Lippard group in which the carboxylate ligands were incorporated to mimic the metal binding sites in hemerythrin.[11, 12] Metallation of this ligand with two equivalents of Fe(II),[13] Mg(II),[14] Co(II),[15] and Mn(II),[16] salts led to formation of new homobimetallic complexes. Furthermore, it was shown that reaction of mononuclear [Zn^{II}(XDK)(H_2O)] with $M^{II}(acac)_2 \bullet 2H_2O$ (acac = 2,4-pentaneionate; M = Co, Mn, Fe, Ni)[17] afforded heterobimetallic compounds. The rigidity of the XDK ligand scaffold imparts stability in the formation of bimetallic complexes with bridging carboxylates. These complexes served as structural models for understanding the reactivity and behavior of various metalloprotein and metalloenzyme systems.

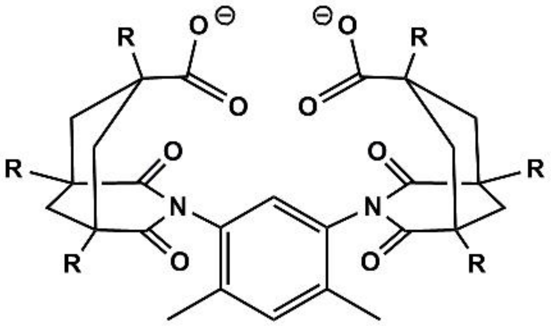

Figure 4.1. The XDK ligand used by Lippard and coworkers to prepare new bimetallic complexes.

The crucial role of ligand architecture in the construction of new bimetallic systems is further highlighted in the use of macrocyclic ligand systems with two metal-binding sites..[11, 18, 19] For example, the Bosnich group prepared a family of diphenoxide-based ligand scaffolds that allowed encapsulation of two metals in different coordination environments (Scheme 4.1).[11, 19] By sequentially introducing the metals into each coordination site, this type of metallation strategy permitted tunability of the metal centers, which was conducive for investigating the structural properties and cooperative redox reactivity of various bimetallic combinations. It was shown that when M_a = Co(II) or Fe(II) for the monometallic system, the metals were readily oxidized to the +3 oxidation state.[11] However, incorporation of the second metal resulted in deactivation of the six-coordinate component. This was likely caused by ligand reorganization induced by oxidation of the metals, a phenomenon known as mechanical coupling.[19]

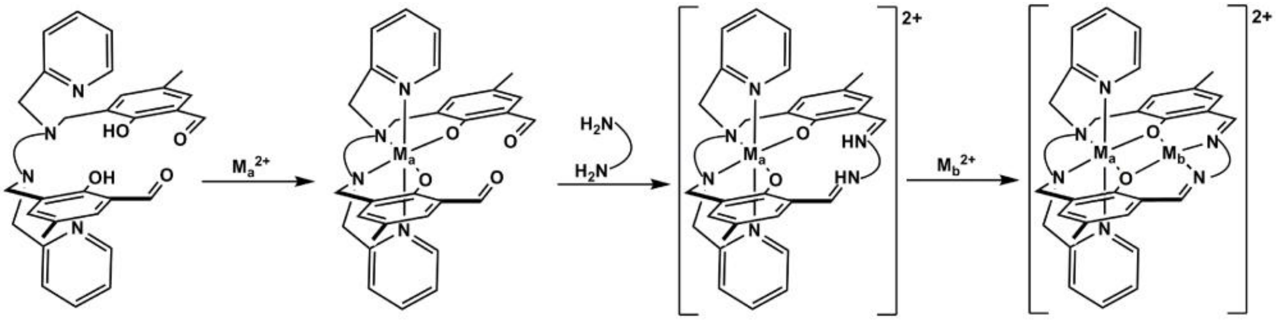

Scheme 4.1. Stepwise synthesis of bimetallic complexes based on dinucleating diphenoxide-based ligand scaffold.

Our laboratory has taken a modular approach towards assembling bimetallic complexes incorporating redox cofactors for the purposes of investigating metal–ligand redox cooperativity. A myriad of homoleptic, six-coordinate compounds of the formula M[ONO]$_2$ ([ONO^{cat}]H$_3$ = bis(3,5-di-*tert*-butyl-2-phenol)amine; M = Fe, Cu, Ni, Zn, Cd,[20] M = Al, Ga, Ca, Ba,[21] M = Mn, Co,[22] M = Ti, V, Ge, Sn,[23] M = Pb[24]) have been reported in the literature. While many of these complexes display multiple stable oxidation states, their saturated coordination sphere limits their ability to perform inner-sphere reactivity. In contrast, ligand-based multi-electron reactivity is achievable using metal complexes coordinated by a single [ONO] ligand.[25, 26, 27, 28] By combining the preformed monomers, {[ONO]M'} and M[ONO]$_2$, two novel bimetallic complexes of the form [ONO]M'[ONO]$_2$M (M' = Fe, Zn; M = Fe) have been prepared. This platform lays the foundation for a general synthetic method to access a wide variety of bimetallic complexes that could be promising for multi-electron transformations.

4.2 Results

4.2.1 Synthesis and Characterization of [ONO^{sq}]Zn(py)$_2$

A new zinc complex supported by one [ONO] ligand was prepared for use as a synthon in new heterobimetallic complex synthesis. As shown in Scheme 4.2, treatment of Zn(OAc)$_2$ with one equivalent of K$_2$[ONO^{sq}] in neat pyridine produced [ONO^{sq}]Zn(py)$_2$ (**11**) in 71% yield. Single crystals suitable for X-ray crystallography were obtained from diffusion of acetonitrile into pyridine solutions of **11** at –35 °C.

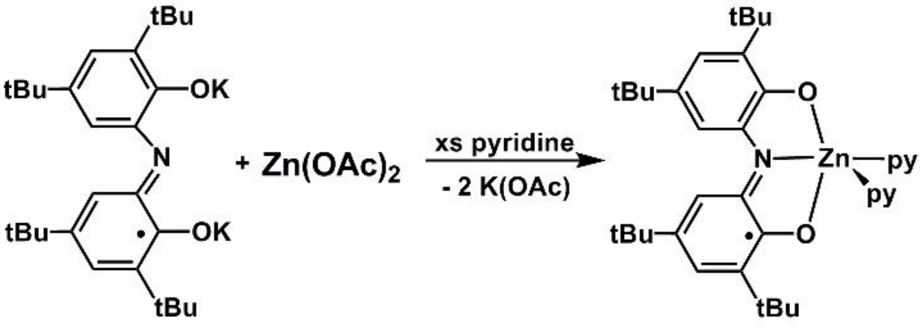

$K_2[ONO^{sq}]$ **11**

Scheme 4.2. Synthesis of complex **11**.

Through X-ray diffraction studies, the oxidation state of the [ONO] ligand and the geometry of complex **11** are elucidated. An ORTEP diagram of the crystal structure is depicted in Figure 4.2. A list of selected bond measurements is shown in Table 4.1. The C–N and C–O bond lengths of 1.354(6) Ǻ and 1.312(5) Ǻ, respectively, along with the C–C ring bond lengths of the [ONO] ligand are consistent with what has been observed in other metal complexes supported by the $[ONO^{sq}]^{2-}$ ligand.[26, 29, 30, 31] The geometric parameter ² = (– ~) / 60 (= ∠O(1)–Zn(1)–O(2); ~ = ∠N(1)–Zn (1)–N(2)) was used to probe the coordination geometry of the zinc ion.[32] The ² value of 0.305 indicates that the geometry at Zn(1) lies in between a square pyramid and trigonal bipyramid.

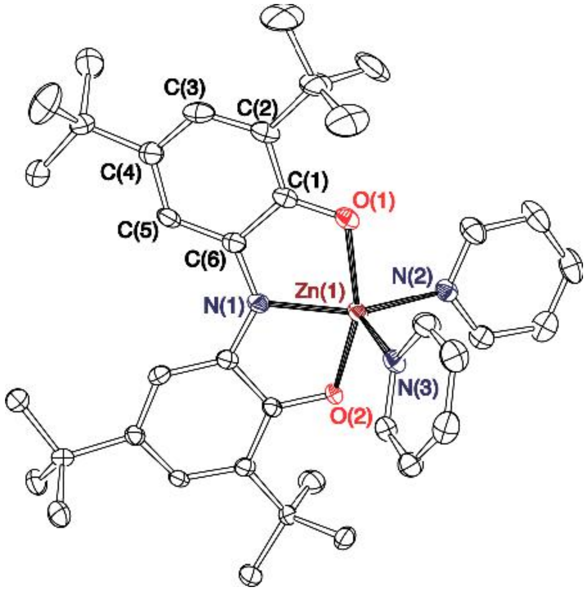

Figure 4.2. ORTEP diagram of **11**. Thermal ellipsoids are displayed at 50% probability. The hydrogen atoms and solvent molecules have been removed for simplicity.

Table 4.1. Selected bond lengths (Å) and angles (°) of **11**.

Bond	Length	Bond	Angle
O(1)–C(1)	1.312(5)	O(1)–Zn(1)–O(2)	157.6(1)
C(1)–C(2)	1.435(6)	O(1)–Zn(1)–N(1)	79.5(1)
C(2)–C(3)	1.376(6)	N(1)–Zn(1)–N(2)	139.3(1)
C(3)–C(4)	1.419(6)	N(1)–Zn(1)–N(3)	120.4(2)
C(4)–C(5)	1.385(6)	N(2)–Zn(1)–N(3)	100.2(1)
C(5)–C(6)	1.410(6)		
C(1)–C(6)	1.453(6)		
N(1)–C(6)	1. 354(6)		
Zn(1)–O(1)	2.097(3)		
Zn(1)–N(1)	2.008(4)		

Spectroscopic data for **11** further supports that the [ONO] ligand adopts the semiquinonate form while zinc retains its +2 oxidation state. When perpendicular mode EPR experiments were conducted on toluene or pyridine solutions of **11** at 77 K, an isotropic resonance was observed at g = 2.00 (Figure 4.3). This is consistent with **11** being an $S = \frac{1}{2}$ system with an unpaired electron localized on the ligand scaffold.

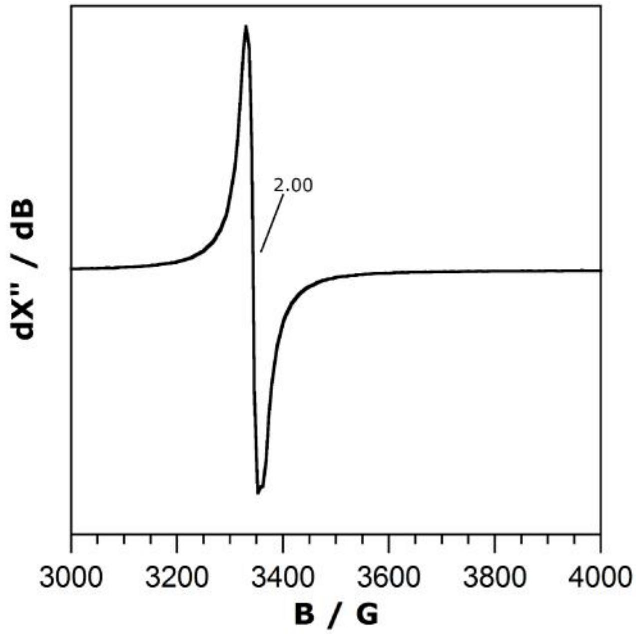

Figure 4.3. X-band EPR spectrum of [ONO^{sq}]Zn(py)$_2$ (**11**). Experimental conditions: $B_1 \perp B_0$; solvent, toluene or pyridine; temperature, 77 K.

4.2.2 Synthesis and Characterization of Fe$_2$[ONO]$_3$ and FeZn[ONO]$_3$

The diiron complex, Fe$_2$[ONO]$_3$ (**12**), was initially isolated as an unexpected side product in reduction reactions with [ONO^q]FeX$_2$, as described in Chapter 3. For example, the reduction of [ONO^q]FeCl$_2$ (**3a**) in the absence of pyridine led to elimination of KCl and isolation of the iron-containing product, Fe$_2$[ONO]$_3$ (Scheme 4.3). This isolation of this unsymmetrical dimer triggered our interest in developing a rational synthetic route to this unusual diiron complex.

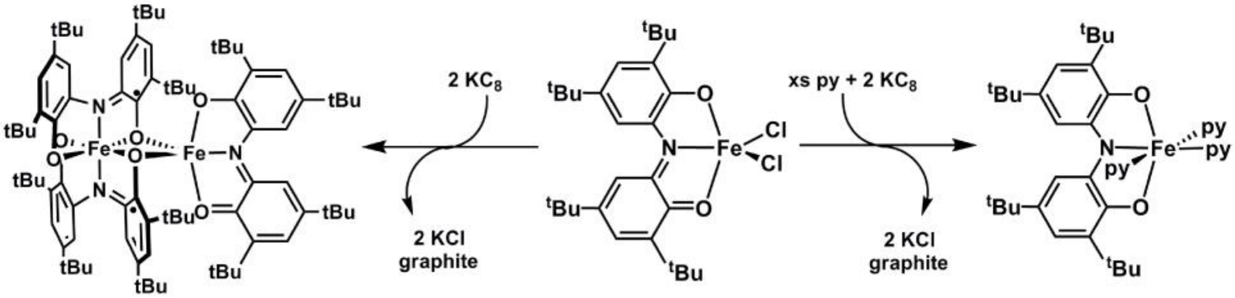

Scheme 4.3. Reductions of [ONO^q]FeCl$_2$ in presence or absence of pyridine.

A route to Fe$_2$[ONO]$_3$ was designed retro-synthetically by breaking the complex up into two parts: a {[ONO]Fe} fragment and a six-coordinate Fe[ONO]$_2$ species. The source for {[ONO]Fe} could be derived from a series of five-coordinate [ONO^q]Fe^{III}X$_2$ complexes in which the two X-type ligands could be replaced by Fe[ONO]$_2$ as a dianionic ligand source. As illustrated in Scheme 4.4, reduction of Fe[ONO]$_2$ was carried out using two equivalents of potassium graphite at room temperature. Addition of one equivalent of **3a** to the slurry containing K$_2$(Fe[ONO]$_2$) *in-situ* furnished **12** in 77% yield. Alternatively, [ONO^{cat}]Fe^{III}(py)$_3$ (**7**) was also a source for {[ONO]Fe} wherein the three labile pyridine ligands were displaced by Fe[ONO]$_2$ to produce **12** in 88% yield. In this case, Fe[ONO]$_2$ could be considered a neutral bidentate ligand to the {[ONO^{cat}]Fe} species.

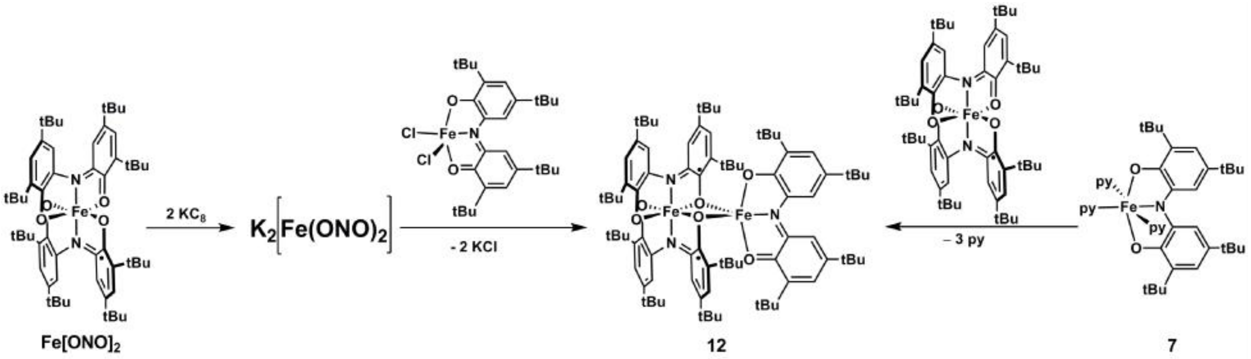

Scheme 4.4. Synthesis of complex **12**.

Analysis of the structural metrics of **12**, obtained by X-ray crystallography, is applied to allow for determination of possible metal and ligand oxidation states. Figure 4.4 shows the ORTEP diagram for the solid-state structure of **12** and Table 4.2 lists selected bond measurements. The geometry at the six-coordinate iron center is pseudo-octahedral. The ² value of 0.265 (~ = ∠N(1)–Fe(2)–O(6);   = ∠O(1)–Fe(2)–O(2)) indicates that Fe(2) lies in between square-pyramidal and trigonal-bipyramidal geometries.[30] The carbon–carbon ring bond lengths of the [ONO] ligand bound meridionally to Fe(2) are consistent with the bond lengths observed in the $[ONO^{q}]^{1-}$ form of the ligand.[26, 28] The C(72)–O(6) bond length of 1.354(2) Å is longer than the C(58)–O(5) bond length of 1.306(2) Å, an indication that the carbon–oxygen bonds containing the bridging oxygen atoms have more C(aryl)–O single bond character than the C–O bonds containing the non-bridging oxygen have.[33] This is also suggestive of a radical that is localized on the aryl carbon containing the non-bridging oxygen atom coordinated to Fe(1). The Fe(2)–O(6) bond length of 1.974(1) Å is shorter than the Fe(1)–O(6) bond length of 2.159(1) Å. Based on the bond metric data, the two [ONO] ligands surrounding the Fe(1) likely are in the dianionic $[ONO^{sq}]^{2-}$ form while the [ONO] ligand coordinated to the five-coordinate Fe(2) is in the $[ONO^{q}]^{1-}$ form. The two bridging oxygen atoms derived from the $[ONO^{sq}]^{2-}$ bind more closely to the five-coordinate iron site, suggesting that these two oxygen atoms act more like anionic X-type ligands to Fe(2). If the bridging O(6) and O(4) atoms have already been assigned as anionic X-type ligands to the Fe(2) site, this leaves two anionic O(3) and O(5) atoms behaving as X-type ligands to Fe(1). Therefore, the six-coordinate iron center has an oxidation state of +2. Thus, the structural data indicates that **12** adopts the following form: $[ONO^{q}]Fe[ONO^{sq}]_2Fe$, where the $\{[ONO^{sq}]_2Fe^{II}\}^{2-}$ can behave as a dianionic ligand to the $\{[ONO^{q}]Fe^{III}\}^{2+}$ fragment.

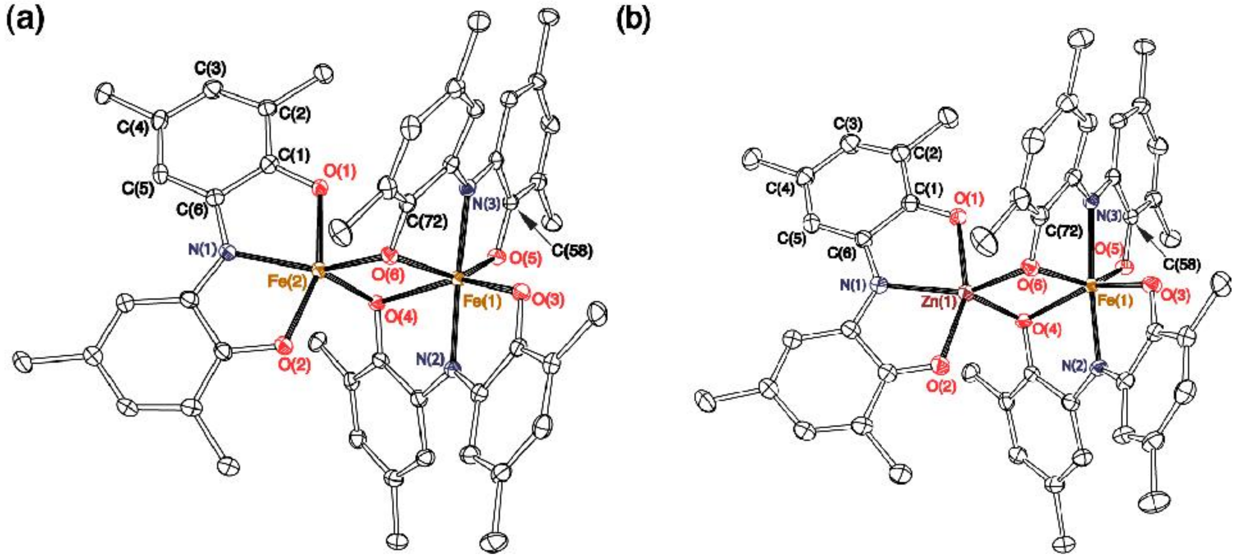

Figure 4.4. ORTEP diagram of **12** (*a*) and **13** (*b*). Thermal ellipsoids are displayed at 50% probability. The *tert*-butyl groups, hydrogen atoms, and solvent molecules have been removed for simplicity.

Table 4.2. Selected bond lengths (Å) and angles (°) of **12** and **13**.

Bond lengths / Angle	**12**	**13**
C(1)–C(2)	1.422(3)	1.454(3)
C(2)–C(3)	1.376(3)	1.361(4)
C(3)–C(4)	1.415(4)	1.439(4)
C(4)–C(5)	1.372(3)	1.360(3)
C(5)–C(6)	1.417(3)	1.422(3)
C(6)–C(1)	1.441(3)	1.466(3)
C(1)–O(1)	1.311(3)	1.269(3)
C(72)–O(6)	1.354(2)	1.353(2)
C(58)–O(5)	1.306(2)	1.299(3)
Fe(1)–N(2)	2.014(2)	2.036(2)
Fe(1)–N(3)	2.029(2)	2.024(2)
Fe(1)–O(3)	1.998(1)	
Fe(1)–O(4)	2.165(1)	
Fe(1)–O(5)	1.953(1)	2.011(2)
Fe(1)–O(6)	2.159(1)	2.114(1)
Fe(2)–O(6)	1.974(1)	–
Fe(2)–O(4)	1.978(1)	–
Fe(2)–O(1)	1.928(1)	–

Fe(2)–O(2)	1.927(1)	–
Fe(2)–N(1)	2.073(2)	–
Fe(1)–Fe(2)	3.0726(5)	–
Zn(1)–O(6)	–	2.019(2)
Zn(1)–O(4)	–	2.013(1)
Zn(1)–O(1)	–	2.006(2)
Zn(1)–O(2)	–	2.027(2)
Zn(1)–N(1)	–	2.145(2)
Zn(1)–Fe(2)	–	3.0542(7)
N(2)–Fe(1)–N(3)	164.79(7)	164.44(7)
N(2)–Fe(1)–O(3)	79.16(6)	78.65(7)
O(3)–Fe(1)–O(6)	92.75(6)	92.05(6)
O(1)–Fe(2)–O(2)	156.53(6)	–
O(2)–Fe(2)–O(6)	98.49(6)	–
N(1)–Fe(2)–O(6)	140.64(6)	–
N(1)–Zn(1)–O(6)	–	140.56(7)
O(1)–Zn(1)–O(2)	–	155.70(7)
O(2)–Zn(1)–O(6)	–	100.76(7)

Mössbauer spectroscopy was applied to better understand the electronic properties of the iron centers in **12**. As shown in Figure 4.5, the overall Mössbauer spectrum could be fitted by two quadrupole doublets with quadrupole shift values of 1.6 mm/s and 1.81 mm/s, which is consistent with the two iron centers having different coordination geometries. Isomer shift values of 0.59 mm/s and 0.49 mm/s for each quadrupole doublet fall in the range of high-spin Fe(II) and high-spin Fe(III),[34] supporting the contention that $Fe_2[ONO]_3$ is an iron(II)–iron(III) system.

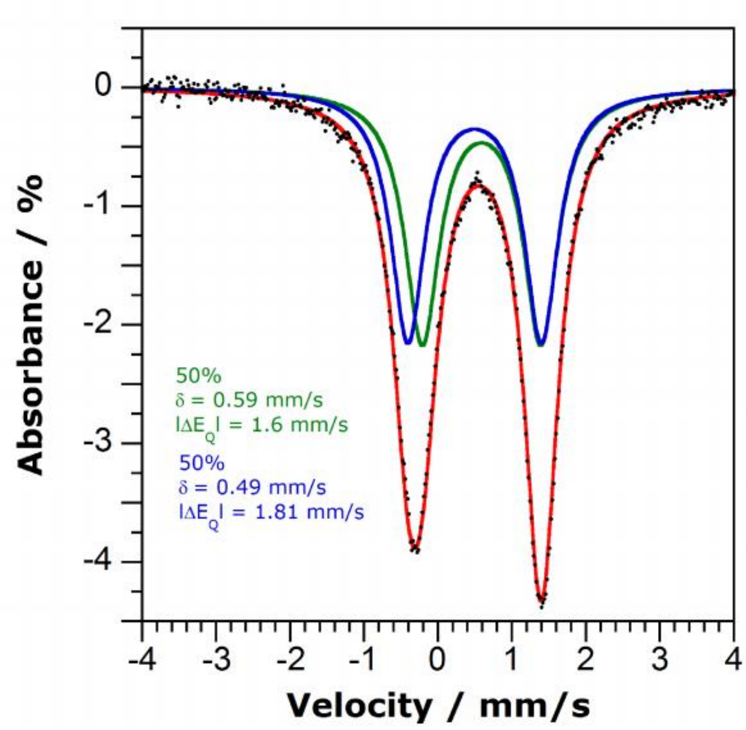

Figure 4.5. Mössbauer spectrum of $Fe_2[ONO]_3$ (**12**). Data collected at 80 K.

By applying the same modular approach used to generate **12**, we were able to assemble new heterobimetallic systems. Towards our goal of preparing the $FeZn[ONO]_3$ (**13**) containing five-coordinate iron and six-coordinate zinc centers, we first reduced $Zn[ONO]_2$ with two equivalents of KC_8 at ambient temperature. Subsequently, one equivalent of **3a** was added *in-situ* to the slurry of $K_2(Zn[ONO]_2)$ to generate $FeZn[ONO]_3$ in 60% yield (Scheme 4.5). Single crystals of **13** suitable for X-ray crystallography were obtained from diffusion of acetonitrile into diethyl ether solutions of the bimetallic complex at –35 °C. Contrary to our initially proposed structure, crystallographic data for this compound indicates that the structure contains {[ONO]Zn} and six-coordinate $Fe[ONO]_2$ fragments (Figure 4.4).

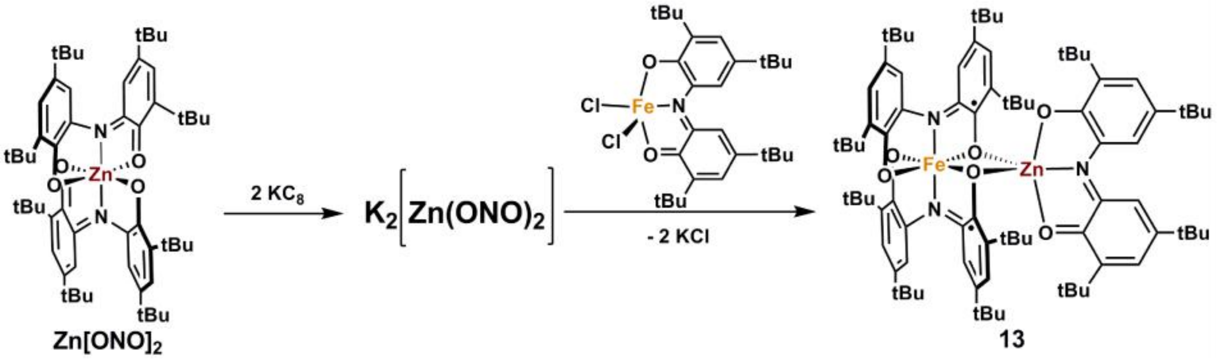

Scheme 4.5. Synthesis of complex **13**.

Alternative synthetic pathways for the preparation of FeZn[ONO]$_3$ were explored to help determine the exact nature of the heterobimetallic complex. Complex **13** was readily formed in 74% yield through the reaction of [ONO^{sq}]Zn(py)$_2$ (**11**) with Fe[ONO]$_2$ in toluene or benzene solutions (Scheme 4.6). The reaction of **7** with one equivalent of Zn[ONO]$_2$ in benzene generated the same heterobimetallic compound but with the addition of mild heating. Because the iron–zinc complex could be prepared through either using Fe[ONO]$_2$ or Zn[ONO]$_2$ as starting materials, these experiments could not confirm if the five- and six-coordinate sites were occupied by iron or zinc.

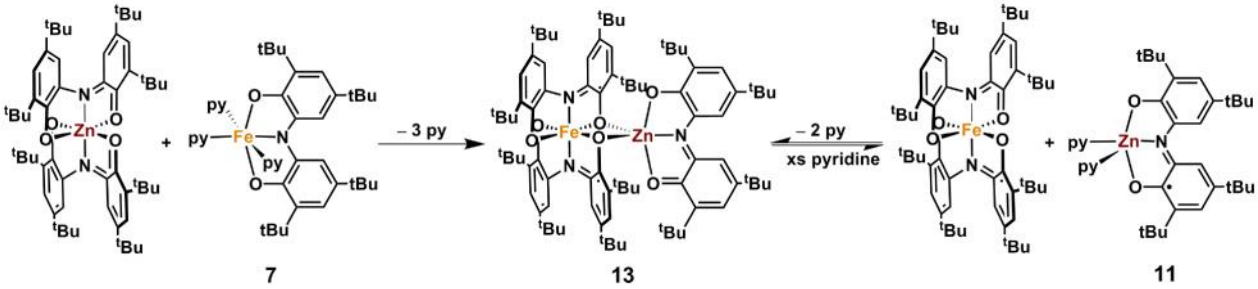

Scheme 4.6. Alternative synthetic pathways for preparing **13**.

The identity of the six-coordinate metal was confirmed by dissociating the heterobimetallic complex in pyridine. The ^{1}H NMR spectrum of **13** in pyridine-d_5 revealed the presence of Fe[ONO]$_2$ while no Zn[ONO]$_2$ was observed. The EPR spectrum of this reaction mixture displayed an isotropic signal consistent with the presence of [ONO^{sq}]Zn(py)$_2$ (**11**). These results confirm that the six-coordinate site contained iron while zinc occupied the five-coordinate site. Likewise, the ^{1}H NMR spectrum in pyridine-d_5 of the dissolved **12** also exhibited resonances pertaining to the $Fe[ONO]_2$ complex. The EPR spectrum of **12** in pyridine-d_5 showed resonances belonging to **7**. Hence, in the presence of a large excess of pyridine, dissociations of $FeZn[ONO]_3$ and $Fe_2[ONO]_3$ were highly favored to form $Fe[ONO]_2$ and the corresponding coordinatively-unsaturated {[ONO]Zn} and {[ONO]Fe} species, which were then captured by pyridine ligands to regenerate **11** and **7**, respectively.

Single-crystal X-ray crystallography is also applied to make possible oxidation state assignments to the ligand and metal entities of **13**. Figure 4.4 shows the ORTEP diagram for the solid-state structure of the iron–zinc complex while Table 4.2 lists selected bond length and angle measurements. Similar to **12**, the geometry at the six-coordinate Fe(1) is pseudo-octahedral while the ² value of 0.252 (~ = ∠N(1)–Zn(1)–O(6); = ∠O(1)–Zn(1)–O(2)) indicates that the geometry at the five-coordinate zinc lies between a square pyramid and trigonal bipyramid.[32] Based on the carbon–carbon ring bond lengths, the [ONO] ligand coordinated meriodionally to Zn(1) is also in the $[ONO^{q}]^{1-}$ form.[26, 28] Analogous to **12**, the Fe(1) is supported by two $[ONO^{sq}]^{2-}$ ligands, as evidenced by the longer C(72)–O(6) bond length of 1.353(2) Å in comparison to the C(58)–O(5) bond length of 1.299(3) Å. The Zn(1)–O(6) and Fe(1)–O(6) bond lengths of 2.019(2) Å and 2.114(1) Å, correspondingly, indicate that the bridging oxygens bind more strongly to Zn(1) as compared to the six-coordinate Fe(1). There are two possible combinations for the formal oxidation states of the metals: iron(V)–zinc(0) and iron(III)–zinc(II). Since metal complexes containing either zinc(0) and iron(V) centers are rarely observed,[35, 36, 37] the $FeZn[ONO]_3$ is best described as an iron(III)–zinc(II) system. Thus, the overall structural data indicates that **13** adopts the form: $[ONO^{q}]Zn[ONO^{sq}]_2Fe$, where the $\{[ONO^{sq}]_2Fe^{III}\}^{1-}$ can behave as a monoanionc ligand to the $\{[ONO^{q}]Zn^{II}\}^{1+}$ fragment.

4.2.3 Electrochemical and Spectroscopic Data Comparisons

To further elucidate on the structural and electronic properties of the bimetallic complexes, cyclic and differential pulse voltammetric techniques along with UV-vis-NIR spectroscopy are utilized. Figure 4.6 displays the voltammograms of **11**, **12**, and **13** as well as $Fe[ONO]_2$ and **3a** for comparison. Figure 4.7 shows the UV-vis-NIR spectra of both bimetallic complexes and $Fe[ONO]_2$.

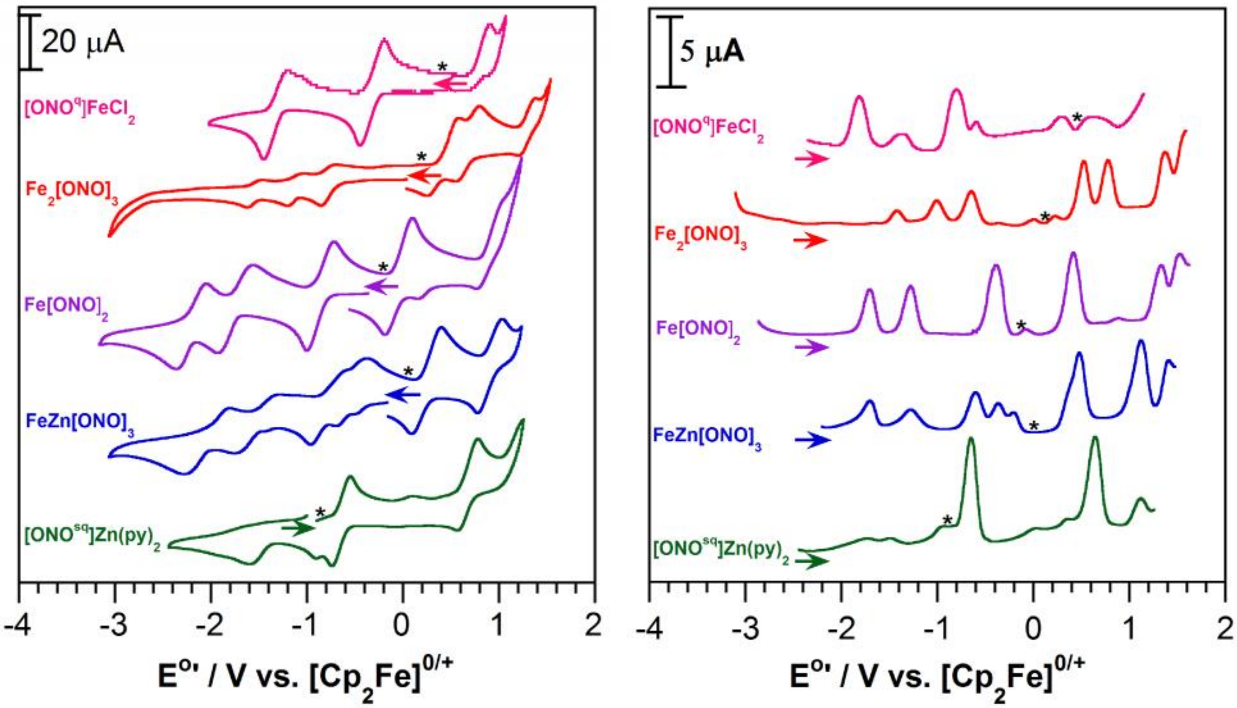

Figure 4.6. Cyclic (*left*) and differential pulse (*right*) voltammograms of $[ONO^{q}]FeCl_2$ (**3a**; magenta), $Fe_2[ONO]_3$ (**12**; red), **(13**; blue), $[ONO^{sq}]Zn(py)_2$ (**11**; green), and $Fe[ONO]_2$ (purple). Bulk of the material indicated by *. Voltammograms were recorded at 1mM analyte concentration in 0.10 M $[^{n}Bu_4N][PF_6]$ in THF using a glassy carbon working electrode, Pt wire counter electrode, $Ag^{0/+}$ wire reference, and scan rate of 200 mV/s at 298 K.

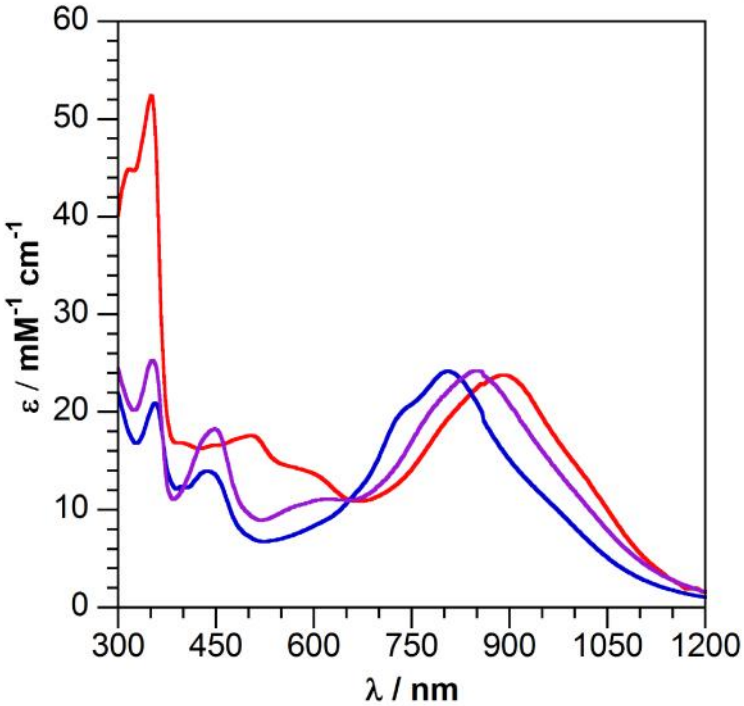

Figure 4.7. UV-vis-NIR spectra of $Fe_2[ONO]_3$ (**12**; red), $FeZn[ONO]_3$ (**13**; blue), and $Fe[ONO]_2$ (purple).

Since the $Fe_2[ONO]_3$ complex is a combination of the $\{[ONO^q]Fe\}$ and $Fe[ONO]_2$ species, the voltammetric and spectroscopic data of the bimetallic complex are compared to those of $[ONO^q]FeCl_2$ and $Fe[ONO]_2$. Complex **12** displays two partially-reversible oxidation events and three partially-reversible reduction events, none of which appear to correlate with the redox events found in the mononuclear components. Although the diiron complex and $Fe[ONO]_2$ exhibit broad absorptions in the NIR region, we cannot conclusively assign the absorbance at 850 nm for **12** to be based on the $Fe[ONO]_2$ component.

Interestingly, the redox and spectroscopic features of $FeZn[ONO]_3$ appear to correlate with those of $Fe[ONO]_2$. Complex **13** displays two partially-reversible oxidation events as well as multiple partially-reversible reduction events. The oxidation event at 0.476 V of **13** seem to compare with that of $Fe[ONO]_2$ at 0.480 V. In addition, the redox couples at −1.70 V and −1.28 V of the heterobimetallic compound align closely with those corresponding to $Fe[ONO]_2$ at

-1.75 V and -1.30 V. The absorptions in the visible region for **13** (356 nm and 436 nm) appear to correlate with those of Fe[ONO]$_2$ (354 nm and 448 nm).

However, as with complex **12**, voltammetric and spectroscopic features cannot be assigned to particular mononuclear components of the heterobimetallic **13**. The broad NIR absorptions of **12** (850 nm), **13** (806 nm), and Fe[ONO]$_2$ (854 nm) can be ascribed to intramolecular charge-transfer transitions likely stemming from the metal-ligand as well as ligand-ligand interactions within all three redox-active complexes. Various metal complexes containing [ONO^{q}]$^{1-}$ and [ONO^{sq}]$^{2-}$ ligands also feature broad charge-transfer bands in the NIR region.[20–28] Consequently, it is difficult to discern whether the electrochemical redox events and electronic absorption attributes are based on specific mononuclear constituents of each bimetallic complex.

4.3 Discussion

4.3.1 Reactivity Patterns of the Bimetallic Synthesis

The unexpected reactivity pathways toward generating FeZn[ONO]$_3$ (**13**) via Zn[ONO]$_2$ and either [ONO^{q}]FeCl$_2$ (**3a**) or [ONO^{cat}]Fe(py)$_3$ (**7**) are still under investigation. Reaction of [ONO^{sq}]Zn(py)$_2$ (**11**) and Fe[ONO]$_2$ at ambient temperature produces **13** in a relatively straightforward manner (Scheme 4.6). On the other hand, heating is required in order for **7** and Zn[ONO]$_2$ to react completely and form the same heterobimetallic compound. Furthermore, metathesis of K$_2$(Zn[ONO]$_2$) with one equivalent of **3a** also leads to the formation of FeZn[ONO]$_3$ comprising five-coordinate zinc and six-coordinate iron sites (Scheme 4.5). These experiments suggest that formation of **13** proceeds through transmetallation reactions of Zn[ONO]$_2$ and its {[ONO]Fe} counterpart to generate the Fe[ONO]$_2$ fragment, which then coordinates to the {[ONO]Zn} species. It has been shown that Zn[ONO]$_2$ can act as a delivery agent of the [ONO] ligand for tin(IV) complexes.[38] This fact further supports the argument that a [ONO] ligand derived from Zn[ONO]$_2$ can migrate towards the {[ONO]Fe} to form the Fe[ONO]$_2$ fragment of **13**.

Consequently, for bimetallic combinations of the form [ONO]M'[ONO]$_2$M, where M' = Fe or Zn, the six-coordinate Zn[ONO]$_2$ is less preferred. Attempts to prepare a dizinc complex of the form [ONO]Zn[ONO]$_2$Zn have been carried out through treatment of the Zn[ONO]$_2$ with [ONO^{sq}]Zn(py)$_2$ at ambient temperature and at 45 °C. However, this pathway does not lead to a new a dizinc product as consumption of Zn[ONO]$_2$ is not observed. This corroborates with the contention that the Fe[ONO]$_2$ fragment is more strongly favored in bimetallic complexes of the form [ONO]M'[ONO]$_2$M.

4.3.2 Non-Innocent Behaviors of Bimetallic Complexes

By replacing the iron with a redox-inactive zinc, we anticipate that the isostructural complexes **12** and **13** will reveal methodical variations with regards to their redox properties. However, it appears that observations of such systematic changes might have been complicated by the metal-ligand non-innocent behaviors. Based on the bond metrics obtained from X-ray diffraction data, we characterize **12** as [ONO^{q}]Fe^{III}[ONO^{sq}]$_2$Fe^{II} and **13** as [ONO^{q}]Zn^{II}[ONO^{sq}]$_2$Fe^{III}. However, due to the metal-ligand redox interactions influencing electron delocalization, we cannot disregard other possible metal and ligand oxidation state interpretations.

4.4 Summary and Conclusion

Through exploiting the redox properties of the monometallic fragments, the redox-active monomers can be combined to construct new bimetallic combinations. The rich redox profiles of complexes **12** and **13** suggest that they can potentially impart unique synergistic bimetallic reactivity. We envision that the Fe[ONO]$_2$ fragment can serve as a redox cofactor for the five-coordinate {[ONO]Fe/Zn}species where reactivity can take place in the open-coordination site. This platform has also inspired the synthesis of new bimetallic combinations for the purposes of exploring new multi-electron reactivity.

4.5 Experimental

General Procedures. The potassium graphite KC$_8$,[39] [ONO^{cat}]H$_3$,[25, 26] K[ONO^q],[30] Fe[ONO]$_2$,[20] and Zn[ONO]$_2$[20] were synthesized according to published procedures. Synthesis of complexes **3a** and **7** have been reported in chapter 2 and in the literature.[28] Potassium hydride (Alfa Aesar) was washed with dry degassed pentane to remove the oil prior to usage. The air- and moisture sensitive compounds and reactions reported below require all manipulations to be carried out under air- and moisture-free conditions using standard glovebox or Schlenk techniques. Solvents were sparged with argon and then deoxygenated and dried by passage through Q5 and activated alumina columns, respectively. To test for effective oxygen and water removal, solvents were treated with a few drops of a purple THF solution of sodium benzophenone ketyl.

Physical Measurements. The UV-vis-NIR spectra were recorded with Perkin–Elmer Lambda 800 Spectrometer as solutions in toluene or pyridine. Electrospray ionization mass spectrometry (MS/ESI) was performed at the Mass Spectrometry Facility at University of California, Irvine. NMR spectra were acquired on a Bruker Avance 400/500/600 MHz spectrometer. Perpendicular-mode X-band EPR spectra were collected using Bruker EMX spectrometer equipped with ER041XG microwave bridge. ^{57}Fe Mössbauer spectra were measured on liquid nitrogen cooled samples at zero magnetic field with a constant acceleration spectrometer (SEE Co., Edina, MN).

Electrochemical Methods. Cyclic voltammograms were collected using Gamry Series G 300 potentiostat/galvanostat/ZRA (Gamry Instruments, Warminster, PA) inside a nitrogen-filled glovebox. A glassy carbon working electrode (3.0 mm), platinum wire counter electrode, and silver wire reference electrode were used. Sample concentrations were 1.0 mM in THF with 0.10 M tetrabutylammonium hexafluorophosphate as the supporting electrolyte. All potentials are referenced to $[Cp_2Fe]^{+/0}$ using $(Cp)_2Fe$ as an internal standard. Decamethylferrocene (Acros) and ferrocene (Acros) was purified by sublimation under reduced pressure. Tetrabutylammonium hexafluorophosphate (Acros) was recrystallized from ethanol three times and dried in the oven before use.

Crystallographic Methods. X-ray diffraction data were collected on crystals mounted on glass fibers using a Bruker CCD platform diffractometer equipped with a CCD detector. Measurements were carried out using Mo K_α (λ = 0.71073 Å) radiation, which was wavelength selected with a single-crystal graphite monochromator. A full sphere of data was collected for each crystal structure. The APEX2 program package was used to determine unit-cell parameters and to collect data.[40] The raw frame data were processed using SAINT[41] and SADABS[42] to yield the reflection data files. Subsequent calculations were carried out using the SHELXTL[43] program suite. Structures were solved by direct methods and refined on F^2 by full-matrix least-squares techniques to convergence. Analytical scattering factors for neutral atoms were used throughout the analyses. Hydrogen atoms, though visible in the difference Fourier map, were generated at calculated positions and their positions refined using the riding model. ORTEP diagrams were generated using ORTEP-3 for Windows[44] and all thermal ellipsoids are drawn at the 50% probability level.

Table 4.3. X-ray diffraction data-collection and refinement parameters for complexes **11**, **12**, **13**.

	11•0.5(C_5H_5N)•0.5(CH_3CN)	**12**•0.5(CH_3CN)	**13**
Empirical formula	$C_{38}H_{50}N_3O_2$ Zn•0.5(C_5H_5N)•0.5(CH_3CN)	$C_{84}H_{120}N_3O_6Fe_2$•0.5(CH_3CN)	$C_{84}H_{120}N_3O_6FeZn$
Formula weight	706.25	1400.06	1389.04
Crystal system	Monoclinic	Monoclinic	Monoclinic
Space group	$P2_1$	$P2_1/c$	$P2_1/c$
T	88(2) K	88(2) K	143(2) K
a	14.208(3) Å	15.5180(10) Å	15.5857(8) Å
b	20.222(4) Å	20.0893(13) Å	20.1236(11) Å
c	14.512(3) Å	26.9179(18) Å	26.8587(14) Å
α	90°	90°	90°
β	108.954(3)°	104.1755(9)°	104.2326(7)°
γ	90°	90°	90°
V	3943.6(12) Å^3	8136.0(9) Å^3	8165.4(7) Å^3
Z	4	4	4
Reflections collected	46059	87960	87548
data/restraints/parameters	17365 / 1/ 899	16658 / 0 / 916	16711 / 0 / 985
R1 [$I > 2\sigma(I)$][a]	0.0435	0.0412	0.0429
wR2 (all data)[a]	0.1005	0.1059	0.1300
GOF[a]	1.074	1.013	1.035

[a] $R1 = \Sigma||F_o| - |F_c||/\Sigma|F_o|$; $wR2 = [\Sigma[w(F_o^2 - F_c^2)^2]/\Sigma[w(F_o^2)^2]]^{1/2}$; $GOF = [\Sigma w(|F_o| - |F_c|)^2/(n - m)]^{1/2}$

Synthesis of [ONO^{sq}]Zn(py)$_2$ (11). A 10 mL pyridine solution of 125 mg of Zn(OAc)$_2$ (0.681 mmol, 1 equiv.) was treated with 340 mg of K_2[ONO^{sq}] (0.680, 1 equiv.) at room temperature. After 18 hours, the solid byproduct was filtered and washed using 15 mL of pyridine solvent. The resulting dark green solution was concentrated to reduced volume prior to diffusion of acetonitrile at –35 ˚C to generate dark green crystals. Yield: 312 mg (71%). Anal. Calc. (Found) for $C_{38}H_{50}N_3O_2Zn$ (%): C: 70.63 (70.14); 7.80 (7.87); N: 6.50 (6.23).

Synthesis of Fe$_2$[ONO]$_3$ (12). *Method A*: A combination of 30.5 mg of potassium metal (0.780 mmol, 2 equiv.) and 77.5 mg of graphite (6.45 mmol, 16 equiv.) was heated under vacuum in the presence of a Teflon stir bar with constant agitation until the solids were finely divided and bronze in color. A slurry of this KC_8 was prepared by addition of 5 mL of THF and frozen at 77 K. To this mixture, a 10 mL THF solution containing 352 mg of Fe[ONO]$_2$ (0.390 mmol, 1 equiv.) was added and the resultant brown-black solution was stirred at room temperature for 1 hour. The mixture was frozen and upon just thawing, 214 mg of **3a** (0.390 mmol, 1 equiv.) in 10 mL of THF was added. The mixture stirred overnight at room temperature, during which time it became a purple-black color. The reaction mixture was filtered through a bed of celite and the solvent was removed from the filtrate under reduced pressure to yield a glassy, black foam. Addition of 3 mL of acetonitrile to this residue and cooling at 238 K yielded the product as a dark purple powder (243 mg over two crops, 77%).

Method B: To a 10 mL toluene solution of 131 mg of Fe[ONO]$_2$ (0.146 mmol, 1 equiv.), 105 mg of **7** (0.146 mmol, 1 equiv.) was added and stirred at ambient temperature for 20 hours. The resulting dark brown solution was placed under reduced pressure to remove the volatiles. Upon dissolving the dark residue again in toluene, diffusion of acetonitrile at 238 K yielded the product as a dark purple powder. Yield: 177 mg (88%). UV-vis-NIR (THF) λ_{max}/nm (ε/ $M^{-1}cm^{-1}$): 318 (44,900), 350 (52,400), 506(17,600), 890 (23,700). Anal. Calc. (Found) for $C_{84}H_{121}N_3O_6Fe_2$ (%): C, 73.08 (72.93); H, 8.83 (8.74); N, 3.05 (2.95). MS(ESI+) m/z: 1378.75 (M+)

Synthesis of FeZn[ONO]$_3$ (13). *Method A*: A combination of 116 mg of potassium (2.90 mmol, 2 equiv.) and 280 mg of graphite (23.3 mmol, 16 equiv.) was heated under vacuum until the solids were finely divided and bronze in color. A suspension of KC_8 in 100 mL of THF was cooled in the cold well. Upon just thawing, 1.34g of Zn(ONO)$_2$ (1.47 mmol, 1 equiv.) was added, and the black-green solution was allowed to stir at room temperature. After 5 hours, the reaction mixture was cooled, and a cold solution containing 805 mg of **3a** (1.47 mmol, 1 equiv.) in THF was added drop-wise. The black-green solution was then allowed to stir at room temperature overnight. After filtering the solution through celite on a fine frit, the solvent was removed to give a black-green solid. The product was recrystallized from a 1:1 layered solution of diethyl ether and acetonitrile to give the final product in 60% yield (1.24g).

Method B: To a 10 mL toluene solution of 132 mg of Fe[ONO]$_2$ (0.146 mmol, 1 equiv.) 94.5 mg of complex **11** (0.146 mmol, 1 equiv.) was added and the dark green solution stirred at room temperature for 20 hours. Upon removal of volatiles under reduced pressure, the resulting dark green residue was dissolved again in toluene. Diffusion of acetonitrile at 238 K yielded dark green product in powder form. Yield: 150.6 mg (74%). Anal. Calc. (Found) for $C_{84}H_{120}FeN_3O_6Zn$ (%): C, 72.63 (72.35); H, 8.71 (9.15); N, 3.02 (2.93). ^{1}H NMR (400 MHz, C_6D_6) δ/ppm: -0.57, -9.80. UV-vis-NIR (THF) λ_{max}/nm (ε/M^{-1} cm^{-1}): 354 (20,200), 438 (14,000), 746 sh (21,400), 806 (24,400). MS(ESI+) m/z: 1386.75 (M+)

4.6 References

[1] Cooper, B. G.; Napoline, J. W.; Thomas, C. M. *Catal. Rev.* **2012**, *54*, 1–40.

[2] Hayashi, T.; Konishi, M.; Kobori, Y.; Kumada, M.; Higuchi, T.; Hirotsu, K. *J. Am. Chem. Soc.* **1984**, *106*, 158–163.

[3] Powers, D. C.; Ritter, T. *Nature Chemistry* **2009**, *1*, 302–309.

[4] Quebatte, L.; Scopelliti, R.; Severin, K. *Angew. Chem. Int. Ed. Engl.* **2004**, *43*, 1520–1524.

[5] Braune, W.; Okuda, J. *Angew. Chem. Int. Ed. Engl.* **2003**, *42*, 64–68.

[6] van den Beuken, E. K.; Feringa, B. L. *Tetrahedron* **1998**, *54*, 12985–13011.

[7] Krogman, J. P.; Foxman, B. M.; Thomas, C. M. *J. Am. Chem. Soc.* **2011**, *133*, 14582–14585.

[8] Yang, J. Y.; Bullock, R. M.; Shaw, W. J.; Twamley, B.; Fraze, K.; DuBois, M. R.; DuBois, D. L. *J. Am. Chem. Soc.* **2009**, *131*, 5935–5945.

[9] DuBois, D. L.; Bullock, R. M. *Eur. J. Inorg. Chem.* **2011**, 1017–1027.

[10] (a) Tye, J. W.; Darensbourg, M. Y.; Hall, M. B. *Inorg. Chem.* **2006**, *45*, 1552–1559. (b) Liu, T.; Darensbourg, M. Y. *J. Am. Chem. Soc.* **2007**, *129*, 7008–7009. (c) Rampersad, M. V; Jeffery, S. P.; Golden, M. L.; Lee, J.; Reibenspies, J. H.; Darensbourg, D. J.; Darensbourg, M. Y. *J. Am. Chem. Soc.* **2005**, *127*, 17323–17334. (d) Gloaguen, F.; Rauchfuss, T. B. *Chem. Soc. Rev.* **2009**, *38*, 100–108.

[11] Gavrilova, A. L.; Bosnich, B. *Chem. Rev.* **2004**, *104*, 349–383.

[12] Tanme, T.; Yun, J. W.; Lippard, S. J. *Inorg. Chem.* **1995**, *34*, 4220–4229.

[13] Herold, S.; Pence, L. E.; Lippard, S. J. **1995**, *117*, 6134–6135.

[14] Yun, J. W.; Tanase, T.; Pence, L. E.; Lippard, S. J. **1995**, *117*, 4407–4408.

[15] He, C.; Lippard, S. J. *J. Am. Chem. Soc.* **1998**, *120*, 105–113.

[16] Tanase, T.; Lippard, S. J. *Inorg. Chem.* **1995**, *34*, 4682–4690.

[17] Tanase, T.; Yun, J. W.; Lippard, S. J. *Inorg. Chem.* **1996**, *35*, 3585–3594.

[18] Sessler, J. L.; Tomat, E.; Mody, T. D.; Lynch, V. M.; Veauthier, J. M.; Mirsaidov, U.; Markert, J. T. *Inorg. Chem.* **2005**, *44*, 2125–2127.

[19] Bosnich, B. *Inorg. Chem.* **1999**, *38*, 2554–2562.

[20] (a) Girgis, A. Y.; Balch, A. L. *Inorg. Chem.* **1975**, *14*, 2724−7. (b) Simpson, C. L.; Boone, S. R.; Pierpont, C. G. **1989**, *28*, 4379–4385.

[21] Camacho-camacho, C.; Merino, G.; Martínez-Martínez, F. J.; Nöth, H.; Contreras, R. *Eur. J. Inorg. Chem.* **1999**, 1021–1027.

[22] Larsen, S. K.; Pierpont, C. G. *J. Am. Chem. Soc.* **1988**, *110*, 1827–1832.

[23] Bruni, S.; Caneschi, A.; Cariati, F.; Delfs, C.; Dei, A.; Firenze, U. *J. Am. Chem. Soc.* **1994**, *116*, 1388–1394.

[24] Mcgarvey, B. R.; Ozarowski, A.; Tian, Z.; Tuck, D. G. *Can. J. Chem.* **1995**, *73*, 1213–1222.

[25] Chaudhuri, P.; Hess, M.; Weyhermüller, T.; Wieghardt, K. *Angew. Chemie Int. Ed.* **1999**, *38*, 1095–1098.

[26] Zarkesh, R. A.; Ziller, J. W.; Heyduk, A. F. *Angew. Chem. Int. Ed.* **2008**, *47*, 4715–4718.

[27] Zarkesh, R. A.; Heyduk, A. F. *Organometallics* **2009**, *28*, 6629–6631.

[28] Wong, J. L.; Sánchez, R. H.; Logan, J. G.; Zarkesh, R. a.; Ziller, J. W.; Heyduk, A. F. *Chem. Sci.* **2013**, *4*, 1906–1910.

[29] Szigethy, Géza; Heyduk, A. *Dalton Trans.* **2012**, *41*, 8144–8152.

[30] Szigethy, G.; Shaffer, D. W.; Heyduk, A. F. *Inorg. Chem.* **2012**, *51*, 12606–12618.

[31] Hananouchi, S. P. MS Thesis, University of California, Irvine, 2014.

[32] Trans, D.; Addison, A. W.; Rao, T. N. *J. Chem. Soc. Dalt. Trans.* **1984**, 1349–1356.

[33] Allen, F. H.; Kennard, O.; Watson, D. G. *J. Chem. Soc. Perkin Trans. II* **1987**, S1–S19.

[34] Gütlich, P.; Bill, E.; Trautwein, A. X. *Mössbauer Spectroscopy and Transition Metal Chemistry*; Springer-Verlag: Berlin Heidelberg, 2011; p 85.

[35] Dey, A.; Ghosh, A. *J. Am. Chem. Soc.* **2002**, *124*, 3206–3207.

[36] de Oliveira, F. T.; Chanda, A.; Banerjee, D.; Shan, X.; Mondal, S.; Que, L. Jr.; Bominaar, E. L.; Münck, E.; Collins, T. J. *Science*, **2007**, *315*, 835–838.

[37] Grapperhaus, C. A.; Mienert, B.; Bill, E.; Weyhermüller; Wieghardt, K. *Inorg. Chem.*, **2000**, *39*, 5306–5317.

[38] Camacho-Camacho, C.; Mijangos, E.; Castillo-Ramos, M. E.; Esparza-Ruiz, A.; Vásquez-Badillo, A.; Nöth, H.; Flores-Parra, A.; Contreras, R. *J. Organomet. Chem.* **2010**, *695*, 833–840.

[39] I. S. Weitz and M. Rabinovitz *J. Chem. Soc. Perkin Trans.* **1993**, *1*, 117−120.

[40] APEX2, Version 2008.3-0 / 2.2-0, Bruker AXS, Inc.; Madison, WI 2007.

[41] SAINT Version 7.53a / 7.46a, Bruker AXS, Inc.; Madison, WI 2007.

[42] Sheldrick, G. M. *SADABS*, Version 2007/4, Bruker AXS, Inc.; Madison, WI 2007.

[43] Sheldrick, G. M. *SHELXTL*, Version 6.12; Brucker AXS, Inc.: Madison, WI, 2001.

[44] International Tables for X-Ray Crystallography 1992, Vol. C., Dordrecht: Kluwer Academic Publishers.

Chapter 5

Synthesis and Characterization of Homoleptic Chromium(III) Complexes Coordinated to Redox-Active ~-Diimine Ligands

5.1 Introduction

Over the past few decades, metal semiquinonate complexes containing redox-active dioxolene-type ligands have been of interest due to the unique electronic and magnetic properties imparted by the metal-ligand interactions.[1] Among many classic examples of these compounds, homoleptic tris-semiquinonate chromium(III) complexes are an ideal platform for these studies as six-coordinate chromium has a strong preference for the +3 oxidation state (Scheme 5.1).[1, 2, 3] These complexes display rich redox profiles and oftentimes complicated magnetic behaviors due to exchange coupling between the ligand-based radicals and the d^3 metal ion.[3] The diverse behavior of non-innocent ligands on the electronic properties of these complexes have bolstered the motivation for further investigations of ~-diimine ligands.

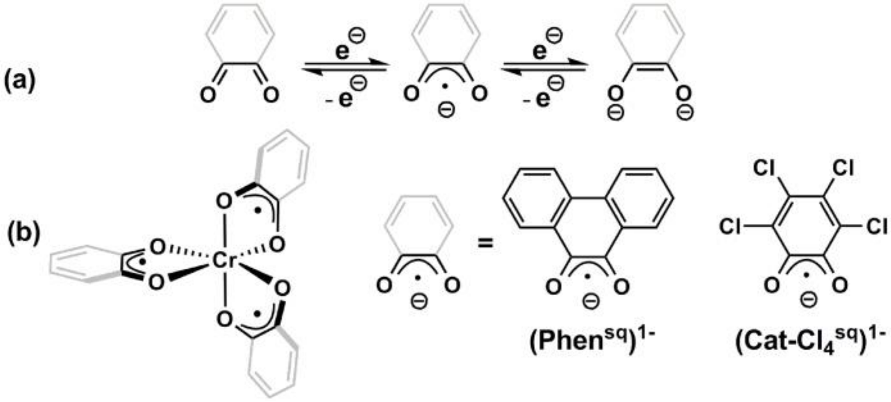

Scheme 5.1. (a) The three accessible oxidation states of dioxolene ligands. (b) Homoleptic tris-semiquinonate complexes of chromium(III).

While ~-diimines and dioxolenes share many similarities, they differ largely in the tunability of the structural and electronic properties of their complexes. Much like their dioxolene congeners, ~-diimines can also bind to octahedral metal centers in the bidentate coordination mode and in three different oxidation states.[4] This concept is portrayed through the *N,N'*-bis(aryl)acenapthenediimine (ar-ADI; ar = 3,5-dimethylphenyl) and *N,N'*-bis(aryl)phenanthrenediimine (ar-PDI; ar = 3,5-dimethylphenyl) ligand sets in Scheme 5.2.[5, 6] Unlike the dioxolenes, the steric properties of the diimine ligands can be modulated through changes to the organic group bound to the nitrogen donor atom, which in turn can influence the physical and redox profiles of their metal complexes as well as their reactivity.[7, 8] Furthermore, the replacement of oxygen with nitrogen results in a decrease in the electronegativity of the donor atoms, leading to anodic shifts in the redox potentials of the complex.

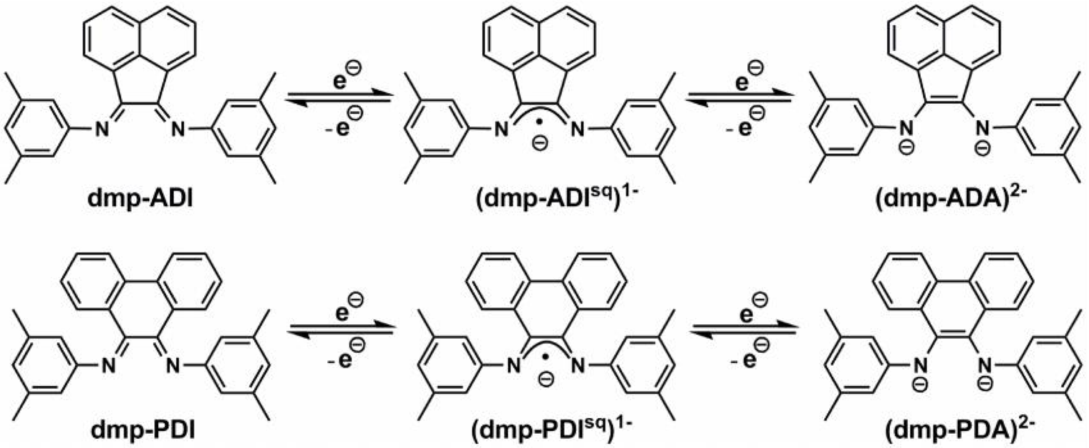

Scheme 5.2. Three accessible oxidation states of the (dmp-ADI) and (dmp-PDI) ligand scaffolds (dmp = 3,5-dimethylphenyl).

Recently, studies of chromium complexes containing singly-coordinated ~-diimine ligands have garnered interest due to their applications in polymer catalysis.[9, 10] Mu and coworkers have shown that upon activation with methylaluminumoxane (MAO), chromium(III) catalysts that contain (ar-PDI^{sq})$^{1-}$ ligands are able to perform isoprene polymerization, while those supported by (ar-ADI^{sq})$^{1-}$ exhibit high activities in isoprene and butadiene polymerization (Chart 5.1).[11, 12] Although the reactivity of chromium(III) complexes supported by (ar-PDI) and (ar-ADI) ligands have been explored, little is understood about the redox activity of these systems. Furthermore, there are virtually no investigations of homoleptic tris-iminosemiquinonate chromium(III) complexes of these ligand sets; studies which may be instrumental to enhancing our understanding of the reactivity of chromium complexes supported by non-innocent ligands.

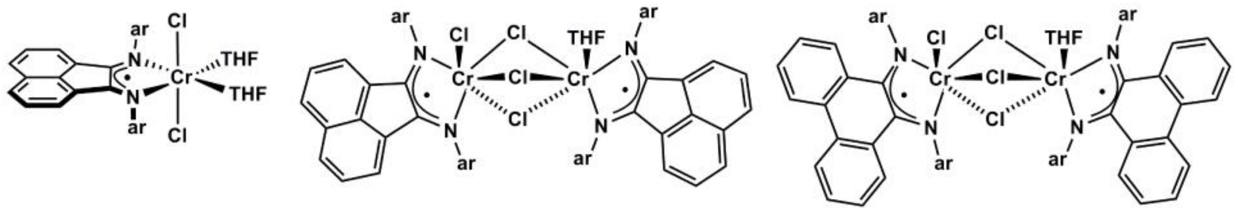

Chart 5.1. Chromium polymer catalysts containing (ar-ADI^{sq})$^{1-}$ and (ar-PDI^{sq})$^{1-}$ coordinated to single metal centers.

To further our fundamental understanding of chromium(III)–iminosemiquinonate complexes, we have become interested in studying how the nature of the backbone affects the redox activity of the ligand and overall metal-ligand electronic behaviors of such systems. Two homoleptic chromium(III) complexes have been prepared and characterized.[13] The (dmp-ADI) and (dmp-PDI) ligand sets, which differ mainly in the level of conjugation within the ligand scaffold (Scheme 5.2), comprise the current study.

5.2 Results

5.2.1 Synthesis and Structural Characterization of Homoleptic Chromium(III) Complexes

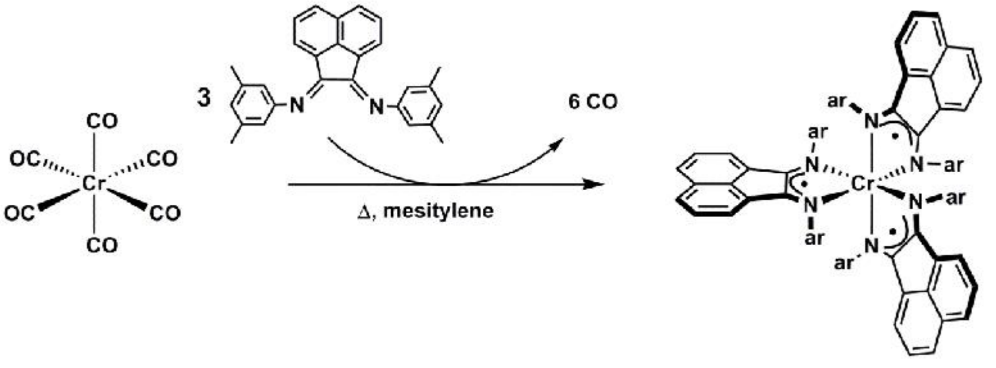

ar = 3,5-dimethylphenyl

14

Scheme 5.3. Synthesis of complex **14**.

Synthesis of the homoleptic chromium(III) compound Cr(dmp-ADI^{sq})$_3$ (**14)** was carried out through adapting known procedures (Scheme 5.3).[13] Heating to reflux for five days, a mesitylene solution containing one equivalent of Cr(CO)$_6$ and three equivalents of neutral *N*,*N'*-bis(3,5-dimethylphenyl)acenapthenediimine (dmp-ADI) resulted in release of the CO ligands and coordination of three (dmp-ADI) ligands to the metal center. Dark red crystals of **14** suitable for X-ray crystallography were grown from concentrated benzene solutions at ambient temperature.

The solid state structure of **14**, obtained from X-ray crystallography, provides an overall physical description of the complex to assist in assigning ligand and metal oxidation states. The solid-state structure of **14** is displayed as an ORTEP diagram in Figure 5.1 while Table 5.1 lists selected bond lengths and angles in the primary coordination sphere of chromium. The N(1A)−Cr(1)−N(1D), N(1B)−Cr(1)−N(1E), and N(1A)−Cr(1)−N(1B) angles of 172.29(2)°, 172.22(5)°, and 79.77(5)°, respectively, indicate that the chromium complex adopts a pseudo-octahedral geometry. Complex **14** crystallizes in a rhombohedral crystal lattice system and as a result, the asymmetric unit of **14** consists of one chromium metal bound to half a unit of (dmp-ADI). Consequently, all six C−N bonds have equi-length values of 1.326(2) Ǻ. This bond distance falls in the range typically reported for the C−N bond distances of complexes with (ar-ADI^{sq}) coordinated to chromium(III), as well as to alkali and alkaline-earth metals.[6, 12, 14, 15, 16] The backbone C−C bond length of 1.432(2) Ǻ is also consistent with the 1.41−1.43 Ǻ C−C bond distance range observed in chromium(III) and other metal complexes containing (ar-ADI^{sq}) ligands. These diagnostic bond measurements are indicative of the bidentate ligands adopting the (dmp-ADI^{sq})$^{1-}$ form. Thus, **14** can be assigned as a chromium(III) complex in which three monoanionic (dmp-ADI^{sq})$^{1-}$ ligands coordinate to the metal center.

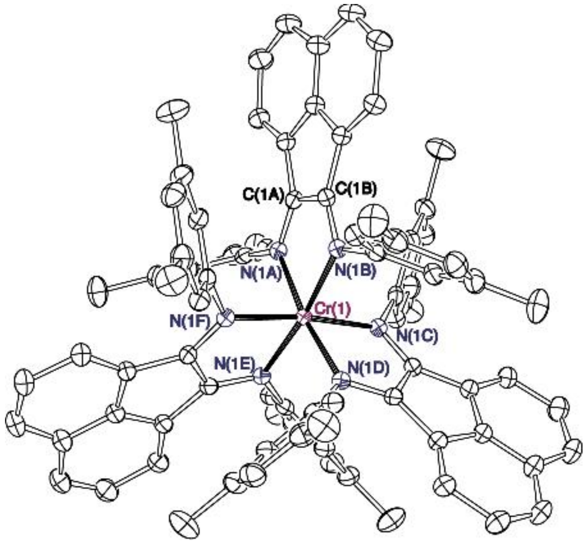

Figure 5.1. Crystal structure of **14**. Solvent molecules and hydrogen atoms are removed for clarity. Thermal ellipsoids are drawn at 50% probability.

Table 5.1. Selected bond lengths (Å) and angles (°) of **14**.

Bond	Lengths	Bond	Angle
C(1A)–N(1A)	1.326(2)	N(1B)–Cr(1)–N(1E)	172.22(5)
C(1A)–C(1B)	1.432(2)	N(1A)–Cr(1)–N(1B)	79.77(5)
Cr(1)–N(1A)	2.030(1)	N(1A)–Cr(1)–N(1D)	172.29(5)
		N(1A)–Cr(1)–N(1C)	94.71(5)
		N(1A)–Cr(1)–N(1E)	94.68(6)
		N(1A)–Cr(1)–N(1F)	91.18(6)

Coordination of three *N,N'*-bis(3,5-dimethylphenyl)phenanthrenediimine (dmp-PDI) ligands to chromium proceeded through metathesis reaction using a chromium(III) salt (Scheme 5.4). Initial attempts to prepare Cr(dmp-PDI^{sq})$_3$ (**15**) through heating to reflux in toluene or anisole solutions containing $Cr(CO)_6$ and three equivalents of (dmp-PDI) led to recovery of free diimine ligands in high yield. Hence, a different route was developed using chromium(III) and lithiated iminosemiquinonate starting materials. Upon treating *N,N'*-bis(3,5-dimethylphenyl)phenanthrenediamine (dmp-PDA) with two equivalents of *n*-butyllithium, the *in situ* generated dark red solution of Li$_2$(dmp-PDA) was reacted with one equivalent of the neutral (dmp-PDI) to produce Li(dmp-PDI^{sq}) via comproportionation. Addition of $CrCl_3(THF)_3$ to the dark green mixture led to a dark red solution containing **15,** which was isolated in 58% yield. Single crystals of **15** suitable for X-ray crystallography were obtained at −35 °C by the diffusion of acetonitrile into a toluene solution of the chromium complex.

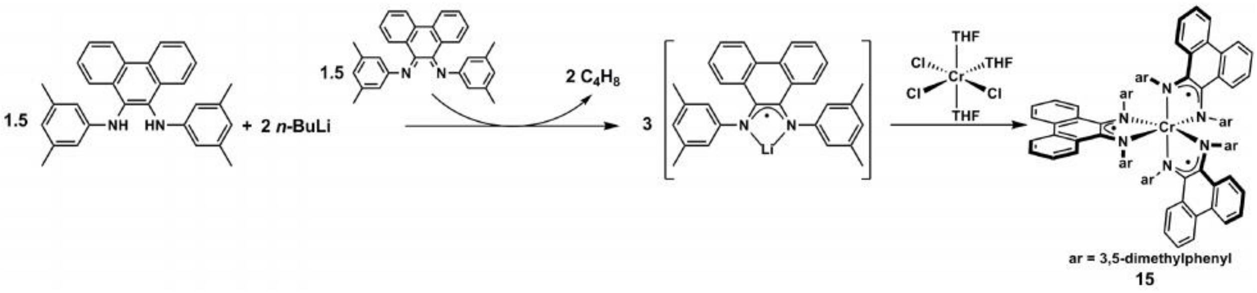

Scheme 5.4. Synthesis of complex **15**.

The structural properties of **15** are investigated through X-ray crystallography in order to help determine the ligand and metal oxidation states. Similar to the (dmp-ADI^{sq}) analogue, the geometry at the chromium center of **15** is best described as pseudo-octahedral, as evidenced by the N(1)–Cr(1)–N(3), N(2)–Cr(1)–N(6), and N(1)–Cr(1)–N(2) angles of 171.44(7)°, 171.75(7)°, and 76.25(7)°, respectively. All three backbone carbon−carbon bond lengths (1.43−1.44 Å) are consistent with those observed in other chromium(III) compounds containing (ar-PDI^{sq}) ligands.[11] The C−N bond distances of **15** are between 1.34−1.35 Å. The reported C−N bond distances of the (ar-PDI^{sq}) coordinated to chromium(III) centers are in the range of 1.35−1.46 Å. Carbon−nitrogen bond distances of 1.32−1.35 Å have also been described in the literature for chromium(III) complexes containing iminosemiquinonate ligands with varying backbone topologies.[10, 16] An examination of these diagnostic bond lengths suggest that all three bidentate ligands of complex **15** adopt the (dmp-PDI^{sq})$^{1-}$ form. Chelation of three monoanionic ligands to the metal center, therefore, indicates that **15** possesses a chromium(III) center.

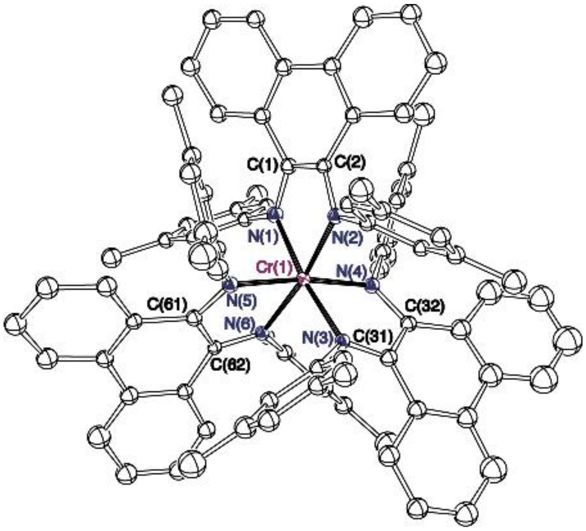

Figure 5.2. Crystal structure of **15**. Solvent molecules and hydrogen atoms are removed for clarity. Thermal ellipsoids are drawn at 50% probability.

Table 5.2. Selected bond lengths (Å) and angles (°) of **15**.

Bond	Lengths	Bond	Lengths	Bond	Angle
C(1)–C(2)	1.438(3)	Cr(1) –N(1)	2.032(2)	N(1)–Cr(1)–N(3)	171.75(7)
C(1)–N(1)	1.349(3)	Cr(1) –N(2)	2.036(2)	N(2)–Cr(1)–N(6)	171.44(7)
C(2)–N(2)	1.347(3)	Cr(1) –N(3)	2.037(2)	N(1)–Cr(1)–N(2)	76.25(7)
C(31)–C(32)	1.434(3)	Cr(1) –N(4)	2.036(2)	N(1)–Cr(1)–N(4)	97.44(7)
C(31)–N(3)	1.347(3)	Cr(1) –N(5)	2.041(2)	N(1)–Cr(1)–N(5)	88.40(7)
C(32)–N(4)	1.343(3)	Cr(1) –N(6)	2.034(2)	N(1)–Cr(1)–N(6)	97.50(7)
C(61)–C(62)	1.436(4)				
C(61)–N(5)	1.347(3)				
C(62)–N(6)	1.342(2)				

5.2.2 Magnetism and Spectroscopic Comparisons of Chromium(III) Complexes

The electronic spectra of **14** and **15** further support the presence of Cr(III) centers in both systems. For both complexes, the visible region is dominated by two absorptions (Figure 5.3). Intraligand transitions for complexes **14** and **15** are observed at 508 nm and 482 nm, respectively. The bands at 572 nm for **14** and 566 nm for **15** have the energy expected for the $^4A_{2g} \rightarrow {}^2E_g$ spin-forbidden d–d transitions in d^3 compounds; [17] however, the observed molar extinction coefficients for such transitions are larger than usual. The enhanced intensity can be ascribed to coupling between the metal-based electrons and the ligand-based radicals.[18] The absorption features of **14** and **15** support the argument that both are chromium(III) complexes.

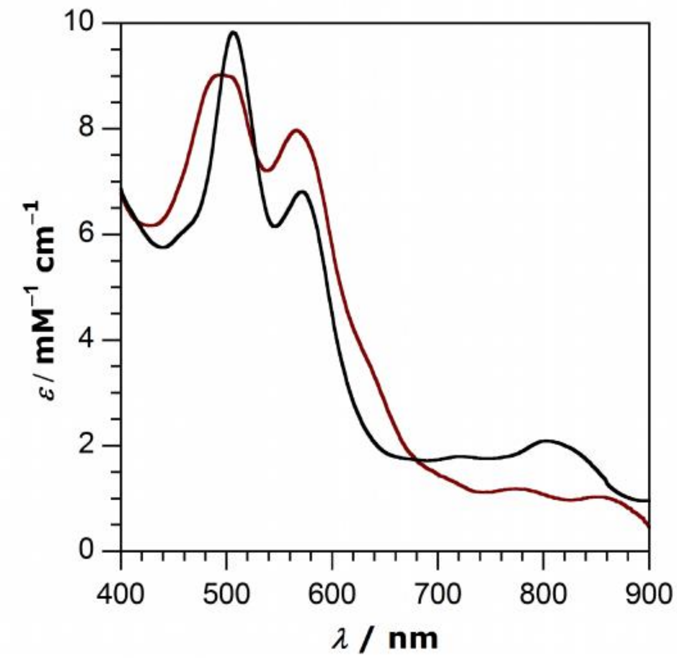

Figure 5.3. Absorption spectra of Cr(dmp-ADI^{sq})$_3$ (**14**; black) and Cr(dmp-PDI^{sq})$_3$ (**15**; red) collected in THF.

EPR spectroscopy is also employed to interrogate the electronic properties of **14** and **15**. At 298 K, the EPR spectrum of complex **14** reveals a nine-line isotropic signal centered at g = 2.00 (Figure 5.4). These hyperfine splittings are due to coupling of a singly-unpaired electron to six equivalent ^{14}N nuclei (I = 1, 99.63%, A_N = 1.46 mT). In addition, weak satellite peaks arising from coupling to ^{53}Cr nuclei (I = $\frac{3}{2}$, 9.6%, A_{Cr} = 4.41 mT) are also observed.[19] Upon cooling to 77 K, a broad isotropic signal was observed. Hyperfine coupling patterns have also been observed at ambient temperatures in various main-group complexes containing (ar-ADI^{sq})$^{1-}$ ligands, wherein the unpaired electron residing in each ligand is coupled to the nuclei of the ^{14}N and the coordinated main-group element.[6, 15] Thus, the EPR spectrum of **14** unequivocally supports the contention that each (dmp-ADI) moiety surrounding the chromium center contains a radical that resides in the ligand. In contrast, at room temperature complex **15** is EPR silent while at 77 K, an axial resonance with g = 1.98 and 2.01 is observed (Figure 5.5), consistent with a metal-based $S = \frac{1}{2}$ system and indicative of a low-spin Cr(III) species.

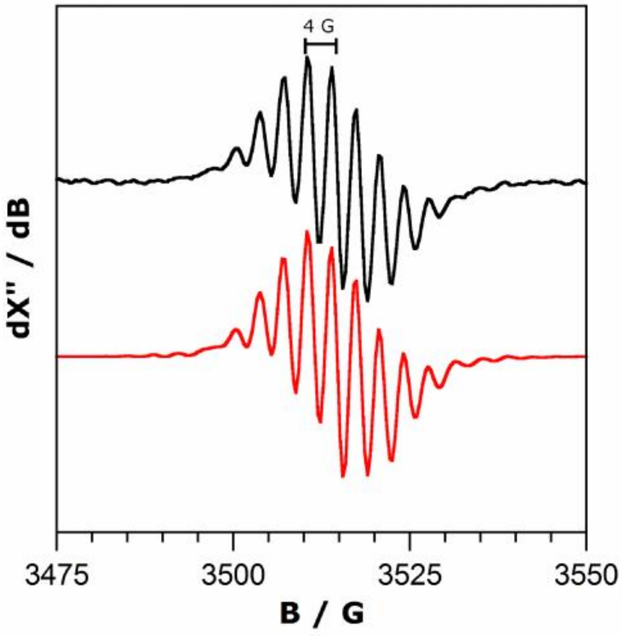

Figure 5.4. X-band EPR spectra of Cr(dmp-ADI^{sq})$_3$ (**14**; black) and simulation (red). Experimental conditions: $B_1 \perp B_0$; solvent, THF; temperature, 298 K.

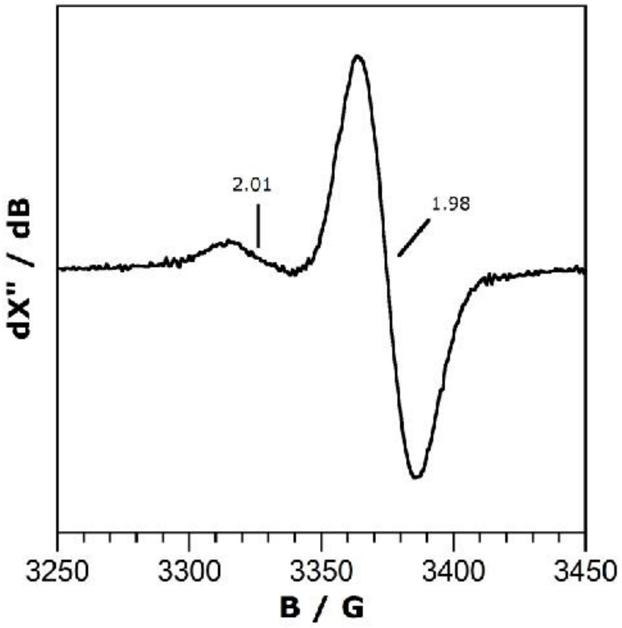

Figure 5.5. X-band EPR spectra of Cr(dmp-PDI^{sq})$_3$ (**15**). Experimental conditions: $B_1 \perp B_0$; solvent, THF; temperature, 77 K.

The observed differences displayed in the EPR spectra of **14** and **15** prompted our interests in exploring their magnetic properties. An Evans' method measurement of **14** at ambient temperature provided a magnetic moment («$_{eff}$) value of 1.18 «B, similar to what has been observed for Cr(Phen^{sq})$_3$ (1.15 «B) and Cr(Cat-Cl$_4$^{sq})$_3$ (1.08 «B).[3] On the other hand, when magnetic measurements of **15** were performed under comparable conditions, the ^{1}H NMR spectrum displayed little to no separations between the resonance belonging to the solution containing the paramagnetic analyte and that of the isolated standard. The results of these measurements suggest that both complexes exhibit varying degrees of intramolecular anti-ferromagnetic coupling often observed in other chromium(III) tris-semiquinonate complexes.[3]

5.2.3 Electrochemical Studies of Chromium(III) Complexes

To investigate the redox properties of Cr(dmp-ADI^{sq})$_3$ (**14**) and Cr(dmp-PDI^{sq})$_3$ (**15**), cyclic and differential pulse voltammetric techniques have been applied (Figure 5.6). As indicated in Table 5.3, overall, the redox events of **15** occur at more positive potentials as compared to those of **14**. Each complex displays three reversible redox couples relevant to the cationic series of the respective chromium compounds. However, differences in the reduction events, which pertain to the anionic series of the chromium compounds, are observed between the two complexes. While all three reduction events of Cr(dmp-ADI^{sq})$_3$ are reversible, one reversible and two irreversible reductions are present for the (dmp-PDI^{sq}) counterpart. The six redox processes of each chromium compound are likely ligand-based, as three oxidation and three reduction events have also been observed for the dioxolene congener Cr(Phen^{sq})$_3$ (Table 5.3).[2c] In contrast to Cr(Phen^{sq})$_{3,}$ the redox potentials of **14** and **15** are more negative, in agreement with the lower electrophilic character of the nitrogen-containing semiquinonate ligands.

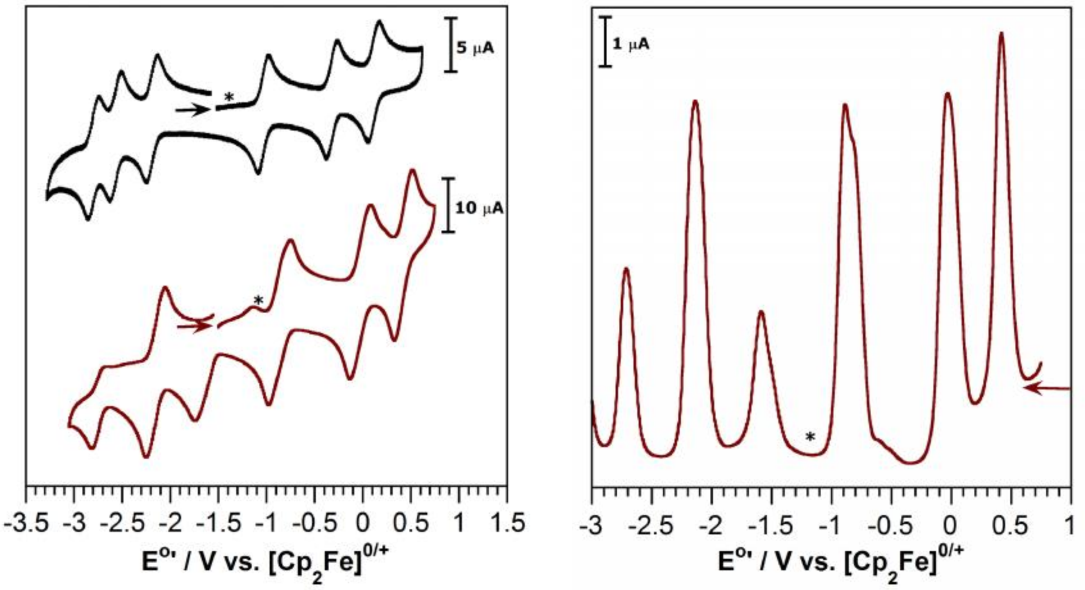

Figure 5.6. Cyclic voltammograms (*left*) of Cr(dmp-ADI^{sq})$_3$ (**14**; black) and Cr(dmp-PDI^{sq})$_3$ (**15**; red) and differential pulse voltammogram (*right*) of **15**. Bulk of the material denoted by *. Voltammograms were recorded at 1mM analyte concentration in 0.10 M [^{n}Bu$_4$N][PF$_6$] in THF using a glassy carbon working electrode, Pt wire counter electrode, Ag$^{0/+}$ wire reference, and scan rate of 200 mV/s at 298 K.

Table 5.3. Redox potentials vs. [Cp$_2$Fe]$^{0/+}$ for Cr(dmp-ADI^{sq})$_3$ (14) and Cr(dmp-PDI^{sq})$_3$ (15).[a]

Redox Couple	14	15	Cr(Phen^{sq})$_3$ [c]
2+ / 3+	0.12	0.42	0.68
1+ / 2+	–0.33	–0.03	0.54
0 / 1+	–1.08	–0.87	0.35
1^- / 0	–2.19	–1.56[b]	–0.62
2^- / 1^-	–2.58	–2.15	–0.95
3^- / 2^-	–2.81	–2.75[b]	–1.38

[a] Experimental conditions are detailed in Figure 5.6. [b] Irreversible process. [c] Potentials converted from E°' vs. SCE to E°' vs. [Cp$_2$Fe]$^{0/+}$. Data obtained from Ref. 2c.

5.3 Discussion

5.3.1 Ligand and Metal Oxidation State Assignments

Intramolecular charge distribution is a commonly observed entity in metal complexes containing non-innocent ligands and as such, ligand and metal oxidation state determinations are often convoluted. In order to make such assignments, a battery of analytical techniques must be applied. Structural data obtained from X-ray diffraction experiments establish that the (3,5-dmp ADI) and (3,5-dmp PDI) ligand scaffolds of **14** and **15**, respectively, are in their monoanionic iminosemiquinonate forms. The EPR spectrum of **14** also ascertains that a radical is localized in the acenapthenediimine ligand. Chelation of three monoanionic ligands to each chromium center, therefore, suggests that the metal center oxidation state is +3. This contention is further supported by UV-vis spectroscopy wherein the absorption bands at 572 nm and 566 nm for complexes **14** and **15**, correspondingly, pertain to metal-ligand interactions of Cr(III) complexes containing ligand-based radicals.[17] These measurements establish that complexes **14** and **15** are formally chromium(III) compounds supported by π radical iminosemiquinonate ligands.

5.3.2 Redox Properties of Chromium(III) Complexes

Although the metal center coordination environments are very similar for Cr(dmp-ADI^{sq})$_3$ (**14**) and Cr(dmp-PDI^{sq})$_3$ (**15**), the differences in their ligand backbones have significant impacts on their electronic profiles. Whereas the phenanthrene moiety of (3,5-dmp PDI) is aromatic when fully reduced, the acenapthene moiety of (3,5-dmp ADI) is anti-aromatic in its diamide form (Scheme 5.2). Therefore, it should be easier to reduce and harder to oxidize (3,5-dmp PDI^{sq})$^{1-}$ in comparison to (3,5-dmp ADI^{sq})$^{1-}$. This proposal is in agreement with the results of electrochemical studies wherein the redox potentials of **15** are generally shifted more positive as compared to those of **14**.

Based on the electrochemical data of complexes **14** and **15**, the neutral tris-iminosemiquinonate chromium(III) complexes are capable of supporting multi-electron oxidation and reduction reactions without formal oxidation state changes at the metal centers (Scheme 5.5). Successive additions of three single electrons to Cr(ISQ)$_3$ generate the molecular monoanionic, dianionic, and trianionic complexes in which the iminosemiquinonate ligands act as the electron acceptors. Sequential oxidations of Cr(ISQ)$_3$ produce the singly-, doubly-, and triply-oxidized species wherein the ligands act as electron donors. These redox series are akin to those of chromium(III) tris-semiquinonate complexes containing dioxolene-type ligands.[2c]

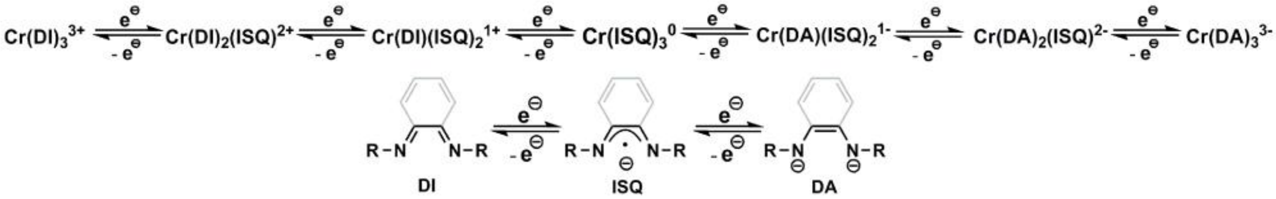

Scheme 5.5. Redox series of tris-iminosemiquinonate complexes of chromium(III).

5.4 Summary and Conclusion

Complexes **14** and **15** display clear differences in their electronic properties likely stemming from differences in the diimine ligand backbones. The electrochemical activity of both chromium complexes conform with the view that the phenanthrenediimine moiety is more difficult to oxidize but easier to reduce than the acenapthenediimine moiety. However, further investigations are required in order to completely understand the unique behaviors of such complexes, both of which apparently exhibit intramolecular anti-ferromagnetic properties.

5.5 Experimental

General Procedures. All compounds and reactions reported below require manipulations to be carried out under air- and moisture-free conditions using standard glovebox techniques or Schlenk techniques. Solvents were sparged with argon and then deoxygenated and dried by passage through Q5 and activated alumina columns, respectively. To test for effective oxygen and water removal, solvents were treated with a few drops of a purple solution of sodium benzophenone ketyl in THF. The C_6D_6 NMR solvent was dried in sodium-potassium amalgam benzophenone ketyl for two days, followed by trap-to-trap vacuum distillation and several freeze-pump-thaw cycles. Mesitylene was dried by heating at reflux in the presence of sodium benzophenone before being distilled into Straus flasks and degassed through several freeze-pump-thaw cycles. The ligands *N*,*N'*-bis(3,5-dimethylphenyl)acenapthenediimine (dmp-ADI),[20] *N*,*N'*-bis(3,5-dimethylphenyl)phenanthrenediimine (dmp-PDI), [21] and *N*,*N'*-bis(3,5-dimethylphenyl)phenanthrenediamine (dmp-PDA)[5a, 21] were synthesized according to published procedures. The $CrCl_3(THF)_3$ (Strem), $Cr(CO)_6$ (Alfa-Aesar), and *n*-butyl lithium (Alfa-Aesar) were used without further purification.

Physical Measurements. The UV-vis spectra were recorded with Perkin–Elmer Lambda 800 Spectrometer as solutions in toluene, THF or pyridine. Electrospray ionization mass spectrometry MS(ESI) was performed at the Mass Spectrometry Facility at University of California, Irvine. NMR spectra were acquired on a Bruker Avance 400/500/600 MHz spectrometer. Perpendicular-mode X-band EPR spectra were collected using Bruker EMX spectrometer equipped with ER041XG microwave bridge. Elemental analysis experiments have been performed on all new compounds, and the results of those that fall in the expected mass ranges are reported.

Electrochemical Methods. Cyclic voltammograms were collected using Gamry Series G 300 potentiostat/galvanostat/ZRA (Gamry Instruments, Warminster, PA) inside a nitrogen-filled glovebox. A glassy carbon working electrode (3.0 mm), platinum wire counter electrode, and silver wire reference electrode were used. Sample concentrations were 1.0 mM in THF with 0.10 M tetrabutylammonium hexafluorophosphate as the supporting electrolyte. All potentials are referenced to $[Cp_2Fe]^{+/0}$ using $(Cp^*)_2Fe$ and Cp_2Fe as internal standards. Decamethylferrocene (Acros) and ferrocene (Acros) were purified by sublimation under reduced pressure. Tetrabutylammonium hexafluorophosphate (Acros) was recrystallized from ethanol three times and dried in the oven before use.

Crystallographic Methods. X-ray diffraction data were collected on crystals mounted on glass fibers using a Bruker CCD platform diffractometer equipped with a CCD detector. Measurements were carried out using Mo K_α (λ = 0.71073 Å) radiation, which was wavelength selected with a single-crystal graphite monochromator. A full sphere of data was collected for each crystal structure. The APEX2 program package was used to determine unit-cell parameters and to collect data.[22] The raw frame data were processed using SAINT[23] and SADABS[24] to yield the reflection data files. Subsequent calculations were carried out using the SHELXTL[25] program suite. Structures were solved by direct methods and refined on F^2 by full-matrix least-squares techniques to convergence. Analytical scattering factors for neutral atoms were used throughout the analyses. Hydrogen atoms, though visible in the difference Fourier map, were generated at calculated positions and their positions refined using the riding model. ORTEP diagrams were generated using ORTEP-3 for Windows[26] and all thermal ellipsoids are drawn at the 50% probability level.

Table 5.4. X-ray diffraction data-collection and refinement parameters for complexes **14** and **15**.

	14•(C_6H_6)	**15**•3(C_7H_8)
Empirical formula	$C_{84}H_{72}N_6Cr$•(C_6H_6)	$C_{90}H_{78}$ N_6Cr•3(C_7H_8)
Formula weight	1295.58	1571.98
Crystal system	Rhombohedral	Triclinic
Space group	$R\bar{3}c$	$P\bar{1}$
T	88(2) K	133(2) K
a	13.1416(5) Å	13.2313(7) Å
b	23.1416(5) Å	13.3926(7) Å
c	70.675(3) Å	25.6445(14) Å
α	90°	79.8351(7)°
β	90°	84.4156(8)°
γ	120°	70.6054(7)°
V	10570.4(7) $Å^3$	4215.4(4) $Å^3$
Z	6	2
Reflections collected	35656	46400
data/restraints/parameters	2389 / 0 / 150	17199 / 0 / 1014
R1 [$I > 2\sigma(I)$][a]	0.0380	0.0522

wR2 (all data)[a]	0.1127	0.1414
GOF[a]	1.054	1.021

[a] $R1 = \Sigma||F_o| - |F_c||/\Sigma|F_o|$; $wR2 = [\Sigma[w(F_o^2 - F_c^2)^2]/\Sigma[w(F_o^2)^2]]^{1/2}$; $GOF = [\Sigma w(|F_o| - |F_c|)^2/(n - m)]^{1/2}$

Synthesis of Cr(dmp-ADI)$_3$ (14). Dry mesitylene was transferred via cannula into a Schlenk flask containing 3.10 g of dmp-ADI (7.98 mmol, 3.5 equiv.) and 502 mg of $Cr(CO)_6$ (2.28 mmol, 1 equiv). The dark red solution was heated at reflux under argon for 5 days to afford a dark purple solution. Solvent was removed via distillation under vacuum to reveal dark purple solids which were then washed with pentane. Yield: 1.73 g (62 %). UV-vis (THF) λ_{max}/nm (ε/ $M^{-1}cm^{-1}$): 508 (8,600), 572 (6,200), 804 (2,100), 960 (1,200), 1116 (1,400). MS(ESI+) m/z: 1217.60 (M+).

Synthesis of Cr(dmp-PDI)$_3$ (15). A THF solution containing 83.6 mg of dmp-PDA (0.200 mmol, 1.5 equiv.) was cooled at 77 K. To the cold orange solution, diethyl ether solutions of *n*-butyl lithium (0.400 mmol, 3 equiv.) was added and the resulting dark red solution stirred at ambient temperature for 1 hour, after which the mixture was cooled at 77 K. To the cold dark red mixture, 82.1 mg of dmp-PDI (0.197 mmol, 1.5 equiv.) was added at room temperature. After reacting for 2 hours, the resulting dark green lithiated semiquinonate mixture was once again cooled at 77 K. Subsequent addition of $CrCl_3(THF)_3$ at warmer temperatures produced a dark red solution that was stirred overnight (>12 hours) after which the mixture was placed under vacuum to remove the volatiles. The dark red product was then extracted with 25 mL of toluene and the solid byproducts were removed by filtration. Upon concentrating the dark red filtrate to one-quarter volume, acetonitrile was added and the resulting dark red mixture was cooled overnight at 238 K to produce dark microcrystalline solids. Yield: 100.5 mg (58%). UV-vis (THF) λ_{max}/nm (ε/ $M^{-1}cm^{-1}$): 566 (6,100), 490 (5,000). MS(ESI+) m/z: 1296.58 (MH+).

5.6 References

[1] (a) Pierpont, C. G. *Coord. Chem. Rev.* **2001**, *221*, 415–433. (b) Pierpont, C. G.; Buchanan, R. M. *Coord. Chem. Rev.* **1981**, *38*, 45–87.

[2] (a) Pierpont, C. G.; Downs, H. H.; Rukavina, T. G. *J. Am. Chem. Soc.* **1974**, *96*, 5573–5574. (b) Buchanan, R. M.; Downs, H. H.; Shorthill, W. B.; Pierpont, C. G.; Kessel, S. L.; Hendrickson, D. N. *J. Am. Chem. Soc.* **1978**, *100*, 4318–4320. (c) Downs, H. H.; Buchanan, R. M.; Pierpont, C. G. *Inorg. Chem.* **1979**, *18*, 1736–1740. (d) Chang, H.; Ishii, T.; Kondo, M.; Kitagawa, S. *J. Chem. Soc. Dalton Trans.* **1999**, 2467–2476.

[3] (a) Buchanan, R. M.; Kessel, S. L.; Downs, H. H.; Pierpont, C. G.; Hendrickson, D. N. *J. Am. Chem. Soc.* **1978**, *100*, 7894–7900. (b) Pierpont, C. G. *Inorg. Chem.* **2001**, *40*, 5727–5728.

[4] Caulton, K. G. *Eur. J. Inorg. Chem.* **2012**, *2012*, 435–443.

[5] (a) Ketterer, N. A.; Ziller, J. W.; Rheingold, A. L.; Heyduk, A. F. *Organometallics* **2007**, *26*, 5330–5338. (b) Shaffer, D. W.; Ryken, S. A.; Zarkesh, R. A.; Heyduk, A. F. *Inorg. Chem.* **2011**, *50*, 13–21.

[6] Hill, N. J.; Vargas-Baca, I.; Cowley, A. H. *Dalton Trans.* **2009**, *9226*, 240–253.

[7] (a) Clark, K. M.; Ziller, J. W.; Heyduk, A. F. *Inorg. Chem.* **2010**, *49*, 2222–2231. (b) Clark, K. M.; Bendix, J.; Heyduk, A. F.; Ziller, J. W. **2012**, *3*, 7457–7459.

[8] Gonsalvi, L.; Gaunt, J. A.; Adams, H.; Castro, A.; Sunley, G. J.; Haynes, A. *Organometallics* **2003**, *22*, 1047–1054.

[9] (a) Kim, W.; Fevola, M. J.; Liable-sands, L. M.; Rheingold, A. L.; Theopold, K. H. *Organometallics* **1998**, *17*, 4541–4543. (b) Macadams, L. A.; Kim, W.; Liable-sands, L. M.; Guzei, I. A.; Rheingold, A. L.; Theopold, K. H. *Organometallics* **2002**, *21*, 952–960. (c) MacAdams, L. A.; Buffone, G. P.; Incarvito, C. D.; Rheingold, A. L.; Theopold, K. H. *J. Am. Chem. Soc.* **2005**, *127*, 1082–1083.

[10] (a) Kreisel, K. A.; Yap, G. P. A.; Theopold, K. H. *Inorg. Chem.* **2008**, *47*, 5293–5303. (b) Kreisel, K. A.; Yap, G. P. A.; Theopold, K. H. *Eur. J. Inorg. Chem.* **2012**, *2012*, 520–529.

[11] Gao, B.; Luo, X.; Gao, W.; Huang, L.; Gao, S.; Liu, X.; Wu, Q.; Mu, Y. *Dalton Trans.* **2012**, *41*, 2755–2763.

[12] Gao, B.; Gao, W.; Wu, Q.; Luo, X.; Zhang, J.; Su, Q.; Mu, Y. *Organometallics* **2011**, *30*, 5480–5486.

[13] Clark, K. M. Ph.D. Dissertation, University of California, Irvine, 2010.

[14] Fedushkin, I. L.; Skatova, A. A.; Chudakova, V. A.; Fukin, G. K. *Angew. Chem. Int. Ed. Engl.* **2003**, *42*, 3294–3298.

[15] (a) Evans, D. A.; Cowley, A. H. *J. Am. Chem. Soc.* **2012**, *134*, 15672–15675. (b) Fedushkin, I. L.; Skatova, A. A.; Chudakova, V. A.; Cherkasov, V. K.; Fukin, G. K.; Lopatin, M. A. *Eur. J. Inorg. Chem.* **2004**, *2004*, 388–393.

[16] Fedushkin, I. L.; Makarov, V. M.; Sokolov, V. G.; Fukin, G. K. *Dalton Trans.* **2009**, *2*, 8047–8053.

[17] (a) Ghosh, M.; Sproules, S.; Weyhermüller, T.; Wieghardt, K. *Inorg. Chem.* **2008**, *47*, 5963–5970. (b) Spikes, G. H.; Sproules, S.; Bill, E.; Weyhermüller, T.; Wieghardt, K. *Inorg. Chem.* **2008**, *47*, 10935–10944. (c) Buchanan, R. M.; Claflin, J.; Pierpont, C. G. *Inorg. Chem.* **1983**, *22*, 2552–2556. (d) Sokolowski, A.; Bothe, E.; Bill, E.; Weyhermüller,T.; Wieghardt, K. *Chem. Commun.* **1996**, 1671–1672.

[18] (a) Benelli, C.; Dei, A.; Gatteschi, D.; Gudell, H. U.; Pardi, L. *Inorg. Chem.* **1989**, *28*, 3089–3091. (b) Tsukahara, Y.; Kamatani, T.; Iino, A.; Suzuki, T.; Kaizaki, S. *Inorg. Chem.* **2002**, *41*, 4363–4370.

[19] Fujii, H.; Yoshimura, T.; Kamada, H. *Inorg. Chem.* **1997**, *36*, 1122–1127.

[20] Gasperini, M.; Ragaini, F.; Cenini, S. *Organometallics* **2002**, *21*, 2950.

[21] Ketterer, N. A. PhD. Dissertation, University of California, Irvine, 2008.

[22] APEX2, Version 2008.3-0 / 2.2-0, Bruker AXS, Inc.; Madison, WI 2007.

[23] SAINT Version 7.53a / 7.46a, Bruker AXS, Inc.; Madison, WI 2007.

[24] Sheldrick, G. M. *SADABS*, Version 2007/4, Bruker AXS, Inc.; Madison, WI 2007.

[25] Sheldrick, G. M. *SHELXTL*, Version 6.12; Brucker AXS, Inc.: Madison, WI, 2001.

[26] International Tables for X-Ray Crystallography 1992, Vol. C., Dordrecht: Kluwer Academic Publishers.

Appendix

Synthesis of *N,N'*-bis-(3-adamantylamino-propyl)-4,5-dimethoxy-benzene-1,2-diamine ($[^{Ad}N_2N_2]H_2$)

The preparation of *N,N'*-bis-(3-adamantylamino-propyl)-4,5-dimethoxy-benzene-1,2-diamine ($[^{Ad}N_2N_2]H_2$) was adapted from synthetic procedures for *N,N'*-bis-(3-dimethylamino-propyl)-4,5-dimethoxy-benzene-1,2-diamine ($[^{Me}N_2N_2]H_2$).[1] As described in Scheme A.1, heating to reflux a methanol solution of the $[N_2Cl_2]H_2$ precursor with excess dimethylamine hydrochloride and potassium carbonate provided $[^{Me}N_2N_2]H_2$ in high yield. However, under comparable conditions, reaction of $[N_2Cl_2]H_2$ with 2.5 equivalents of adamantylamine resulted in recovery of free amine in considerable yields. When the reaction was carried out in the presence of stronger bases, such as KOH or NaH, formation $[^{Ad}N_2N_2]H_2$ was still not observed.

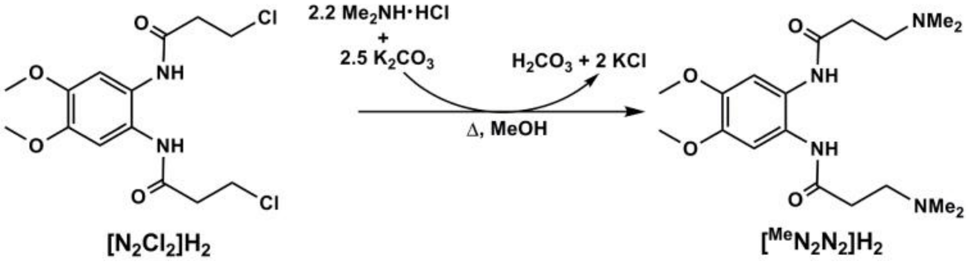

Scheme A.1. Synthesis of $[^{Me}N_2N_2]H_2$.

To increase the driving force for installing the adamantylamide, it was hypothesized the use of a better leaving group would be necessary. Hence, $[N_2I_2]H_2$ was used as a precursor in place of $[N_2Cl_2]H_2$ (Scheme A.2). Interestingly, when the reaction mixture was heated to reflux in methanol overnight, the product formed appeared to be $[N_2(OMe)_2]H_2$ based on ^1H NMR spectral analysis. Under similar conditions, $[N_2(OMe)_2]H_2$ was also isolated when $[N_2Cl_2]H_2$ and 2.2 equivalents of NaI were used as starting materials.

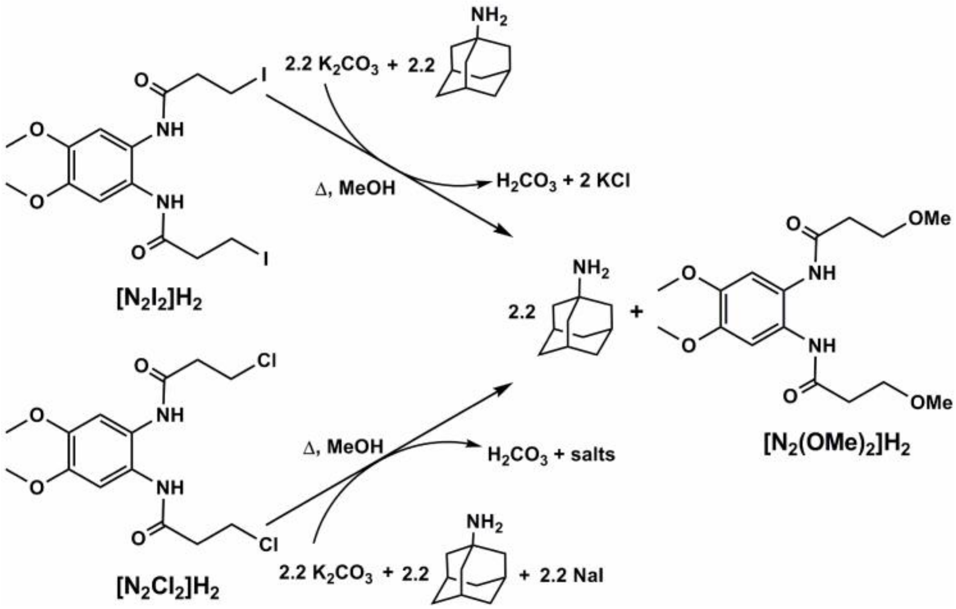

Scheme A.2. Attempts to prepare $[^{Ad}N_2N_2]H_2$ leading to formation of $[N_2(OMe)_2]H_2$.

Ultimately, it was discovered that treatment of the $[N_2Cl_2]H_2$ synthon in THF with excess adamantylamine and catalytic amounts of NaI was necessary to furnish the desired product $[^{Ad}N_2N_2]H_2$ (Scheme A.3). When either 2.2 or five equivalents of adamantylamine were employed, asymmetric products were observed by ^{1}H NMR. In contrast, the use of ten equivalents of adamantylamine generated a fully aminated $[^{Ad}N_2N_2]H_2$. However, separation of the excess amine precursor from $[^{Ad}N_2N_2]H_2$ proved challenging. Due to their similar solubilities, isolation of the desired product via solvent extractions or recrystallization were unsuccessful. Because their polar and basic properties were very alike, purification by column chromatography was also difficult to achieve. Thus far, the most effective technique for removing the free adamantylamine was through sublimation, although significant amounts of the free amine was still present in the final product mixture.

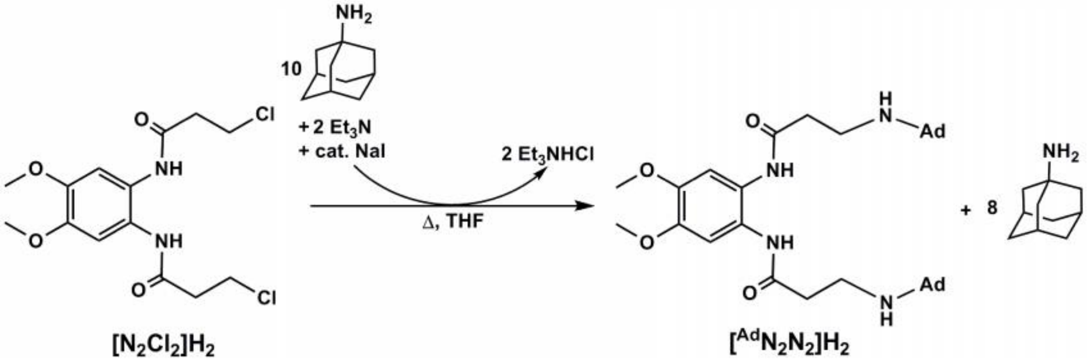

Scheme A.3. Synthesis of $[^{Ad}N_2N_2]H_2$.

Experimental

Synthesis of $[^{Ad}N_2N_2]H_2$. To a THF solution containing 100 mg of $[N_2Cl_2]H_2$ (0.286 mmol, 1 equiv.), 80 µL of triethylamine (0.572 mmol, 2 equiv.), 434 mg of adamantylamine (2.86 mmol, 10 equiv), and a catalytic amount of sodium iodide were added. After heating the dark brown solution to reflux for 12 hours, solid byproducts were removed via vacuum filtration. Addition of diethyl ether to the liquid filtrate led to precipitation of beige solids, which were then dissolved in dichloromethane and washed with 1 M sodium hydroxide. After drying with magnesium sulfate, the dichloromethane solution was placed under reduced vacuum to remove volatiles, revealing light brown solids. Excess adamantylamine was removed by sublimation under static vacuum at 65°C. ^{1}H NMR (500 MHz, $CDCl_3$) δ/ppm: 1.59–1.76 (overlap, 54 H, C*H* from free adamantylamine and adamantylamine of $[^{Ad}N_2N_2]H_2$), 2.04–2.16 (overlap, 14 H, N*H* from free adamantylamine and adamantylamine from $[^{Ad}N_2N_2]H_2$,), 2.72 (s, 4 H CH_2), 4.87 (s, CH_2, 4 H), 3.83 (s, 6 H O-CH_3), 7.00 (s, 2 H, aryl-*H*). MS(ESI+) m/z: 579.4 (MH+).

References

[1] Szigethy, G.; Heyduk, A. F. *Inorg. Chem.* **2011**, *50*, 125–135.